HYBRID ORGANIC/INORGANIC NANOMATERIALS: DEVELOPMENT OF MALONAMIDE-FUNCTIONALIZED NANOPARTICLES DESIGNED FOR LANTHANIDE ION DETECTION

by

CARMEN ELLEN LISOWSKI

A DISSERTATION

Presented to the Department of Chemistry
and the Graduate School of the University of Oregon
in partial fulfillment of the requirements
for the degree of
Doctor of Philosophy

March 2010

University of Oregon Graduate School

Confirmation of Approval and Acceptance of Dissertation prepared by:

Carmen Lisowski

Title:

"Hybrid Organic/Inorganic Nanomaterials: Development of Malonamide-Functionalized Nanoparticles Designed for Lanthanide Ion Detection"

This dissertation has been accepted and approved in partial fulfillment of the requirements for the degree in the Department of Chemistry by:

Darren Johnson, Chairperson, Chemistry
James Hutchison, Advisor, Chemistry
Catherine Page, Member, Chemistry
Michael Haley, Member, Chemistry
Barbara Roy, Outside Member, Biology

and Richard Linton, Vice President for Research and Graduate Studies/Dean of the Graduate School for the University of Oregon.

March 20, 2010

Original approval signatures are on file with the Graduate School and the University of Oregon Libraries.

An Abstract of the Dissertation of

Carmen Ellen Lisowski for the degree of Doctor of Philosophy

in the Department of Chemistry to be taken March 2010

Title: HYBRID ORGANIC/INORGANIC NANOMATERIALS: DEVELOPMENT OF MALONAMIDE-FUNCTIONALIZED NANOPARTICLES DESIGNED FOR LANTHANIDE ION DETECTION

Approved: _____
James E. Hutchison

Hybrid nanoscale complexes incorporate the attributes of organic and inorganic components to yield novel multifunctional materials. Because the individual components themselves and the combinations used can be widely varied to tune the properties of the resulting complex, the potential for new properties and practical applications is nearly limitless. However, widespread use of these materials relies on appropriate design, synthesis and characterization strategies to ensure proper function and compositional integrity. This dissertation describes the chemistry of these hybrids, made possible by combining organic ligands, inorganic nanoparticles, and metal ions, and the interesting optical and spectroscopic properties associated with the hybrid nanomaterials.

Organic ligands containing Bunte salt and acyclic malonamide functionalities were attached to gold nanoparticles to produce colorimetric sensors for lanthanide ion

detection. Bunte salt functionality stabilizes the gold core and malonamide functionality offers selective and sensitive lanthanide ion binding. The binding interaction controls a nanoparticle cross-linking event that changes the color of the nanoparticle solution, resulting in visual, colorimetric lanthanide ion detection. Next, the concentration of malonamide ligand was diluted and replaced with a diluent ligand yielding nanoparticles stabilized with a mixed ligand composition. The mixed ligand environment makes the optical response of the colorimetric sensor reversible. Furthermore, the use of Bunte salt ligands during nanoparticle synthesis has allowed the investigation of the role of reducing agent on nanoparticle stability.

In addition to exploring interactions pertaining to gold nanoparticle complexes, a new approach to sensitize europium ion luminescence was developed by fabricating a zinc oxide/europium complex. A molecular linker permits simultaneous zinc oxide nanoparticle functionalization and trivalent europium binding in order to tether the europium ion close to the nanoparticle surface. The zinc oxide nanoparticle can then act as an inorganic antenna, transferring energy to the europium ion and enhancing its luminescence.

Finally, a strategy was developed to synthesize bifunctional bicyclic malonamides. Synthesis of these ligands allows the enhanced f-block ion binding affinity of bicyclic malonamides to be incorporated into functional materials to compare their performance to our previously prepared acyclic malonamide hybrid complexes.

This dissertation includes both my previously published and my co-authored materials.

CURRICULUM VITAE

NAME OF AUTHOR: Carmen Ellen Lisowski

PLACE OF BIRTH: Pittsburgh, Pennsylvania

DATE OF BIRTH: September 19, 1978

GRADUATE AND UNDERGRADUATE SCHOOLS ATTENDED:

University of Oregon
University of North Carolina at Asheville

DEGREES AWARDED:

Doctor of Philosophy in Chemistry, 2010, University of Oregon
Master of Science in Chemistry, 2005, University of Oregon
Bachelor of Science in Chemistry, 2003, University of North Carolina at Asheville
Bachelor of Science in Environmental Science, 2003, University of North Carolina at Asheville

AREAS OF SPECIAL INTEREST:

Hybrid nanoscale materials
Green chemistry

PROFESSIONAL EXPERIENCE:

Graduate Research Assistant, Department of Chemistry, University of Oregon, Eugene, Oregon, 2004-2010

Research Assistant, Department of Chemistry, University of North Carolina at Asheville, Asheville, North Carolina, 1999-2003

Water Analysis Technician, Environmental Quality Institute, Asheville, North Carolina, 1999-2001

GRANTS, AWARDS AND HONORS:

National Science Foundation IGERT Fellow, 2006-2009

Technology Entrepreneur Program Fellow, 2008

National Science Foundation GK-12 Fellow, 2005-2006

Rotary Club Scholarship, 2002

Audubon Society Scholarship, 2001

PUBLICATIONS:

Lisowski, C. E.; Hutchison, J. E. *Analytical Chemistry* **2009**, 81, 10246-10253.

Lisowski, C. E.; Duncan, J. R.; Heard, G. L.; Setser, D. W.; Holmes, B. E. *Journal of Physical Chemistry A* **2008**, 112, 441-447.

Braun, B.; Charney, R.; Clarens, A.; Farrugia, J.; Kitchens, C.; Lisowski, C.; Naistat, D.; O'Neil, A. *Journal of Chemical Education* **2006**, 83, 1126-1129.

ACKNOWLEDGMENTS

There is no doubt that my successful navigation through the murky waters of research were made possible from the dedication extended to me from Jim Hutchison. I sincerely appreciate his encouragement over the years, and the flexibility that I was given to develop a research project that I was both eager and excited to explore.

Over the years, I have had the great fortune of working with an amazing group of individuals. I cannot count the number of times I knocked on Mike Haley's door for organic synthesis advice. I thank him for his time and patience. Christa Inman and Evan Foster took me under their wing during my first years in the Hutch lab and to this day continue to provide answers to my never-ending questions. Josh Razink was extremely helpful to me when acquiring nanoparticle images on the TEM. I surely would still be in lab making malonamides had Sean McClintock and Tatiana Zaikova not graciously offered their assistance with my synthetic efforts. I have worked with Sam Lohse on several projects, and thank him for his collaborative spirit. Rick Glover has been both a good friend and coworker, willingly sharing his thoughtful insight, goldfish, and colds. John Miller and Lallie McKenzie were both helpful over the years, and Pat Haben, Ed Elliot and Bev Smith all contributed to the many productive discussions spawned from countless days in the bullpen.

A great deal of my research was made possible through assistance from the fantastic staff at the CAMCOR facility. Steve Golledge was extremely helpful with data collection on the XPS, and Sujing Xie was crucial in the collection of nanoparticle images

and EDAX spectra on the TEM. Kurt Langworthy assisted me on the SEM, and was the first person to train me in TEM analysis. Collaboration with Dave Schut and the rest of the scientists at Voxtel enabled the malonamide/ZnO project to occur. I would also like to acknowledge the National Science Foundation's GK-12 and IGERT Fellowship programs for research support.

And finally, I must thank my family for their encouragement and unwavering belief in me over the years, especially my mom, who flew to Oregon a month before my advancement to stock my freezer with dinners. I cannot thank her enough for her selfless ways. And lastly, I would like to thank Luke for taking care of life for the past several months, and making the last few years in Oregon so lovely that I think we should stay for a couple more.

TABLE OF CONTENTS

Chapter Page

Chapter Page

Chapter Page

Chapter Page

LIST OF FIGURES

Figure Page

Figure Page

LIST OF CHARTS

LIST OF SCHEMES

CHAPTER I

INTRODUCTION: DESIGN AND CHARACTERIZATION OF HYBRID NANOSCALE MATERIALS

Introduction

The Lycurgus Cup is perhaps one of the oldest and well-known cases where the inherent property of a nanoscale material was used for functional application. This piece of 4th century AD Roman glasswork appears green in color in reflected light. When illuminated from within, the chalice is bright red. Electron microscopy has shown the glass to be embedded with roughly 70 nanometer gold nanoparticles, owing to the red hue of the glass.[1] Unbeknownst to artisans at the time, the incorporation of nanoscale substrates into functional materials would continue into the future, becoming a central theme for hybrid nanomaterial design in the 21st century. Our comprehension of the phenomena that govern nanoscale substrates is immeasurable compared to the days of roman glassmakers, however, scientists today still strive to understand and control the properties of materials on the nano scale.

Nanotechnology is defined as the study of fundamental principles, interactions, and fabrication of structures with at least one dimension in the size regime of 1-1000 nanometers (nm).[2] To refine this broad term to better suit the nature of specific research, scientists coin nano-inspired terminologies including nano-flowers,[3-5] -cars,[6] -rice,[7-9] -diamonds,[10-12] and –forests.[13,14] Nanomaterial-based technologies have advanced the development of microelectronics,[15,16] optical devices,[17,18] sensors,[19-21] and the bio-medical field[22,23] by taking advantage of a desirable function resulting from an inherent property of the chosen nanoscale substrate. Multi-functional nanoscale materials take advantage of several properties through the combination of inorganic and organic components to form a hybrid nanoscale complex. Hybrid complexes utilize the advantageous properties unique to each individual component to develop new materials for functional application. To successfully fabricate functional hybrid nanoscale materials, however, the inorganic and organic component interactions must be understood. Solubility and stability are two parameters that influence the interactions of the inorganic and organic components. Development of reliable synthetic methods to control the interactions of the final hybrid product will expedite the development of hybrid nanoscale materials for commercial application.

Solubility is the ability of a solute to dissolve in a given liquid media to form a homogeneous solution. Bare, non-functionalized nanoscale materials including inorganic metal and metal oxide nanoparticles often have limited solubility. Nanoparticles can contain a layer of surface organic molecules, or ligand shell, that help impart desired solubility.[24] As a way to promote green nano-syntheses, nanoparticles

are often sought to be soluble in environmentally compatible solvents including water and non-chlorinated solvents.[25] Ligands can be designed to permit these specific requirements for solubility, and can also permit ligand exchange, subsequent ligand reaction, and functionalization to solid supports, making functionalized nanoparticles attractive substrates for inorganic/organic hybrid materials.

Nanoparticle ligand shells help to stabilize against instability and irreversible particle agglomeration.[26] To stabilize the particle, the chosen organic ligand must contain a functional group that can interact with the particle surface, either through covalent attachment or an electrostatic interaction between the charged ligand and the metal nanoparticle core. In either case, the organic ligand serves to passivate the particle surface, shielding the nanoparticle from interaction with neighboring particles, which allow the particle to remain in solution.[26] Because electrostatic interactions are easily perturbed by changes in ionicity, covalent attachment is often the desired means for organic ligand attachment to inorganic substrates.[27] Furthermore, organic ligands can be developed for inorganic substrate functionalization and subsequent synthetic modification, providing solubility and stability to nanoparticle surfaces, while also providing reactive groups for functional application. Ligand passivated nanoparticles will be discussed at length, and are the central theme to this dissertation research.

The overarching motivations of this research project are to advance the current understanding about the requirements needed to successfully meld inorganic nanoparticles with organic ligands to form functional nanoscale hybrid complexes. The successful fabrication of organic ligand functionalized nanoparticles allows synthetic

requirements, surface chemistry, and binding interactions to be explored. To study these interactions, the malonamide class of ligands was chosen as the organic component of the hybrid complex. Malonamides exhibit desirable properties that make these ligands suitable candidates for material hybridization, including flexibility for synthetic modification, specificity for lanthanide ions, and a preferred ligand-to-metal binding ratio. The increased use of lanthanide ions in commercial applications warrant the development of technologies able to detect these metal ions in the environment, and the strong line-like emission properties of lanthanide ions provide a spectroscopic reporter convenient for characterization purposes. Nanoparticles of gold and zinc oxide possess interesting optical and electronic behaviors, respectively, that enable lanthanide detection methods to be envisioned. Thus, successful synthesis of malonamide-functionalized gold nanoparticles made it possible to develop a colorimetric sensor for lanthanide ions, and the synthesis of malonamide-functionalized zinc oxide nanoparticles allowed the sensitization of europium to occur. The general design strategy used to develop these hybrid complex materials permitted the gold nanoparticle system to be refined, which led to the development of a reversible sensor. In addition, the use of specifically tailored ligands for our nanoparticle syntheses allowed the parameters necessary to develop methods for stable, functionalized nanoparticle solutions to occur. Lastly, successful synthesis of acyclic malonamides designed for inorganic material functionalization enabled important characteristics to be established, enabling the successful optimization of the bifunctional bicyclic malonamide ligand.

Malonamides

A number of chelating ligands have been under investigation for the detection and/or removal of Ln/Ac metals,[29,30] and acyclic malonamides have shown considerable promise as candidates for the removal of trivalent Ln and Ac metals.[31,32] However, minimal advancements in extraction efficiency have been realized for acyclic malonamides,[33-35] as it was determined the extraction efficiencies were limited by the induced strain introduced to the ligand during metal complexation.[28] A bicyclic malonamide (BMA) molecule, based upon rational design using molecular mechanic calculations to predict ligand-metal interaction, was developed through collaboration between Pacific Northwest National Laboratory (PNNL) and the Hutchison Laboratory. The BMA ligand was designed to be in a preorganized conformation to bind trivalent lanthanide (Ln) and actinide (Ac) metals preferentially (Figure 1.1).[28]

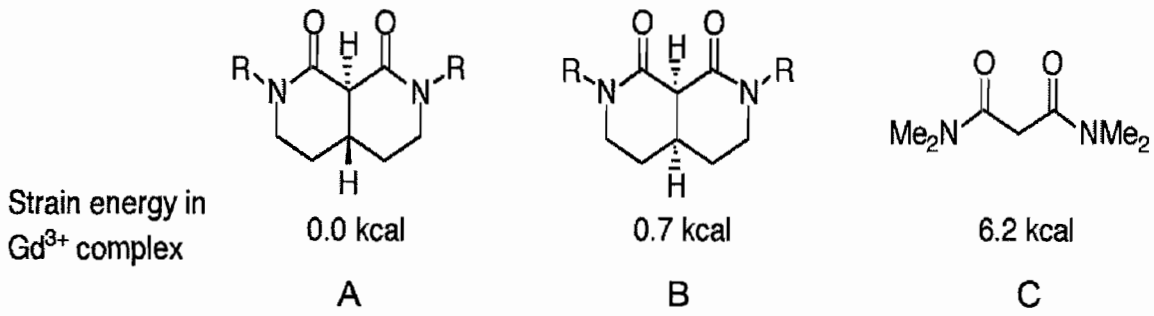

Figure 1.1: Schematic of the energy needed for malonamide-lanthanide binding. Strain energies (calculated by molecular mechanics) due to ligand reorganization upon binding to gadolinium (a representative trivalent lanthanide) are provided for the cis and trans forms of the bicyclic malonamide compared to a representative acyclic malonamide. The decrease in strain energy results in an enhanced binding for f-block ions.

The preorganized conformation of the bicyclic malonamide decreases the strain energy required to bind the ligand to the metal from 6.2 kcal/mol for a representative acyclic malonamide (Figure 1.1, C) to 0.7 kcal/mol for the bicyclic malonamide (Figure 1.1, B). This decreased strain energy results up to a 10^7 increase in binding affinity towards trivalent Ln/Ac metals.[28,36,37] The crystal structure has confirmed that the preorganized bicyclic malonamide ligand binds in a 2:1 ligand-to-metal ratio (Figure 1.2),[28,38] and effectively competes for binding sites around the trivalent metal ion in aqueous acidic media.

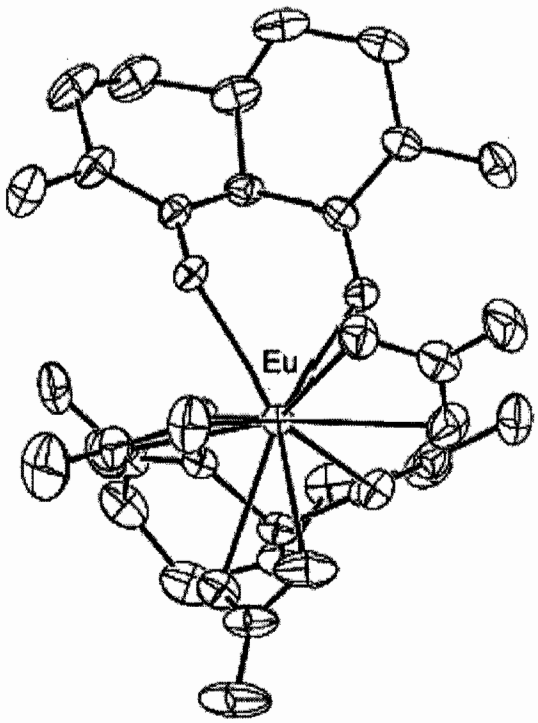

Figure 1.2: X-ray crystal structure of the europium complex of cis-dimethylbicyclic malonamide. Reproduced with permission from Lumetta, G. J.; Rapko, B. M.; Garza, P. A.; Hay, B. P.; Gilbertson, R. D.; Weakley, T. J. R.; Hutchison, J. E. *Journal of the American Chemical Society*, 2002, 124, 5644-5645. Copyright 2002, American Chemical Society.

Binding studies and crystal structure were determined for the bis-functional bicyclic malonamide, where the functionality on each amide substituent (R) is the same (Figure 1.1, A & B). The generality of the synthetic route allows a wide variety of functional groups to be incorporated into the bis-functional BMA molecule,[38] and necessitates few modifications to the synthetic procedure to incorporate substrate-binding functionality into the molecule. However, the bis-functional bicyclic malonamide would initiate cross-linking if used as the capping ligand on a nanoparticle surface (Figure 1.3, A-C). A bicyclic malonamide molecule with differential substitution on each amide group ($R_1 \neq R_2$) is therefore necessary to prevent nanoparticle cross-linking during the functionalization process. Successful synthesis of a differentially substituted bicyclic malonamide would take advantage of the enhanced binding properties of the BMA ligand, and offer the same flexibility for incorporation into hybrid complexes as that of acyclic malonamide ligands.

The acidic proton bridging the two amide carbonyls in acyclic malonamides can be accessed for synthetic modification without interference to the lanthanide binding site, which offers greater synthetic flexibility over their bicyclic analogs (Figure 1.4). The convenience of acyclic malonamide synthetic modification[39-41] has allowed malonamide ligands designed to bind inorganic surfaces including silica,[40] gold,[42] and zinc oxide[43] to occur. Synthesis of a ligand with terminal thiol, or masked thiol (Bunte salt), functionality would allow direct functionalization of a gold nanoparticle surface.[44,45] The ability to provide synthesis in a single, direct step eliminates the need

for ligand exchange, a method traditionally used to incorporate functionality to the surface of gold nanoparticles.

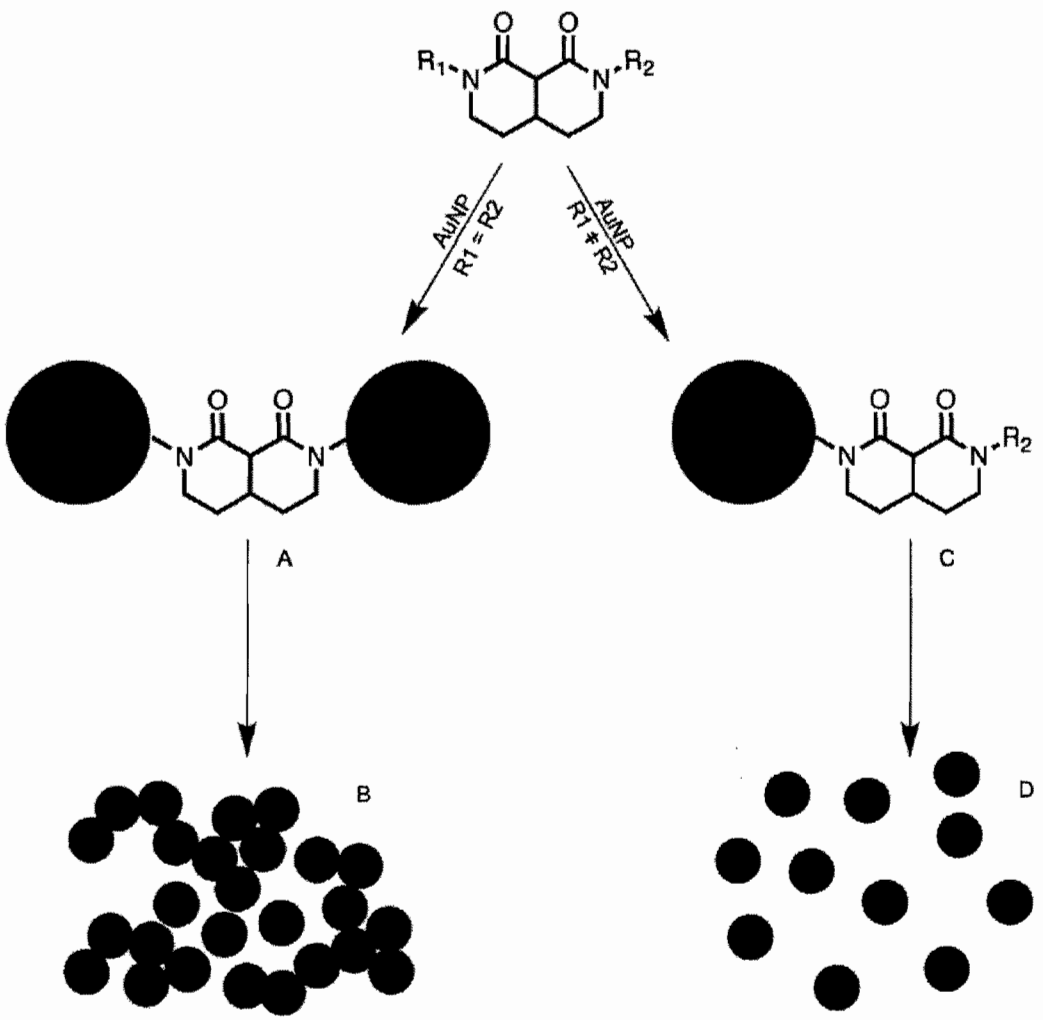

Figure 1.3: Theoretical schematic of BMA-NP complexes. Functionalization of a bis-functional BMA (A) would result in NP cross-linking and irreversible NP aggregation (B). The use of a differentially substituted BMA would allow only one amide substituent to bind to the NP surface (C), resulting in nanoparticles that do not cross link, and remain dispersed (D).

In addition to alleviating the need for ligand exchange, Bunte salts have been used to access gold nanoparticles with core diameters greater than 3 nm,[46] an important size requirement for colorimetric sensing. The optical, colorimetric properties that make gold nanoparticles desirable substrates for sensing application arise from the distinct surface plasmon absorption in the visible region of the absorption spectrum present for large (d_{core} >3 nm) gold nanoparticles,[42] a unique size-dependant property that is not present in bulk gold.

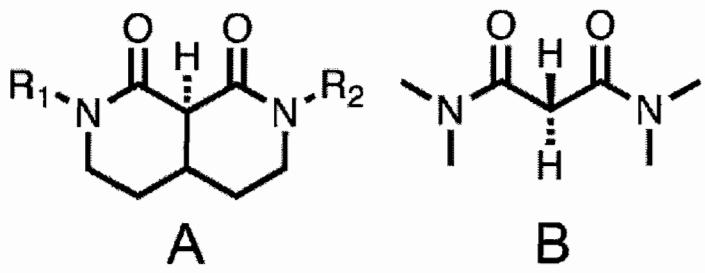

Figure 1.4: Bicyclic vs. acyclic malonamides. Preorganization of the bicyclic malonamide prevents synthetic modification at the acidic proton bridging the carbonyls (A) due to interference with the lanthanide-binding site. The acyclic malonamide is able to freely rotate, providing access for synthetic modification at the methylene carbon bridging the two carbonyls (B). Synthetic modification at this site allows additional, surface-binding functionality to be incorporated into the molecule without interfering with the lanthanide-binding site.

Gold

Bulk gold is prized for is malleability and lack of reactivity. However, when the size of gold reaches the nanometer scale it becomes highly reactive, which has provided the basis for a wealth of research related to both its electronic and optical behavior. A

specific property discussed in this dissertation research is that of the size-dependant surface plasmon resonance that gold nanoparticles exhibit, and allow the chromatic properties of gold nanoparticles to be utilized as colorimetric sensors.

The electrons in nanoscale gold are close to the surface of the particle, which generate confined surface plasmons that can interact with light on the particle surface.[47] When an incoming light wave interacts with a particle, the electron density is polarized to one side of the particle, and then oscillates to the other side of the particle in resonance with the frequency of the incoming light. This phenomenon is known as plasmon resonance (Figure 1.5).[42] Because this oscillation is located at the particle surface, it is called the surface plasmon resonance (SPR). The absorption of the surface plasmon resonance occurs in the visible region for gold nanoparticles, and leads to a surface plasmon band (SPB) at approximately 520 nm in the UV-vis absorption spectrum. Nanoparticles in the size range between 3 and 100 nm display a distinct surface plasmon band,[47] though the shape, intensity and location of the surface plasmon band depends on the shape and size of the nanoparticles, as well as dielectric constant of the surrounding media.[24,42,47-50]

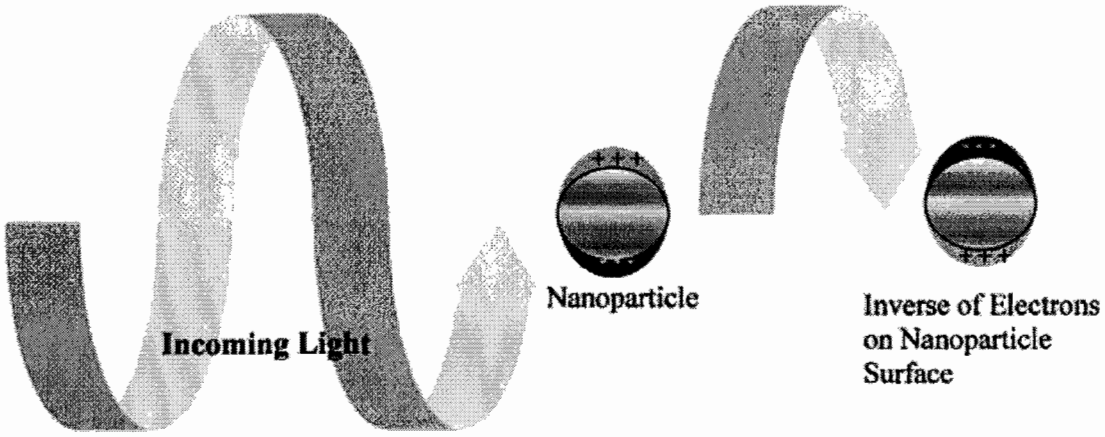

Figure 1.5: Depiction of AuNP surface plasmon resonance. The SPR in a metal nanoparticle sphere is due to the resonant oscillation of the surface electrons with incoming light, and provides the basis for the AuNP sensors designed in this dissertation. Reproduced with permission from Eustis, S.; El-Sayed, M. A. *Chemical Society Reviews* 2006, 35, 209-21. Copyright 2006, RSC Publishing.

The surface plasmon absorption at 520 nm is absent for both bulk gold and particles with diameters below 2 nm. The conduction electrons are no longer confined to the surface gold in bulk samples,[47] and at sizes below 2 nm, quantum size effects become important, so the density of states no longer forms a continuous band structure.[24] The nature of the surface plasmon band of gold nanoparticles is dependant on interparticle spacing.[24] When the spacing between two particles is decreased to the point in which electronic dipoles of the particle can interact, the dipoles couple, and a shift and broadening of the surface plasmon band occurs.[24] The dipole coupling results in a visible, colorimetric change from red to blue-purple as the absorbance shifts from 520 nm to longer wavelengths, respectively (Figure 1.6).[50-55] It is this electromagnetic

dipole coupling that provides the basis for the colorimetric, optical response in gold nanoparticle based sensors.

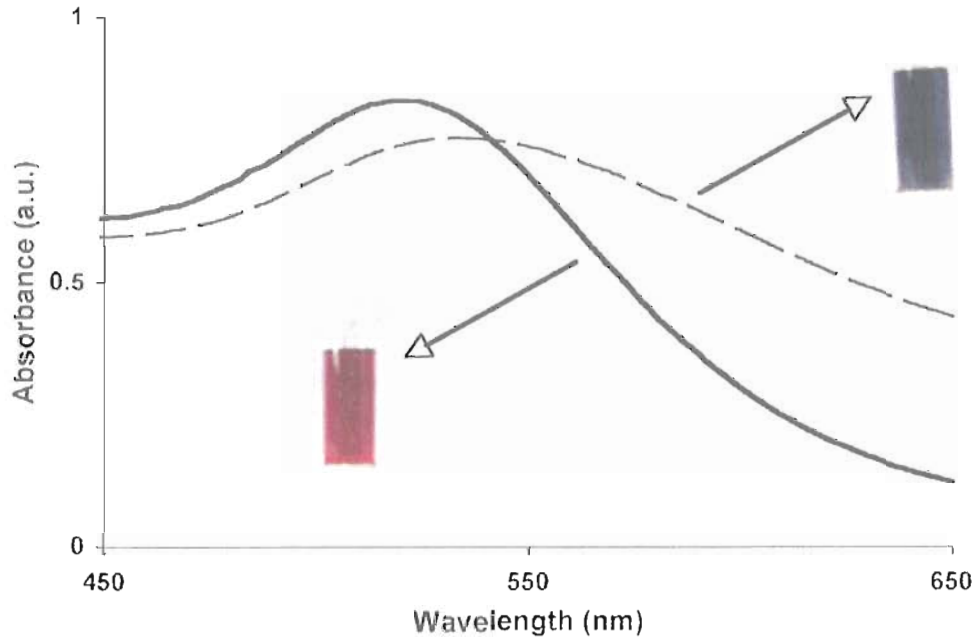

Figure 1.6: UV-vis spectra of ~ 8 nm gold nanoparticles. The dispersed gold nanoparticles exhibit a distinct plasmon absorption at ~520 nm (solid trace), rendering the solution red. When the nanoparticles are brought to within close proximity for particle-particle plasmon interaction a bathochromic shift, and broadening of the absorbance can be monitored (broken trace), changing the color of the nanoparticle solution to blue-purple.

Gold nanoparticle colorimetric sensors. The use of gold nanoparticles for analyte sensing has been reported for over a decade.[52] Since this first report, the use of gold nanoparticles for optical sensing of various analytes has been exploited for application in both organic and aqueous solution.[50-54,56] The qualitative, real-time detection that functionalized gold nanoparticles can provide has made colorimetric gold nanoparticle-based sensing an active area of research.[50-53,56]

The use of gold nanoparticles functionalized with biological-based molecules including peptides,[57,58] aptamers[19,59] and DNA[54,56] allow both selective and sensitive analyte detection to occur, as detection limits in the femtomolar range have been reported.[52] The low detection limits are a result of analyte-specificity that is built in to the backbone of the biological molecule. However, the use of biological ligands for sensing application is often limited due to constraints with narrow ranges of pH, temperature, and the necessity to buffer the nanoparticle solution.[50,56] Kim, Johnson and Hupp report the use of a non-biological ligand-based gold nanoparticle sensor for use in heavy metal sensor applications.[53] Gold nanoparticles functionalized with 11-mercaptoundecanoic acid (MUA) were used to create water-soluble particles that provided a receptor site able to bind lead, cadmium, and mercury. These MUA-based sensors are able to detect heavy metal concentrations in the μM range, even though MUA is known to have only a limited affinity to these particular ions.[53] The selectivity and sensitivity of gold nanoparticle-based sensors can vary dramatically based on the ligand chosen for nanoparticle functionalization, and suggests that the use of a ligand having a known binding affinity for a particular analyte should allow low limits of detection to be achieved.

The preferred binding affinity to lanthanide ions that the malonamide class of ligands displays suggests that an even lower level of detection can be attained for application in colorimetric gold nanoparticle-based sensing as compared to the MUA-functionalized gold nanoparticles. In addition, the preferred 2:1 ligand/metal binding ratio of the malonamides would facilitate nanoparticle interaction, initiating the surface

plasmon coupling event. Successful synthesis of a malonamide functionalized gold nanoparticle should therefore permit selective, sensitive colorimetric lanthanide detection to occur, as depicted for the acyclic malonamide (Scheme 1.1).

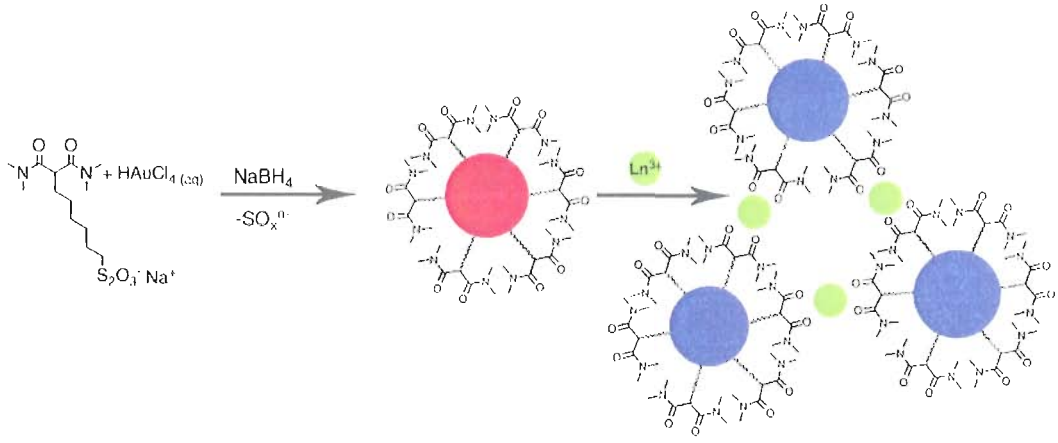

Scheme 1.1: Schematic of malonamide functionalized AuNPs. The use of a Bunte salt terminated malonamide allows direct functionalization to the surface of gold nanoparticles to occur. The preferred 2:1 ligand/metal binding ratio of the malonamide for lanthanide ions facilitates the nanoparticles to come within close proximity for electronic dipole coupling. This lanthanide-induced coupling event changes the color of the nanoparticle solution, allowing the formation of a colorimetric lanthanide sensor.

In addition to applications in colorimetric sensing, the design of a ligand that incorporates malonamide functionality with a reactive group for substrate binding would enable the development of other hybrid complexes. The strong lanthanide-binding properties of malonamide ligands would also permit exploration into spectroscopic lanthanide detection to occur, as lanthanide ions have been combined with various inorganic substrates[60-64] for the fabrication of luminescent hybrid structures. One such substrate that holds promise for the development of luminescent devices is that of zinc oxide.

Zinc oxide

Zinc oxide (ZnO) occurs naturally as the mineral zincite, but is synthetically derived for material application. It is a type II – VI wide-gap semiconductor with a direct gap of about 3.4 eV, rendering it both clear and colorless in the visible region of the energy spectrum,[65] which has contributed to the incorporation of zinc oxide in material applications, including sensors,[66,67] antimicrobial activity,[68] and more recently, in the electronic industry for its potential in liquid crystal displays.[69] Additionally, a widely studied topic for zinc oxide-based research is in the area of luminescent devices[70-76] due to the strong UV-absorption properties, commercial accessibility, and environmental compatibility of ZnO.[77-79] One area of particular interest is in the combination of zinc oxide and lanthanide ions. Lanthanide ions have notably poor absorption properties, but strong line-like emission properties that make them suitable candidates for light-emitting devices.[62] The strong absorption properties of zinc oxide have been shown to transfer energy to lanthanide ions through doping,[80] or surface functionalization with chromophores.[62]

Attempts to dope zinc oxide have proved challenging due to mismatches in atomic radii of lanthanide ions and zinc.[62] To overcome the challenges of effective doping, methods to attach lanthanides to zinc oxide via surface ligands have recently been explored.[62] Methods to modify the surface of zinc oxide has been successfully demonstrated with various ligands,[81] including PEG,[82] silanes,[83] and carboxylic acids.[43,62] The ability to functionalize the surface of zinc oxide allows it to be used as a substrate for study in inorganic-organic hybrid systems, and should allow a malonamide

ligand to be developed for the surface functionalization of zinc oxide. Synthesis of a ZnO-malonamide-lanthanide complex will allow the possibility of energy transfer between zinc oxide nanoparticles and a bound lanthanide ion to be explored. In addition, the luminescent properties of the hybrid species can be investigated. Synthesis of such hybrid materials advances the study of nanoscale complex fabrication by permitting the synthetic requirements necessary for each component to be studied, both individually, and after hybridization.

Design of hybrid nanoscale complexes

Successful incorporation of organic and inorganic components allows surface interactions to be explored while inspiring additional interactions, such as the delivery of different organic mixtures to a single inorganic core.[84,85] Reproducible incorporation of multiple organic ligands onto the surface of a single nanoparticle substrate requires precise control over reaction conditions. Development of a synthetic method to provide reaction control over nanoparticle compositions will provide control over surface chemistry impacting nanoparticle function, such as sensor reversibility, and spatial assembly for nanoscale architectures.

Despite extensive nanoparticle research, few reports have successfully shown controlled fabrication of higher order nanoparticle assemblies.[86-89] Control over the spatial distribution of nanoparticles allows interpretation of interparticle electromagnetic coupling,[90-92] provides greater understanding of optimal distance, damping effects and overall interaction with other species,[86] and can allow the

fundamental science of nanoscale materials to be explored in greater detail. However, for the development of such applications to become a reality, rigorous characterization of prepared nanoscale products must be attainable.[93,94]

Characterization of hybrid nanoscale materials

One of the major challenges associated with nanoscale materials synthesis is the ability to assess product purity and integrity. Characterization challenges can be overcome, in part, by utilizing a combination of characterization techniques, allowing individual components of the system to be analyzed and subsequently assessed for comprehensive analysis. Instrumentation necessary for complete characterization of organic/inorganic hybrid nanoscale complexes included in this dissertation work involve ^{1}H and ^{13}C nuclear magnetic resonance spectroscopy (NMR), Fourier transform infrared spectroscopy (FT-IR), ultraviolet-visible spectroscopy (UV-vis), transmission electron microscopy (TEM), and x-ray photoelectron spectroscopy (XPS). Each of these techniques is indispensable in providing information necessary to assess the purity and composition of prepared nanoscale organic/inorganic hybrid complexes.

Nuclear magnetic resonance spectroscopy. Ubiquitous to synthetic organic chemistry, NMR is used to monitor changes in chemical structure and molecular purity. Molecular purity is of the utmost importance in nanoscience due to the highly reactive surface of nanoscale materials. Small amounts of synthetic impurities can have detrimental impacts on both the nanoparticle surface composition and surface-ligand interactions,[95] preventing complete surface ligand passivation that can impact the

structural integrity of monolayer formation, stability and interaction with local chemical environements.[95] Detection of organic impurities via NMR prior to surface functionalization is therefore an essential tool to assess organic ligand composition and purity to help ensure that the surface ligand composition is comprised of only the desired functionality intended for substrate functionalization.

Fourier transform infrared spectroscopy. FT-IR allows changes in molecular structure to be monitored by vibrations and stretches relating to specific combinations of chemical bonds. The use of FT-IR spectroscopy can provide information about ligand composition, allow the functionalization of ligands to nanoparticle surfaces to be monitored, as well as confirm chelation of metal ions to organic ligands. FT-IR was particularly essential in characterization of the functionalization of zinc oxide described in this dissertation research. FT-IR allowed the binding of carboxylic acid to the surface of the ZnO substrate to be confirmed.[43] The loss of the C=O stretching frequency at ~1600 cm^{-1} to lower wave numbers was monitored as the C-O bonds formed on the zinc oxide surface (Figure 1.7, A). In a similar fashion, FT-IR was used in this dissertation research to monitor the binding of the malonamide functionality to europium ions, as the C=O amide stretch becomes both shifted and broadened as chelation to europium occurs (Figure 1.7, B).

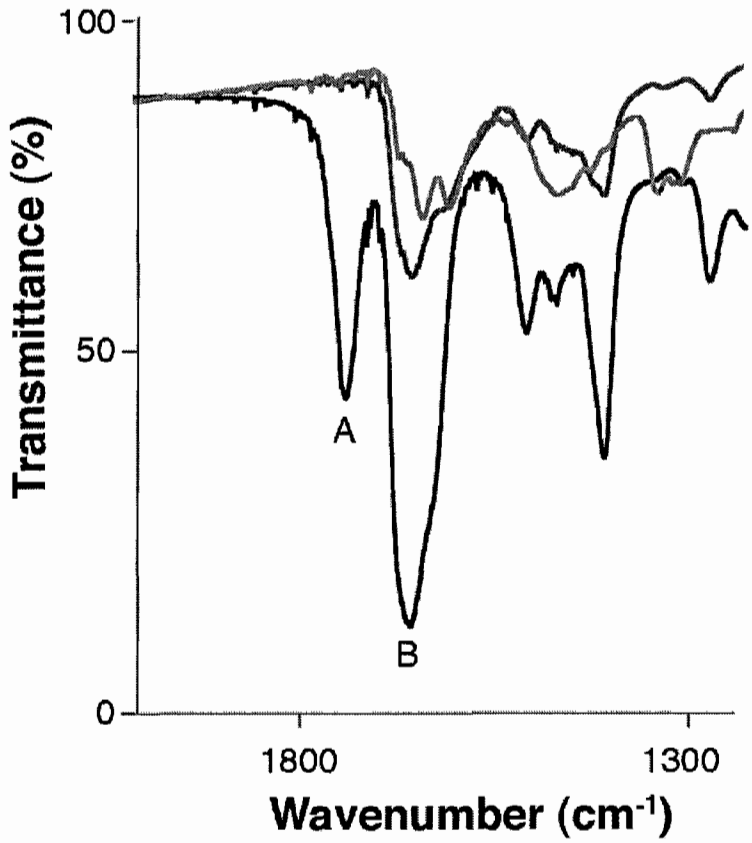

Figure 1.7: FT-IR spectra of malonamide functionalization to ZnO and Eu^{3+} chelation. The loss of the diamide acid carbonyl (A) as it binds to the surface of a zinc oxide nanoparticle can be monitored. The shift and broadening of the amide carbonyl region (B) can be used as a spectroscopic handle to confirm chelation of europium to the malonamide-functionalized zinc oxide nanoparticles.

Ultraviolet-visible spectroscopy. For applications using large gold nanoparticles (core diameter > 3 nm), UV-vis is the foremost method to assess surface plasmon interaction. A dispersed solution of gold nanoparticles exhibits an absorption at ~520 nm, rendering the solution red. When neighboring particles become close enough such that the surface plasmons interact, the absorbance at 520 nm becomes broadened, and a bathochromic shift to longer wavelengths occurs.[92] UV-vis allows

these events to be monitored in real time. UV-vis also allows particle stability to be monitored, as mass particle agglomeration results in a rise of the baseline. This rise in the baseline occurs when particles are no longer in solution, and is indicative of light scattering off of insoluble particles due either by a loss of stability, or by particle precipitation caused by mass aggregation. UV-vis can also be used to gain information relating to nanoparticle concentration.

The concentration of gold nanoparticles in solution (C_{NP}) can be approximated by a rearrangement of Beer's Law (1.1).

$$C_{NP} = \frac{A}{eb} \quad (1.1)$$

This calculation combines the use of UV-vis and transmission electron microscopy (TEM). First, the nanoparticle size is determined by TEM. Next, an experimentally derived extinction coefficient (e) is chosen based off of the size and dielectric constant of the NP solution.[96] Finally, the maximum absorbance (A) of the surface plasmon band from the UV-vis spectra of the gold nanoparticle solution, and the path length (b) of the UV-vis cell, is used to estimate the concentration of the solvated nanoparticles. This method allows not only the concentration of nanoparticles that are difficult to isolate to be determined, but also exemplifies the utility of using multiple characterization tools in tandem to acquire information about a prepared nanomaterial sample.

Transmission electron microscopy. The ability to visualize prepared nanoscale materials down to sub-nanometer size makes TEM perhaps the most widely used analysis tool for nanoscale research. TEM allows changes to the synthetic

parameters of nanoparticle formation including ligand precursor, source of gold salt, or concentration of reducing agent to be directly monitored and assessed for impacts on nanoparticle formation, size, and shape. In addition, when a representative group of images are collected for a particular nanoparticle sample, the use of image-processing software[97] allows the size distribution of the nanoparticle sample to be attained. Size distribution can provide information relating to the relative dispersity of a nanoparticle sample, as well as provide information about the efficacy of a given synthetic protocol developed to target a specific size regime of nanoparticles. However to obtain accurate size distribution data, the nanoparticles must be sufficiently dispersed on the TEM substrate such that individual particles can be counted, while aggregates of nanoparticles avoided. This can be especially challenging for nanoparticle samples passivated with ligand functionalities that promote hydrogen-bonded nanoparticle network formation. To obtain TEM samples that allowed successful size distribution analysis to occur, specially prepared TEM grids were utilized.

Functionalized SiO_2 TEM grids developed in the Hutchison lab,[98] and prepared by Dune Sciences™ were used for this dissertation research. Functionalization of the SiO_2 grid allows nanoparticles to be tethered to the grid surface via chemical interaction between the nanoparticle ligand shell and the grid-functionalized species. This allows the nanoparticles to remain well-dispersed on the grid, permitting a representative sampling of all nanoparticles present in the sample solution to be analyzed for size and size distribution. TEM grids functionalized with either aminopropyltriethoxysilane (APTES) or polyethyleneglycol (PEG) were used for TEM sample preparation of

MHTMMA- or MEEE-functionalized nanoparticle samples, respectively. The choice of substrate used to image nanoparticle samples can make a dramatic impact on the accuracy of the size distribution, as a TEM grid having no surface functionality can result in images with sparsely distributed, or hydrogen-bonded networks of nanoparticles, as opposed to the functionalized Smart Grids™ provided by Dune Sciences™ that allowed nanoparticle samples to be accurately imaged (Figure 1.8).

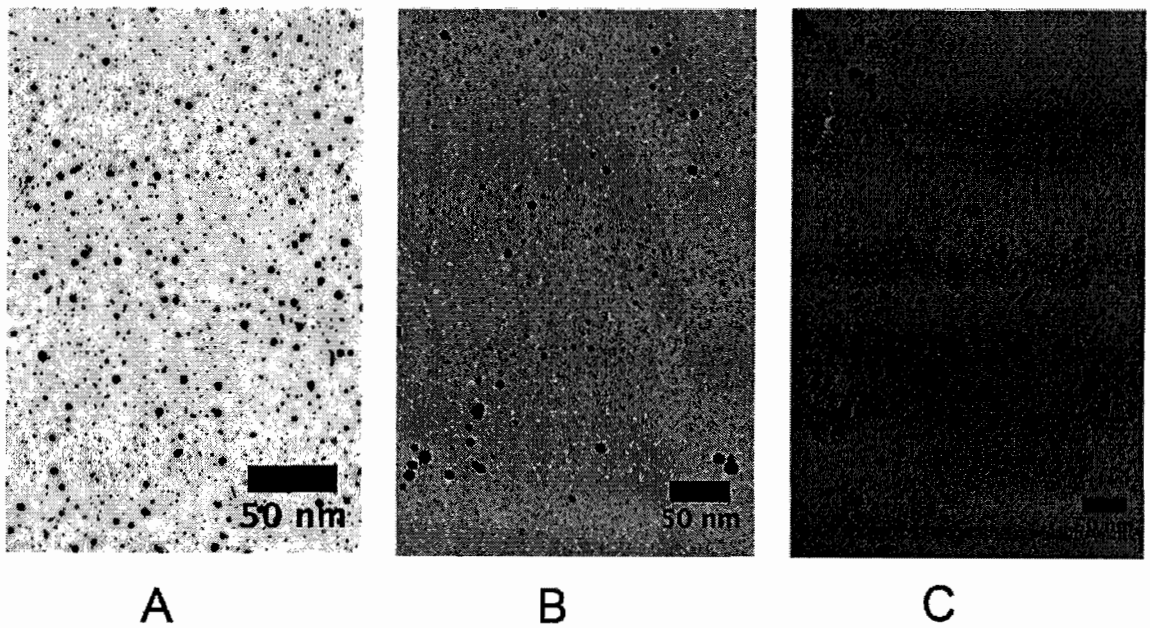

Figure 1.8: TEM micrographs of NPs on various grid substrates. The grid substrate can affect the resulting nanoparticle analysis. The functionalized Smart Grids™ allow representative nanoparticle samples to be imaged by taking advantage of interactions between the grid surface and the functionality on the nanoparticle surface (A). Grids having no chemical modification result in nanoparticle samples that are either sparsely distributed (B) or linked together via nanoparticle-nanoparticle attractive forces (C) that prevent accurate analysis of size and size distribution to occur.

Through choice of an appropriately functionalized TEM substrate the challenge of counting only individual nanoparticles during size distribution analysis can be

overcome, and a representative sample of all nanoparticles in solution can be obtained. This ensures that size and distribution of size for a particular nanoparticle synthesis is accurately assessed.

X-ray photoelectron spectroscopy. Commercially available in 1969, X-ray photoelectron spectrometers irradiate a sample-mounted substrate with monoenergetic soft X-rays, and use detected energy of photoejected electrons to provide information about the analyzed surface. The energy counted is directly related to the type and concentration of element present in the sample, allowing XPS to provide quantitative identification of species present in a sample, as well as provide information pertaining to the chemical environment and oxidation state of each type of element present. [99] This is particularly useful for analysis of attached ligands on a nanoparticle surface, especially during synthesis from Bunte salts, where the ligand undergoes a chemical transformation from an oxidized thiosulfate to that of a bound thiolate (Figure 1.9). To quantify the relative amount of unique species present, the area under each curve is measured relative to the intensity of a known signal. It is therefore important that there is no interference of the XPS substrate that can affect the relative integration of the peaks of interest. For the assessment of the sulfur 2p region, specially prepared substrates were used to allow quantitative data to be acquired to compare sulfur-to-gold ratios.

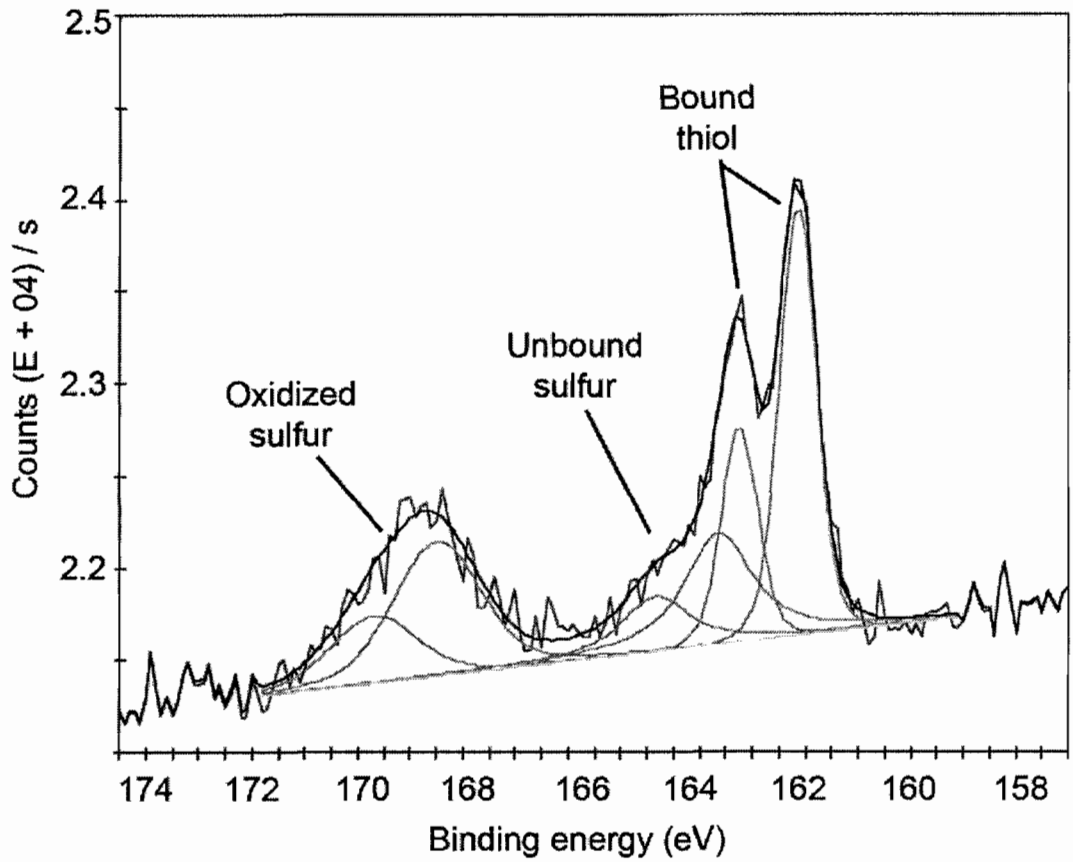

Figure 1.9: XPS spectra of ligand stabilized AuNPs. The sulfur 2p region during synthesis of gold nanoparticles stabilized from a MEEE Bunte salt precursor ligand show the unique and characteristic binding energies of various oxidation states of sulfur. These peaks can be used to provide information about the nature of the attachment to the nanoparticle surface, while the area under each curve can be used to measure the relative concentration of each species present.

Polished silicon wafers are often used to mount samples for XPS analysis due to the smooth, continuous nature of its surface. However, the energy loss line from the silicon 2s peak can interfere with that of the sulfur 2p region. Energy loss lines, or features, are generated from the interaction between the photoelectron and other electrons present at the surface of a sample.[100] Sample preparation for thiolate-bound

nanoparticles is thus vital, as peaks associated with a silicon substrate can cause confusion as to the true amount of thiolate-containing species on the nanoparticle surface. The energy loss line of silicon makes it difficult to discern whether the entire region in the S2p region is due to sulfur, or if it is a combination of sulfur and silicon loss feature. Deposition of a layer of chromium thicker than the sampling depth of the XPS instrument (70-100 angstrom) eliminates the interference of the loss feature by effectively subtracting the detection of silicon by the instrument. Furthermore, the prominent peaks associated with chromium occur in the 575-585 eV range,[101] far from the area of interest for either sulfur or gold. Use of these specially prepared XPS substrates allows the representative analysis of the sulfur-to-gold ratio to be performed for a series of ligand stabilized gold nanoparticles, and is discussed at length in Chapter V.

Although the information gathered by each of the previously described characterization methods was not used singularly to provide conclusive evidence about surface analysis of the prepared nanoscale materials, the combined use of each of these described tools has provided a wealth of knowledge enabling us to gain insight relating to ligand-nanoparticle, and ligand-metal interactions.

Dissertation overview

Chapter II describes the synthesis and characterization of a malonamide-functionalized zinc oxide nanoparticle complex. The malonamide-functionalized zinc oxide nanoparticle was used to explore energy transfer and subsequent sensitization of

europium (Eu^{3+}) ions in the solid state. The strong absorption properties of zinc oxide and the narrow, line-like emission properties of europium were combined via a ligand bearing both acid and diamide functionality which linked the europium ion close to the surface of the zinc oxide nanoparticle. The ligand served as a linker between the zinc oxide and europium, which allowed energy transfer from zinc oxide to the bound europium ion. Fourier transform infrared spectroscopy was used to confirm both the ligand-binding event to the surface of zinc oxide during the functionalization process, and europium chelation to the ligand-functionalized nanoparticle. Solid-state fluorescence spectroscopy was used to compare the difference in emission of the europium bound zinc oxide nanoparticles over that of isolated unbound europium. The preparation of the ZnO-malonamide-europium complex also allowed temperature-based changes in emission to be performed. Results from the thermal experiments showed an increase in fluorescence emission from the hybrid complex, and provided information relevant about the metal ions deposition during malonamide-ZnO complexation. The work described in this chapter reflects collaboration between Jim Hutchison, Dave Schut, and myself.

Chapter III describes the development of a selective and sensitive molecular sensor for trivalent lanthanide ions based upon a malonamide-functionalized gold nanoparticle. A new synthetic approach permits nanoparticle synthesis, stabilization *and* incorporation of selective lanthanide binding site in a single, direct step. The sensor incorporates a specifically designed dual function precursor ligand, the Bunte salt analog of 2-(3-mercaptoheptyl)-N^1,N^1,N^3,N^3-tetramethylmalonamide (MHTMMA),

that bears a sodium thiosulfate (Bunte salt) group that links to the gold nanoparticle core and a tetramethylmalonamide group that serves as the selective lanthanide binding site. The colorimetric response of the sensor to lanthanide ions is immediate, and sensitivity was measured to a ~50 nM concentration range for both europium and samarium. The results of this study suggest that design of a ligand architecture that provides nanoparticle synthesis and target analyte binding can enable stability and selectivity to be engineered directly to the nanoparticle surface, allowing colorimetric sensors to be developed for widespread use. The one-step synthesis offers uniform surface ligand composition, reduces the volume of waste generated during nanoparticle synthesis and purification, produces functionalized gold nanoparticles that are stable in non-modified aqueous environments and offers colorimetric detection at ambient temperature. The work performed in this chapter was co-authored by Jim Hutchison and myself, and laid the foundation for the experiments that led to the discovery of the reversible sensor described in chapter IV.

Chapter IV demonstrates the use of a microscale flow reactor to gain control over the ligand composition on the surface of gold nanoparticles through delivery of known quantities of two different individual ligands to a nanoparticle reaction mixture. The micro reactor allowed accurate delivery and mixing of multiple ligands during nanoparticle synthesis and stabilization. This enabled two different ligands to be put on the surface of a gold nanoparticle simultaneously during nanoparticle synthesis. Experiments using the Bunte salt analogs of both mercaptoethoxyethoxyethanol (MEEE) and 2-(3-mercaptoheptyl)-N^1,N^1,N^3,N^3-tetramethylmalonamide (MHTMMA),

are described. The use of the MHTMMA ligand as one of two ligand components on the nanoparticle surface builds off of the gold nanoparticle sensor work described in chapter III. The MHTMMA ligand has been shown to have a selective affinity to lanthanide ions, while the MEEE ligand has no known binding affinity for lanthanide ions. Furthermore, MEEE stabilized gold nanoparticles show no colorimetric or spectral response when introduced to solutions of lanthanide ions. This chapter describes experiments pertaining to the addition of small amounts of the MHTMMA ligand to the primarily MEEE stabilized gold core. The use of the micro reactor provides control over the ligand composition on the nanoparticle surface, which allows reversibility to be engineered into the function of the colorimetric sensor through modification of the resulting nanoparticle aggregates formed upon introduction to lanthanide ions in solution. Chapter IV was co-authored by Jim Hutchison and myself.

Chapter V describes experiments performed to investigate the resulting stability of gold nanoparticles synthesized from Bunte salt precursor ligands. Organic molecules bearing terminal Bunte salt functionality have been shown to produce a variety of nanoparticle sizes, including that of larger (diameter > 3 nm) gold nanoparticles, a size regime that has largely remained a challenge to synthesize due to the formation kinetics of traditional methods.[46] It has been proposed that Bunte salt ligands allow the larger gold cores to form because the thiosulfate to thiolate reduction occurs much more slowly on the gold surface than that of a traditional thiol, resulting in larger particle formation. The size of the resulting particles can be tuned with varying concentrations of gold salt, ligand and reducing agent, as well as with the incorporation of various

functionalities within the ligand backbone.[102] However, recent experiments suggest the stability of the synthesized particles is compromised if appropriate reaction conditions are not met. Specifically, the combination of mixing rate, reducing agent concentration, and method of reductant addition must be precisely controlled. Experiments to investigate the reaction parameters necessary for stable gold nanoparticle synthesis is described. The results of the study aim to understand the surface chemistry involved in stabilizing nanoscale gold clusters prepared from Bunte salt ligand precursors. Multiple analysis techniques were used in tandem to provide information about the prepared nanoparticle samples, including surface composition analysis via XPS to compare the ratio of oxidized sulfur with that of bound thiol (thiosulfate vs. thiolate). UV-vis spectroscopy was used to monitor the shape and position of the surface plasmon band, which provides information relating to particle stability. TEM analysis of the prepared nanoparticle samples was used to determine the size distribution analysis and extent of particle dispersion. The experiments in this chapter are based on work co-authored by Sam Lohse, Jim Hutchison, and myself.

Chapter VI describes the synthetic route developed to incorporate two different functionalities into the backbone of a bicyclic malonamide ligand. Molecular recognition offers sensitive and selective detection of specific analytes, but their successful incorporation into materials relies on synthetic methods capable of allowing diverse functionality to be readily modulated into the backbone of the molecule. The preorganization of the mono-functional 6,6-bicyclic malonamide is optimized for binding trivalent lanthanide ions over that of its acyclic analogs. However, the

incorporation of bicyclic malonamides into organic-inorganic hybrid structures have been limited due to the possibility of cross-linking created by the bis-functionality (R_1= R_2), as well as the inability to incorporate reactive groups via the previously reported synthetic method.[38] Synthesis of a bifunctional bicyclic malonamide that allows independent access to each amide functional group ($R_1 \neq R_2$) would permit the lanthanide-binding properties to be maintained while offering flexibility over solubility, sterics, or the ability to functionalize surfaces. The synthetic protocol that allows amide differentiation is described. The synthesis of a bifunctional BMA with protected terminal thiol functionality is also discussed. The synthesis of a protected thiol-terminated bicyclic malonamide molecule was targeted for its potential usefulness in gold nanoparticle sensor application. Future studies to compare acyclic and bicyclic malonamide-functionalized gold nanoparticles for colorimetric detection of lanthanide ions in water are discussed. Jim Hutchison, Tatiana Zaikova, Rob Gilbertson, Bevin Parks-Lee, and Dylan Domaille all contributed to the development of the synthesis described.

Bridge

During the end of my first year as a member of the Hutchison laboratory I met with Dave Schut, a scientist with Voxtel Inc., who wanted to explore the potential of malonamide ligands as a way to combine the properties of lanthanide ions and zinc oxide nanoparticles. Voxtel was interested in the ability to harness the spectroscopic signal of the emitting lanthanide ions for security applications and material tagging.

The project was appealing to the Hutchison laboratory because attachment of a malonamide ligand to a zinc oxide surface would allow the malonamide-ZnO surface interactions to be explored, as well as investigate the potential to develop a method for the spectroscopic detection of lanthanide ions. As part of this work, I developed a synthetic pathway and functionalization procedure to produce malonamide-functionalized zinc oxide nanoparticles. The synthetic procedure did not interfere with the lanthanide-binding site of the malonamide functionality, which allowed the formation of a zinc oxide-malonamide-europium complex to be prepared. The synthesis, characterization, and resulting fluorescence emission from this complex is discussed in Chapter II. In addition to the results generated from this work, the zinc oxide/malonamide project was the catalyst that initiated the work to synthesize the Bunte salt terminated malonamide ligand that are central to this dissertation work.

CHAPTER II

SENSITIZATION OF EUROPIUM LUMINESCENCE BY MALONAMIDE-FUNCTIONALIZED ZINC OXIDE NANOPARTICLES

Note: Portions of Chapter II are expected to appear in an upcoming publication co-authored by Lisowski, C. E.; Schut, D. and Hutchison, J. E. The first author designed the synthesis and carried out all of the laboratory work described herein. The author also composed the manuscript corresponding to Chapter II. J. E. Hutchison provided experimental and editorial guidance.

Introduction

Long fluorescent lifetimes, large Stokes shifts, and the sharp line-like emission bands of lanthanide ions make them desirable candidates for study as optical materials.[1-5] The long fluorescent lifetimes arise from Laporte forbidden *f-f* transitions, which also give rise to their notably poor absorption properties.[6,7] For this reason, strongly absorbing organic chromophores are often used for lanthanide sensitization (Figure 2.1, A). Energy absorbed from the chromophore is transferred to the lanthanide ion in a process commonly referred to as the 'antennae effect', resulting in dramatic increases in

lanthanide sensitization.[8-12] However, the use of organic antenna chromophores is limited to due their susceptibility to photobleaching, a photochemical deactivation of the chromophore that eliminates lanthanide sensitization.[13,14]

Methods to achieve sensitization have also explored the use of inorganic substrates incorporating lanthanide ions.[4,15-22] The relative low cost, environmental compatibility, and strong absorption properties of zinc oxide[23] (ZnO) have made it one such desirable inorganic substrate.[24-26] Successful incorporation of europium into the crystal structure of ZnO allows energy absorbed from the ZnO matrix to be transferred to the trapped europium ion (Figure 2.1, B).[27,28] The inorganic ZnO serves as the antenna that replaces the role of organic chromophores, which eliminates challenges associated with photobleaching. The synthesis of highly luminescent europium-doped ZnO remains difficult, however, due to the differences in ionic radii between the Zn (II) and Eu (III).[29] These ionic mismatches make it non-trivial to effectively synthesize a doped ZnO-europium material, a necessity for efficient energy transfer.[27]

We sought to design a new hybrid nanomaterial that combines the absorption properties of ZnO, the lanthanide coordination chemistry of an organic ligand, and the narrow emission lines of a lanthanide ion (Figure 2.1, C). ZnO nanoparticles (NPs) were chosen as the ZnO substrate because they are amenable to surface functionalization, absorb strongly, and are commercially available. Our approach uses a dual function molecule that binds to both the ZnO NP surface and a lanthanide ion.

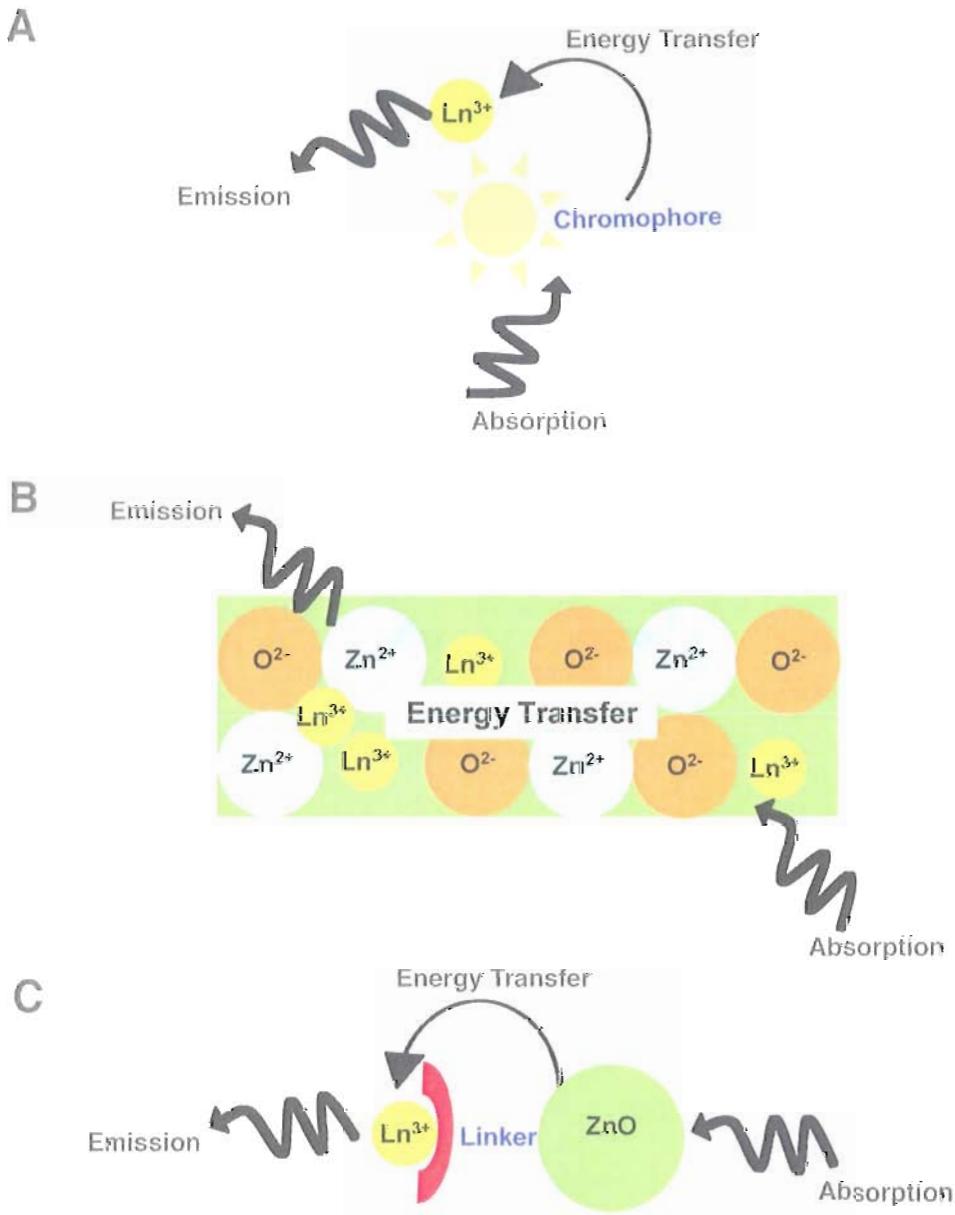

Figure 2.1: Schematic depiction of various strategies for lanthanide sensitization. Energy transfer between an organic chromophore and a Ln^{3+} ion can result in sensitization (A), but bleaching of the chromophore limits this method.[14] The synthesis of Ln^{3+} doped ZnO can effectively sensitize the incorporated Ln^{3+} ion (B). However, mismatches in the ionic radii make the synthesis of lanthanide doped ZnO non-trivial.[29] Our approach takes advantage of the absorption properties of ZnO NPs and the binding affinity of an organic linker to form a new hybrid nanomaterial capable of effective Ln^{3+} sensitization (C).

The design of the linker allows europium to be tethered close to the surface of the ZnO NP. The ZnO acts as an inorganic antenna, transferring absorbed energy from the NP to the bound Eu^{3+}ion, resulting in sensitization.

The use of a linker molecule to synthesize a hybrid complex from europium and ZnO NPs offers advantages for lanthanide sensitization over current methods. Because the lanthanide ion is not incorporated within the core structure of the ZnO substrate, the complexities of lattice mismatching during ZnO-lanthanide doping are eliminated. The use of this method therefore offers flexibility and convenience over challenging co-precipitation synthetic approaches. In addition, because the organic linker molecule described in this method is designed to facilitate surface functionalization and ion binding, and not for energy absorption, concerns with photobleaching[13,14,30] are eliminated.

The current report describes the design, synthesis and characterization of a ZnO-malonamide-europium complex. This new class of hybrid nanomaterial takes advantage of our previous work with acyclic malonamides[31] to design a molecular linker that allows ZnO and europium to be incorporated into a single complex material that results in the sensitization of europium (Eu^{3+}). The ZnO-ligand-Eu^{3+} complex results in a 15,000 times enhancement of luminescence over free $Eu(NO_3)_3$ salt. To our knowledge, this is the first report of an organic molecule-functionalized ZnO system that sensitizes Eu^{3+} through the absorption properties of NPs without relying on doping or an organic chromophore for sensitization. The increased europium emission observed for this complex structure demonstrates the use of ZnO NPs as inorganic antennae, and overall

represents the utility of rational hybrid nanomaterial design. The generality of our approach enables the inorganic components of the system to be tuned, allowing the development of other hybrid nanoscale materials to be designed.

Experimental methods

Materials. Tetramethylmalonamide was obtained from TCI-EP (Tokyo, Japan). All other reagents were obtained from Aldrich and used without further purification. Dichloromethane was distilled from calcium hydride prior to use. Tetrahydrofuran was distilled from potassium prior to use. Deionized water (18.2 MΩ-cm) was purified with a Barnstead Nanopure Diamond system and used for all experiments.

Synthetic procedures. *8-(dimethylamino)-7-(dimethylcarbamoyl)-8-oxooctanoic acid (TMMA-6-OH), **1**.* To 40 mL of distilled THF in a 250 mL round-bottomed flask equipped with a stir bar, sodium hydride (0.19 g, 7.7 mmol) and tetramethyl malonamide (1.22 g, 7.7 mmol) was added, followed by dropwise addition of $Br(CH_2)_6COOH$ (1.01 g, 5.1 mmol) dissolved in 10-mL of THF. The resulting thick white slurry was stirred at reflux for 16 h. 1 mL of deionized H_2O was added to quench the excess NaH, and the mixture was reduced to 10 mL using rotary evaporation. Dichloromethane was added, and the organic layer was washed with 100 mL of deionized H_2O, 50 mL of 10% aqueous HCl, 2 x 100 mL of saturated aqueous $NaHCO_3$, and 2 x 100 mL of saturated aqueous NaCl. The organic layer was dried over Na_2SO_4 and the solvent was removed by rotary evaporation to afford acid **1** as a clear, colorless oil (1.3 g, 92%). ^1H NMR ($CDCl_3$) δ 11.1 (br s, 1H), 3.61 (t, 1H), 2.97 (d, 12H), 2.37 (t, 2H), 1.87 (q, 2H), 1.65 (br p, 2H), 1.37 (p, 4H).

Functionalization procedure for grafting TMMA-6-OH to the ZnO surface. The TMMA-6-OH ligand, **1**, was bound to the surface of ZnO nanoparticles following literature precedent.[32] Briefly, to 50 mL of o-xylene in a 100 mL round-bottomed flask, equipped with a stir bar, TMMA-6-OH (1.27 g, 4.67 mmol) and ZnO NPs (1.00 g, 11.2 mmol) were added, brought to 50°C, and stirred vigorously for one hour. The particles were separated via centrifugation, followed by 3 x 20 mL toluene and 3 x 20 mL ethanol washes. The particles were then dried overnight under vacuum at 60°C.

Chelation procedure for binding Eu^{3+} to the TMMA-6-OH –ZnO hybrid. To a minimal amount of ethanol in a 25 mL round-bottomed flask, equipped with a stir bar, TMMA-6-OH-ZnO NPs (0.26 g) and $Eu(NO_3)_3$ (0.027 g, 0.06 mmol) were added, brought to reflux for 1 hour, removed from heat, and stirred overnight while coming to room temperature. The solids were separated via centrifugation and the supernatant removed with copious ethanol rinses. The particles were dried overnight under vacuum at 60°C and stored in a desiccator until further use.

Analytical procedures. Nanoparticles were characterized using a combination of Fourier transform infrared (FTIR) spectroscopy and fluorescence spectroscopy.

Fourier transform infrared (FTIR) spectroscopy. The FTIR spectra were obtained on a Nicolet 550 spectrometer equipped with a 1mW HeNe Laser. The TMMA-6-OH sample was prepared on a NaCl salt plate. The TMMA-6-OH functionalized ZnO NPs and the TMMA-6-OH/ZnO/Eu^{3+} complex were prepared as KBr pellets.

Fluorescence spectroscopy. The solid-state fluorescence spectra were recorded on an Edinburgh F900 photomultiplier tube equipped with a 250W Tungsten lamp. Emission spectra were acquired at an excitation of 285 nm. The samples were suspended in ethanol and drop cast on a quartz microscope slide, which were then allowed to air dry prior to measurement. The dehydrated samples were placed on a 100°C hot plate for two minutes and cooled under a stream of nitrogen prior to measurement. The hydrated samples were suspended over a beaker of steaming deionized water for two minutes, followed by immediate measurement.

Results and discussion

Design and synthesis of a ZnO-ligand-Eu^{3+} hybrid nanostructure. The absorption properties of ZnO nanoparticles and the emission properties of europium were brought together in a hybrid structure by linking these two inorganic components with an organic linker molecule. The design of the molecule incorporates both carboxylic acid and diamide functionality to tether the europium ion close to the ZnO nanoparticle surface. Carboxylic acids bind to the surface of ZnO through a carboxylate linkage.[32] Lanthanide ions are hard Lewis acids that have strong interaction to the hard oxygen donor of the diamide, or malonamide, functional group.[6,7,33] Tetramethyl malonamide (TMMA) provides a binding site for europium, is commercially available, and the acidic proton at the methylene carbon bridging the two carbonyls facilitates synthetic modification by alkylation. The amenability of TMMA allows a one-step preparation of 8-(dimethylamino)-7-(dimethylcarbamoyl)-8-oxooctanoic acid (TMMA-

6-OH), a dual function ligand that has a malonamide functionality omega to a carboxylic acid headgroup (Scheme 2.1, A). The TMMA-6-OH ligand was then used to functionalize the surface of ZnO nanoparticles following the method outlined by Hong et al (Scheme 2.1, B).[32] The ZnO-ligand-Eu^{3+} complex is formed by subsequent chelation of the TMMA-6-OH functionalized ZnO NPs to Eu^{3+} (Scheme 2.1, C), where the TMMA-6-OH ligand serves as a linker between the ZnO and Eu^{3+}.

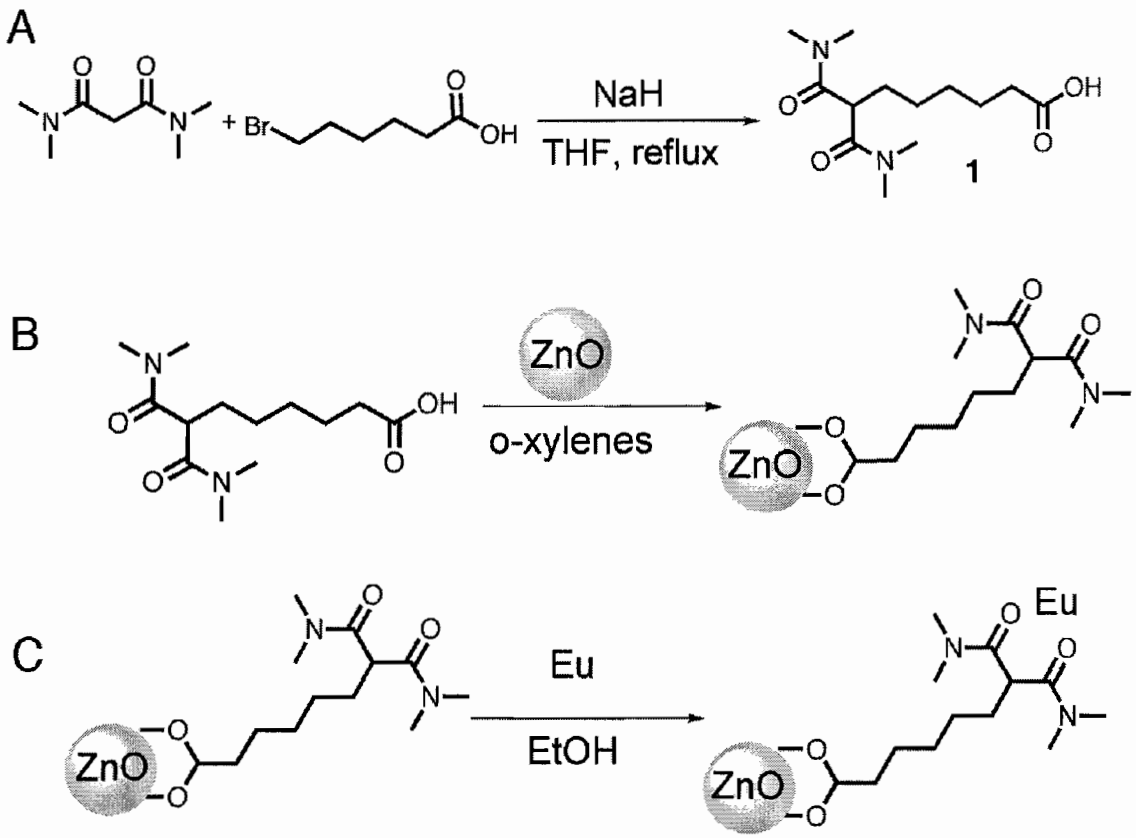

Scheme 2.1: Schematic of the ZnO-ligand-Eu^{3+} complex synthesis. Synthesis of the TMMA-6-OH ligand occurs in a single step (A), providing a molecule with malonamide functionality omega to a carboxylic acid headgroup. The TMMA-6-OH ligand was then used to modify the surface of ZnO NPs (B). The final ZnO-ligand-Eu^{3+} complex is prepared by chelating Eu^{3+} to the terminal malonamide on the ZnO surface (C).

Analysis of the ZnO-ligand-Eu^{3+} hybrid nanostructure. Fourier transform infrared (FT-IR) spectroscopy was used to monitor the successful functionalization of TMMA-6-OH to the surface of ZnO NPs, as well as the chelation of Eu^{3+} to the terminal malonamide functionality (Figure 2.2). The signature C=O stretching bands for the amide and acid carbonyl functionalities at 1728 and 1648 cm^{-1}, respectively, offer a distinct handle to compare the ligand prior to and after introduction to ZnO and europium. The asymmetric C=O stretch corresponding to the acid carbonyl on TMMA-6-OH (Figure 2.2, blue trace) is clearly present at 1728 cm^{-1}, as well as a peak at 1464 cm^{-1} ascribed to the OH stretching band for carboxylic acids.[34] These bands disappear as the TMMA-6-OH ligand binds to the surface of the ZnO NPs (Figure 2.2, magenta trace). The loss of the carboxylic acid confirms the successful functionalization of the TMMA-6-OH ligand to the ZnO nanoparticle surface. Spectra of the TMMA-6-OH functionalized ZnO NPs before and after introduction to europium remain similar by comparison, but the shift and broadening of the $\nu_{C=O}$ and ν_{C-O} regions of the spectrum at 1648 cm^{-1}, 1329 cm^{-1} and 1320 cm^{-1} suggest the Eu^{3+} ion has chelated to the terminal malonamide functionality present on the functionalized ZnO NPs (Figure 2.2, green trace). Inter-ligand and ligand-metal interactions cause these effects upon metal ion coordination[6,7] to the terminal diamide carbonyl ligand functionality. Illumination under UV light provides final confirmation that the europium ion has successfully coordinated to the terminal malonamide functionality on the ZnO nanoparticle surface. The ZnO-ligand-Eu^{3+} complex displays an intense red emission under illumination, where neither the ligand nor functionalized ZnO particles are luminescent under this condition.

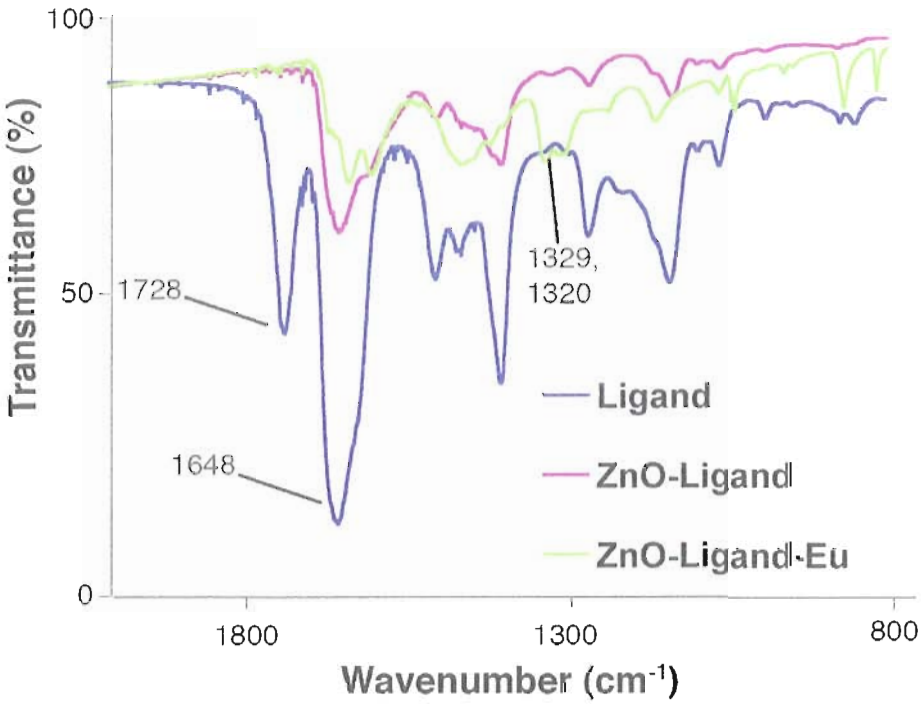

Figure 2.2: FT-IR spectra of the components used for ZnO hybrid complex formation. FT-IR is used to confirm surface functionalization and metal ion chelation for the ZnO-ligand-Eu^{3+} complex. The loss of the asymmetric C=O stretch of the carboxylic acid on the TMMA-6-OH ligand (blue trace) confirms the successful functionalization to the surface of ZnO NPs (magenta trace). The shift and broadening of the $\nu_{C=O}$ and ν_{C-O} region of the spectra confirm the chelation of Eu^{3+} to the terminal malonamide functionality (green trace).

Enhanced sensitization of europium. Successful functionalization and subsequent chelation of the TMMA-6-OH ligand to ZnO and Eu^{3+}, respectively, results in the formation of a new hybrid nanomaterial through the use of simple molecular design. Solid-state fluorescence spectroscopy was used to compare the emission

properties of $Eu(NO_3)_3$, the complex between TMMA-6-OH and Eu^{3+}, and the prepared ZnO-ligand-Eu^{3+} complex at an excitation wavelength of 285 nm.

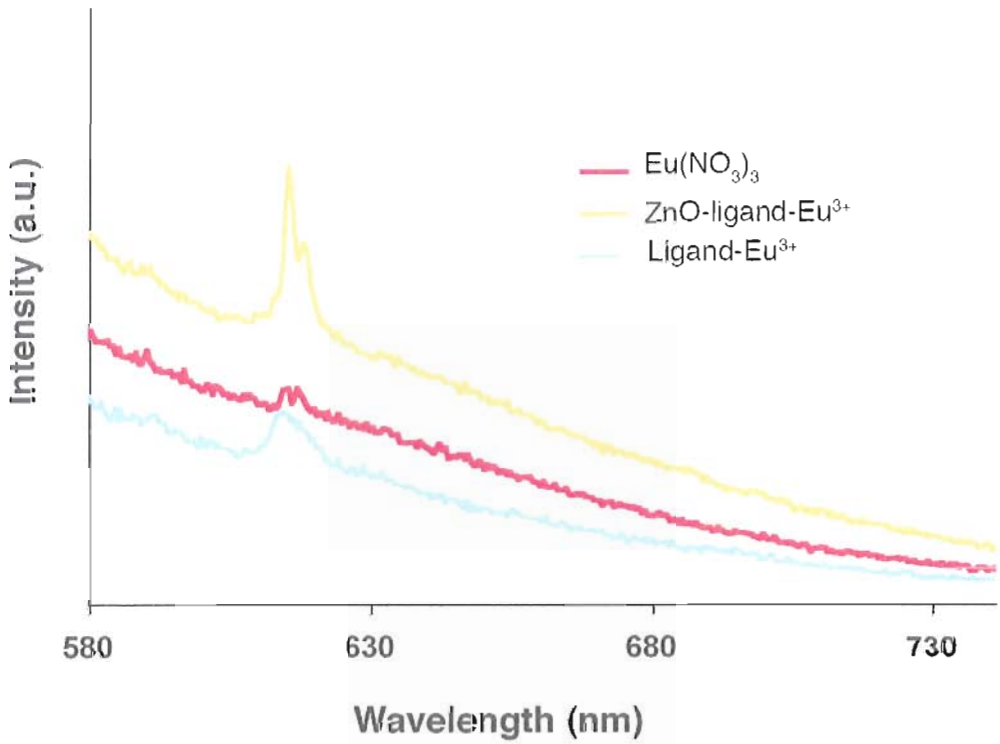

Figure 2.3: Fluorescence spectra of the components used in ZnO hybrid complex formation. A weak emission at 615 nm corresponding to the primary emission line for Eu^{3+} is observed for the free europium salt (red trace). An increase in emission at 615 nm is observed for the synthesized ZnO-TMMA-6-OH-Eu^{3+} complex (orange trace). The emission of Eu^{3+} is also increased when the ion is chelated to the TMMA-6-OH ligand without the use of ZnO (blue trace), but the increase is not as intense.

The transition from $^5D_0 \rightarrow {}^7F_2$ at 615 nm[35] corresponding to the primary Eu^{3+} emission line was measured for the ZnO-ligand-Eu^{3+} complex (Figure 2.3, orange trace). The emission was 15 times as intense as the emission recorded for the free $Eu(NO_3)_3$ salt (Figure 2.3, red trace), and 5 times as much when compared to Eu^{3+} chelated to the TMMA-6-OH ligand (Figure 2.3, blue trace). The increase in Eu^{3+} emission suggests

the transfer of energy from the ZnO NP to the bound lanthanide ion, and represents the use of a ZnO NP as an inorganic antenna. It was expected, however, that the strong absorption properties of ZnO would result in a more dramatic increase in europium sensitization than the modest increases that were observed. It was reasoned that because the final step in the preparation of the ZnO-ligand-Eu^{3+} complex involves chelation of the Eu^{3+} ion to the malonamide headgroup in refluxing ethanol, the presence of fluorescence-quenching OH oscillators were likely bound around the metal ion.[6,11,36] We therefore investigated whether removal of OH oscillators from alcohol or from atmospheric moisture would result in an enhancement over the modest increase in europium emission observed for the ZnO-ligand-Eu^{3+} complex.

Fluorescence spectroscopy was used to monitor the potential for enhanced europium sensitization when the hybrid complex was heated. The emission spectrum for the as-prepared ZnO-ligand-Eu^{3+} complex is given in Figure 2.4 (A, orange trace). The transition from $^5D_0 \rightarrow {}^7F_2$ at 615 nm[35] is present in the complex sample. When the complex is heated, however, additional emission lines corresponding to the transitions between $^5D_0 \rightarrow {}^7F_J$ (J = 1, 3, and 4) at 592, 653, and 697 nm respectively,[35] are also observed (Figure 2.4, A and B, black traces). Thermal treatment of the ZnO-ligand-Eu^{3+} complex results in a dramatic enhancement of europium sensitization. The emission of the non-heated complex increases approximately 20,000 counts from 605 nm to 615 nm. The thermally treated complex increased over 3,000,000 counts for this same wavelength range.

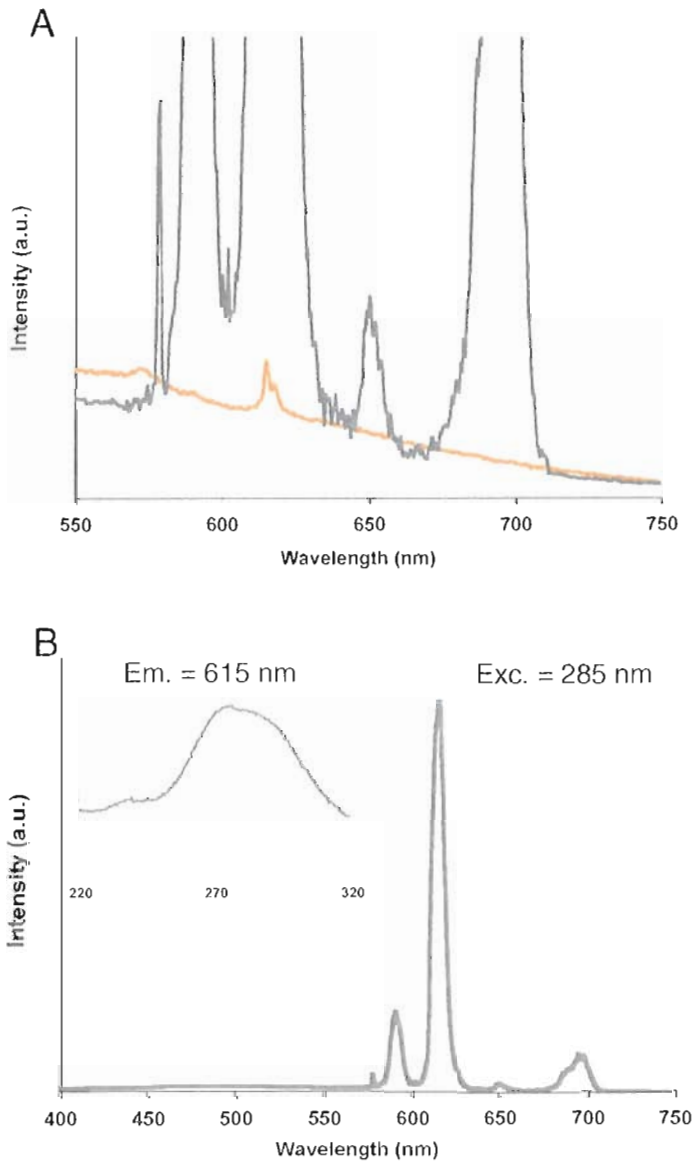

Figure 2.4: Emission and excitation spectra of TMMA-6-OH ZnO NPs after chelation with Eu^{3+}. Eu^{3+} emission at 615 nm is observed for the as-prepared ZnO-ligand-Eu^{3+} complex (A. orange trace). Thermal treatment of the complex results in an enhancement of Eu^{3+} emission (A. black trace). The transitions at 592, 615, 653, and 697 nm can clearly be measured for the complex (B) as fluorescence-quenching OH oscillators are driven off the complex through heating.

The increase in emission upon heating is attributed to the loss of luminescence quenching OH oscillators bound to the outer coordination shell of the lanthanide ion. Although this increase in sensitization has been reported for similar ZnO/lanthanide complexes, [37] the magnitude of the increase was not reported in order to compare intensities. The magnitude of the emission enhancement upon thermal treatment for our ZnO-ligand-Eu^{3+} system, however, represents over a 150 times increase in sensitization. The $^5D_0 \rightarrow {}^7F_2$ transition at 615 nm represents the majority of the total emission recorded for the system, and is consistent with lanthanide emission resulting from energy transfer by an organic chromophore antennae.[38] However, unlike many organic antennae used for sensitization, our system does not lose emission intensity from photobleaching.

Several control experiments were conducted to insure that removal of alcohol or water within the ZnO-ligand-Eu^{3+} complex resulted in the observed changes in emission, and that sensitization was due to energy transfer between the ZnO and the bound lanthanide ion. Samples of $Eu(NO_3)_3$, Eu^{3+}-bound TMMA-6-OH, and the ZnO-ligand-Eu^{3+} complex were hydrated and subsequently dehydrated while changes in emission were monitored using fluorescence spectroscopy. A distinct increase in emission was detected after thermal treatment for each of the three control samples tested (Figure 2.5, A-C). Thermal treatment of the europium salt and coordinated ligand show enhanced emission as the sample is dehydrated (Figure 2.5, A and B), confirming that the increase in emission is attributed to the loss of water during thermal treatment. Changes in the fluorescence spectra are also observed as the ZnO-ligand-Eu^{3+} complex is heated (Figure 2.5, C). However, unlike the modest change in Eu^{3+}

emission that is observed for the salt and chelated ligand, a significant difference in emission intensity occurs for the heated ZnO-ligand-Eu^{3+} complex. Europium emission can occur from the ion itself, the coordinated ligand, or the ZnO substrate. The fluorescence data suggests that negligible emission occurs from $Eu(NO_3)_3$. Similarly, the ligand chelate provides some enhancement of emission, but is insignificant compared to the complex species. The spectrum measured during these trials therefore suggests that the observed europium sensitization results not only from the influence of dehydration, but also from the transfer of absorbed energy from zinc oxide to the coordinated Eu^{3+}. One interesting observation is that no observable decline in emission intensity was reported for our system at temperatures up to 225°C. In previous reports[24] emission intensity declined upon heating beyond 80°C. Decline in emission from heated nanoparticle complexes is attributed to the increase in nanoparticle vacancies that are known to quench luminescence.[39] It is possible that passivation of the ZnO nanoparticle surface by the TMMA-6-OH ligand increases the stability of the zinc oxide surface, which helps to minimize luminescence-quenching vacancy formation.

Conclusions

In summary, we have described the preparation of a hybrid organic ZnO nanostructure that sensitizes emission from europium, resulting in a 15,000 times enhancement of europium emission over free $Eu(NO_3)_3$ salt. The synthesis of this complex represents a new class of hybrid nanomaterial made possible through the rational design and successful synthesis of an organic linker molecule that facilitates

surface functionalization to the particle surface of ZnO and coordination to Eu^{3+}. This tethers the lanthanide ion to within 12 Å to the surface of the ZnO NP. Sensitization of europium with the ZnO-ligand-Eu^{3+} complex confirms the use of ZnO as an inorganic antenna, which allows effective energy transfer between the two inorganic components to occur. Thermal treatment of the functionalized ZnO-europium complex intensifies the europium luminescence by 150 times over the non-treated sample through removal of alcohol and water bound to the coordination sphere of the lanthanide ion. The resulting luminescence from our complex is comparable to other methods of lanthanide sensitization but the simple synthesis and general design of our approach provides the advantage of a convenient strategy without compromising performance. These desirable attributes make this system a useful example for the potential utility of molecular design for the development of solid-state light emitting devices.

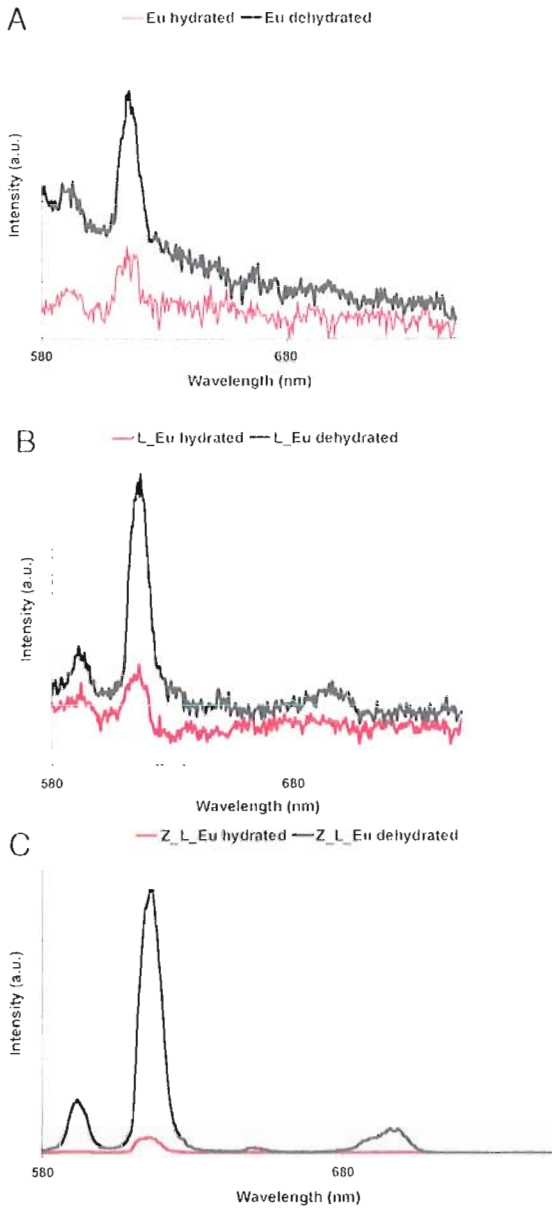

Figure 2.5: Fluorescence spectra of control experiments confirming sample dehydration impacts Eu^{3+} emission. A small increase in emission is observed when $Eu(NO_3)_3$ is heated (A). Dehydration of a TMMA-6-OH/Eu^{3+} chelate also results in a modest increase in Eu^{3+} emission (B). The intensity of the Eu^{3+} emission line at 615 nm increases as water bound to the metal ion is released upon heating. A dramatic sensitization of Eu^{3+} occurs upon the thermal treatment of the ZnO-ligand-Eu^{3+} complex (C). Dehydration of bound water intensifies the emission. but the overall enhancement as compared to the $Eu(NO_3)_3$ salt and the chelated ligand is attributed to the transfer of energy from the ZnO substrate to the bound metal ion.

Bridge

Successful design and synthesis of the TMMA-6-OH dual-function ligand demonstrated that simultaneous inorganic nanoparticle functionalization and lanthanide binding to form a hybrid organic/inorganic nanostructure was possible. The advantageous emission properties that were gained through hybridization of these organic and inorganic components encouraged us to investigate the ability to bind nanoparticles other than zinc oxide. Gold nanoparticles were chosen for several reasons. First, gold nanoparticles have interesting optical properties that have made them desirable candidates for visual, colorimetric sensors. No reports of a gold nanoparticle-based sensor for lanthanide ions had yet been reported. Secondly, Jennifer Dahl and Sam Lohse, two members of the Hutchison Laboratory, were exploring the synthesis of gold nanoparticles through the use of Bunte salt precursor ligands. It was feasible to envision the synthesis of a malonamide ligand that incorporated this Bunte salt functionality into the backbone of the molecule. This allowed us to develop a dual function ligand that used Bunte salt functionality to functionalize the surface of gold nanoparticles, and the preferred ligand-to-metal binding ratio of malonamides to lanthanide ions to control the interaction of neighboring gold nanoparticles. Chapter III describes the direct synthesis of gold nanoparticles from a malonamide Bunte salt ligand precursor, and demonstrates the use of malonamide-functionalized gold nanoparticles for selective and sensitive colorimetric sensing of lanthanide ions in water.

CHAPTER III

MALONAMIDE-FUNCTIONALIZED GOLD NANOPARTICLES FOR SELECTIVE, COLORIMETRIC SENSING OF TRIVALENT LANTHANIDE IONS

Introduction

Molecular sensors transduce analyte-binding events through chemical changes and allow selective binding and subsequent detection of species of interest. Use of these sensors has been expanding in the areas of environmental monitoring,[1,2] biological systems,[3,4] and detection of compounds related to national security.[5-8] Colorimetric sensors signal analyte binding through changes in color and are a broad class of molecular sensors that offer a convenient platform for detection. Gold nanoparticle (AuNP) sensors are a specific class of colorimetric sensor that have piqued much interest due to their unique and tunable properties.[9]

Gold nanoparticles provide an attractive substrate for the development of visual, colorimetric sensing due to their high extinction coefficients, ease of functionalization with organic ligands, photostability, and visual, colorimetric read-out.[10] Appropriately functionalized surface bound ligands can cross-link particles in the presence of an analyte or environmental response, and cause a bathochromic shift in absorbance. The resulting color change from red to blue indicates particle cross-linking[9,11-16] and offers a simple, convenient method for detection.[1,3,4,11,17-27] Examples of AuNP sensor applications include detection of biological systems such as polynucleotide detection,[28] protein modification,[4] and phosphatase activity,[3] as well as metal ion detection including lead[21,26] and mercury.[20] To develop complementary sensors we aimed to explore the utility of AuNPs incorporating designed molecular recognition sites, specifically AuNPs functionalized with diamide ligands[29,30] known to selectively bind lanthanide ions even at low pH levels.

The increased use of lanthanides in agricultural fertilizer,[31] catalysts[32,33] and medical diagnostics[34] has raised concern about their potential for pollution and warrants new methods for their detection.[35-39] In addition, there is interest in monitoring groundwater near storage tanks used to hold high level radioactive waste (HLRW),[40] and recent increased measures of national security are elevating demands for methods to sense and monitor radionuclides.[41] Traditional methods to detect lanthanide ions often are costly, non-portable, and require sophisticated instruments for analysis.[42-50] State-of-the-art inductively coupled plasma mass spectrometry (ICP-MS) and capillary electrophoresis ICP-MS offer excellent sensitivity, multi-elemental analysis, and high

sample throughput.[51-53] However, their use is limited because of the high initial investment of these approaches and required need for sample filtration and pre-concentration prior to analysis. Additionally, because such methods are not portable, samples must be taken from the field to a laboratory for analysis, which eliminates the option of real-time monitoring for applications such as groundwater contamination. Although real-time methods to monitor the presence of lanthanide ions in the field exist, including survey meters and radionuclide identifier devices, these approaches require computer-aided data analysis for analyte confirmation.[41]

A simple, portable detection method that allows rapid, real-time analysis of lanthanide ions would address many of the challenges of the instrument-intensive methods of analysis. The recent development of a phosphorescent detection strategy for europium and terbium ions based on a bipyridine functionalized nanoparticle[18] provides a potential approach to overcome some limitations of current lanthanide ion detection methods, but the surface chemistry limits the use of these functionalized particles to organic solvents, and phosphorescence-based detection of the ions requires use of a UV light source. We sought to develop a portable, qualitative molecular sensor capable of detecting lanthanide ions without the restrictions described above in order to increase the speed and convenience of sample analysis. Specifically, our objective was to develop a direct synthetic method to access malonamide-functionalized gold nanoparticles for rapid and selective optical detection of trivalent lanthanide ions in water.

Use of a masked thiol, or Bunte salt functionality, provides a direct synthetic method to access larger (d_{core} > 3 nm) AuNP core sizes.[54] Bunte salts have been shown to simultaneously provide access to large AuNPs and offer stabilization to the synthesized particles in water or organic solution.[55,56] The malonamide class of ligands enabled selective binding of Ln^{3+} ions and provided access to controlled particle aggregation. Acyclic malonamides have been used for the extraction of lanthanides and actinides in both high- and low-level radioactive waste,[29,57] and their known 2:1 ligand:metal binding ratio[58,59] offers control of the aggregation of nanoparticles through binding of two ligands and one lanthanide ion. Cross-linking of particles through the 2:1 L:M binding of the malonamide should result in coupling of AuNP plasmons and change the color of the nanoparticle solution from red to blue. Water and organic soluble malonamides can be synthesized, which offers flexibility for further synthetic modification.

Herein we report the design and synthesis of a colorimetric gold nanoparticle sensor selective for Ln^{3+} ions. The Bunte salt analog of 2-(3-hydroxyheptyl)-N^1,N^1,N^3,N^3-tetramethylmalonamide (MHTMMA) contains both thiosulfate and malonamide functionalities and allows a AuNP sensor that is selective for lanthanide ions to be produced in a single, direct step (Scheme 3.1). Incorporation of the lanthanide binding functionality on the particle surface during formation eliminates the need for an additional ligand exchange step, reducing time, energy, and solvent waste during synthesis. The as-synthesized MHTMMA functionalized AuNPs are stable in water in a range of pH levels (3.5-11) without the need for additional buffers as stabilizing

agents. Results show that the MHTMMA functionalized AuNPs bind lanthanide ions in water and result in an immediate, visual change in color from red to blue. The functionalized nanoparticles bind Ln^{3+} ions selectively, and no particle aggregation was observed when the MHTMMA particles were introduced to other environmentally relevant ions. The MHTMMA functionalized AuNPs offer excellent sensitivity, detecting Ln^{3+} ions with detection limits of ~ 50 nM.

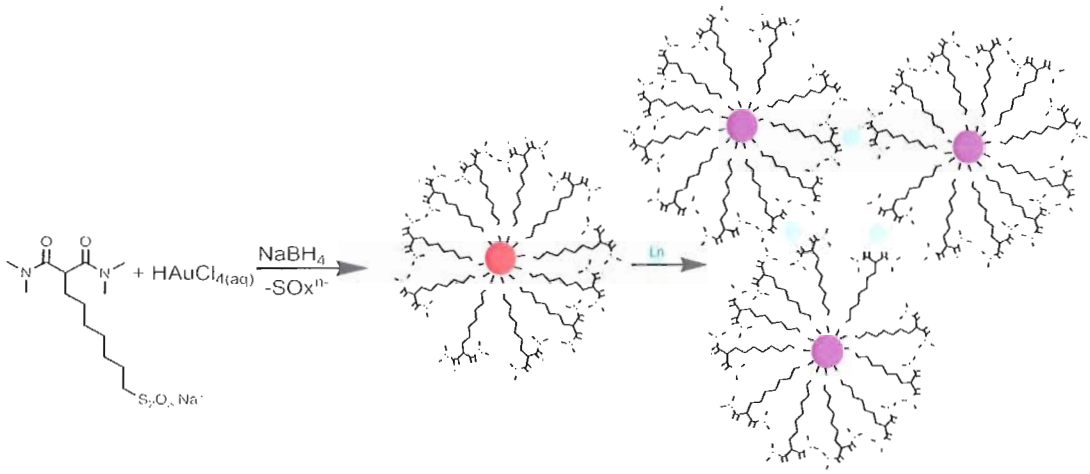

Scheme 3.1: Synthesis of malonamide-functionalized AuNPs and NP cross-linking through Ln^{3+} binding. $NaBH_4$ is added to a mixture of the Bunte salt analog of MHTMMA and $HAuCl_4$ to produce the MHTMMA protected AuNPs. The MHTMMA AuNPs perform as an optical sensor and change color from red to blue when Ln^{3+} is added to the NP solution. The terminal TMMA functionality initiates NP cross-linking through Ln^{3+} ion binding. The NPs come into close proximity such and their surface plasmons interact resulting in a red-shifted change in absorbance.

Experimental methods

Materials. Tetramethylmalonamide was obtained from TCI-EP (Tokyo, Japan). Phosphorus tribromide was distilled and maintained under nitrogen prior to use. Hydrogen tetrachloroaurate was obtained from Alfa Aesar. All other reagents were obtained from Aldrich and used without further purification. Dichloromethane was distilled from calcium hydride prior to use. Tetrahydrofuran was distilled from potassium prior to use. Deionized water (18.2 MΩ-cm) was purified with a Barnstead Nanopure Diamond system.

Synthetic procedures. *2-(3-hydroxyheptyl)-N^1,N^1,N^3,N^3-tetramethylmalonamide, **1**.* Sodium hydride (0.31 g, 12.9 mmol) was dissolved in 100 mL distilled THF in a 250-mL round-bottomed flask equipped with a stir bar. TMMA (1.92 g, 12.1 mmol) was added, followed by dropwise addition of $Br(CH_2)_7OH$ (2.01 g, 10.3 mmol) in 10 mL of THF resulting in a thick white slurry. The reaction mixture was stirred at reflux for 16 hours. Deionized H_2O (1 mL) was added to quench the excess NaH, and the mixture was reduced to 10 mL using rotary evaporation. Dichloromethane (150 mL) was added, and the organic layer was washed with 100 mL of deionized H_2O, 50 mL of 10% $HCl_{(aq)}$, 2 x 100 mL of saturated $NaHCO_{3\,(aq)}$, and 2 x 100 mL of saturated $NaCl_{(aq)}$. The organic layer was dried over Na_2SO_4 and the solvent was removed by rotary evaporation to afford alcohol **1** as a clear, colorless oil (2.6 g, 98%). ^1H NMR ($CDCl_3$) δ1.31 (br d, 6H), 1.53 (q, 2H), 1.87 (q, 2H), 2.97 (d, 12H), 3.61 (m, 3H).

*2-(3-bromoheptyl)-N^1,N^1,N^3,N^3-tetramethylmalonamide, **2**.* Under nitrogen, alcohol **1** (2.6 g, 7.9 mmol) was dissolved in 25 mL of distilled dichloromethane in a 50-mL round-bottom flask equipped with a stir bar. PBr_3 (0.19 mL, 2.0 mmol) was added, and the reaction mixture allowed to stir at room temperature for 16 hours. The resulting mixture was washed with 50 mL 10% $HCl_{(aq)}$, 2 x 100 mL saturated $NaHCO_{3\,(aq)}$, 100 mL deionized H_2O, and 2 x 100 mL saturated $NaCl_{(aq)}$. The organic layer was dried over Na_2SO_4, and the solvent removed using rotary evaporation to afford bromoalkane, **2**, as a clear, colorless oil (2.6 g, 84%). ^{1}H NMR ($CDCl_3$) δ1.31 (br d, 6H), 1.53 (q, 2H), 1.87 (q, 2H), 2.97 (d, 12H), 3.36 (br t, 2H), 3.61 (t, 1H).

*Synthesis of Bunte salt analog of 2-(7-mercaptoheptyl)-N^1,N^1,N^3,N^3-tetramethylmalonamide (MHTMMA), **3**.* Bromoalkane **2** (2.57 g, 6.6 mmol) was dissolved in a mixture of 40 mL of EtOH and 10 mL of deionized H_2O in a 100-mL round-bottom flask equipped with a stir bar. $Na_2S_2O_3$ (1.04 g, 6.0 mmol) was added to the reaction mixture and brought to reflux for 3 hrs. The solvent was removed via rotary evaporation, and further evaporated under high vacuum for an additional 24 hrs. The resulting oil was triturated with 5 x 5 mL of EtOH and the remaining solvent removed via rotary evaporation to afford the Bunte salt, MHTMMA (**3**), as a clear, viscous oil (2.94 g, 87%). ^{1}H NMR ($CDCl_3$) δ1.31 (br d, 6H), 1.53 (q, 2H), 1.87 (q, 2H), 2.97 (d, 12H), 3.42 (t, 1H), 3.50 (q, 2H).

Synthesis of MHTMMA functionalized gold nanoparticles. To an aqua regia (3:1 $HCl:H_2SO_4$) cleaned 250 round bottom flask equipped with a stir bar 100 mL of Nanopure H_2O, 1 mL of 0.1 M $HAuCl_4 \bullet xH_2O$, and 500 uL of a 0.1 M MHTMMA

solution was added. After the reaction mixture was allowed to stir for 10 minutes, 2.0 mL of freshly prepared 0.1 M $NaBH_4$ was added. The reaction mixture was allowed to stir for 3 hours. The resulting dark red solution was filtered through a coarse-fritted glass funnel and purified via diafiltration with twenty volume equivalents of Nanopure water through a 70K Pall Corporation membrane.[60]

Analytical procedures. Nanoparticles were characterized using a combination of transmission electron microscopy and UV-visible spectroscopy.

Transmission electron microscopy (TEM). TEM analysis was performed on a Philips CM-12 Transmission Electron Microscope. AuNP samples were prepared for analysis by floating amine-functionalized Smart Grids™ (Dune Sciences) on top of a droplet of purified MHTMMA AuNP solution for 1 minute then rinsing with copious amounts of Nanopure water. The grid was placed in a desiccator and allowed to dry overnight. After scanning the whole grid, five images were taken for each sample on various places on the TEM grid to ensure a representative sample. Images were taken at 125 kX magnification, and a minimum of 600 nanoparticles per image was used for size analysis. The images were then processed using Image J software to determine average core diameter, size distribution and standard deviation following the literature method.[33]

UV-visible (UV-vis) spectroscopy. All measurements were performed using a Mikropack DH-2000 UV-vis-NIR light source equipped with an Ocean Optics USB2000 spectrophotometer. Absorbance was measured using purified MHTMMA AuNPs in a quartz cuvette that was cleaned with aqua regia and rinsed with copious amounts of Nanopure water in between all measurements. Experiments that included

NP dilutions were carried out using Nanopure water and were prepared to one-half the as-synthesized NP concentration (2:1 H_2O:NP).

Selectivity trials. Experiments to measure binding to Ln^{3+} ions over potentially conflicting metal ions were performed using purified MHTMMA nanoparticles that were diluted to one half the as-synthesized nanoparticle concentration (1:1 NP:H_2O, 2 mL total volume). Aqueous solutions (0.1 mM) of lanthanide nitrate salts (Ln = La, Ce, Nd, Sm, Eu, Gd, Tb, Ho, and Er) were prepared in Nanopure water. A 20-uL aliquot of the lanthanide solution was added to the nanoparticle solution while stirring, and the absorbance spectra were recorded. The cuvette was rinsed with aqua regia and copious amounts of Nanopure water between trials. Assessment of selectivity for competing non-lanthanide ions was performed by adding 0.1 mM solutions of $Fe(NO_3)_3$, $Pb(NO_3)_3$, $CdCl_2$, $CrCl_3$, $CuCl_2$, CsF, NaCl, or KCl, and recording absorbance using the same method as for the lanthanide ions.

Determination of response time. To determine the time needed for lanthanide ion binding, 0.75 mL of MHTMMA AuNPs and 0.75 mL of deionized Nanopure water were added to a 3 mL quartz cuvette equipped with a stir bar. To the rapidly stirring NP solution, 150 uL of a 0.1mM solution of Eu^{3+} was added. The absorbance spectra was recorded every second for three minutes. Following data acquisition, the absorbance at 620 nm was plotted versus time to determine the response time.

Determination of detection limit. The detection limit was determined through a spectral titration monitored via UV-vis. The absorbance spectrum of 2 mL of purified MHTMMA AuNPs was used as the blank. Successive aliquots of a 0.1 mM $Eu(NO_3)_3$

$_{(aq)}$ stock solution were added to the rapidly stirring nanoparticles, and the absorbance spectra recorded after each addition. A total of 12 aliquots of 0.1 mM $Eu(NO_3)_{3\ (aq)}$ were added during the titration (20 uL total, 10 successive 1 uL additions followed by two 5 uL additions), and the concentration of Eu^{3+}in the sample was calculated after each addition. Plotting the calculated Eu^{3+} concentration versus the absorbance at 620 nm determined the detection limit, which was defined as the minimum concentration of Eu^{3+} that caused an observable absorbance at 620 nm.

Results and discussion

Synthesis of MHTMMA functionalized AuNPs. We incorporated thiosulfate and malonamide functionality into MHTMMA to stabilize the AuNP during and after growth, and simultaneously provide a binding site for lanthanide ions. The passivation of the gold surface by the thiosulfate functionality occurs more slowly than that of a thiol, and allows access to nanoparticles with core diameters greater than 3 nm.[56] This is an important consideration for AuNP-based sensing application as it is beyond this core size that the surface plasmon absorption becomes prominent at 520 nm.[13] In addition to providing direct access to larger Au core sizes, the solubility of Bunte salts can be tuned, which offers a route to AuNPs that can be synthesized and utilized in water. These ligands provide for synthesis and stabilization of the Au core, and remain amenable to further synthetic modification. Subsequent ligand exchanges are not required, thus greatly increasing the synthetic convenience while reducing time, synthetic efforts and solvent needed during nanoparticle formation. Additionally, Bunte

salts are shelf-stable and do not produce strong odors that their thiol analogs do. We have stored synthesized Bunte salt ligands at room temperature for over a year with no signs of degradation.

The Bunte salt analog of 2-(7-mercaptoheptyl)-N^1, N^1, N^3, N^3-tetramethylmalonamide (MHTMMA) containing the malonamide functionality omega to the thiosulfate head group is easy to prepare (Scheme 3.2). Tetramethylmalonamide (TMMA) was first alkylated with the bromoheptylalcohol to yield alcohol **1** which was brominated using phosphorus tribromide, and subsequently converted to the Bunte salt following the method outlined by Shon *et al.*[56] This three-step sequence provides the MHTMMA ligand in an overall 72% yield. The methyl groups on the malonamide enhance water solubility, and the acidic proton at the methylene carbon bridging the two carbonyls in TMMA facilitates synthetic modification by alkylation.

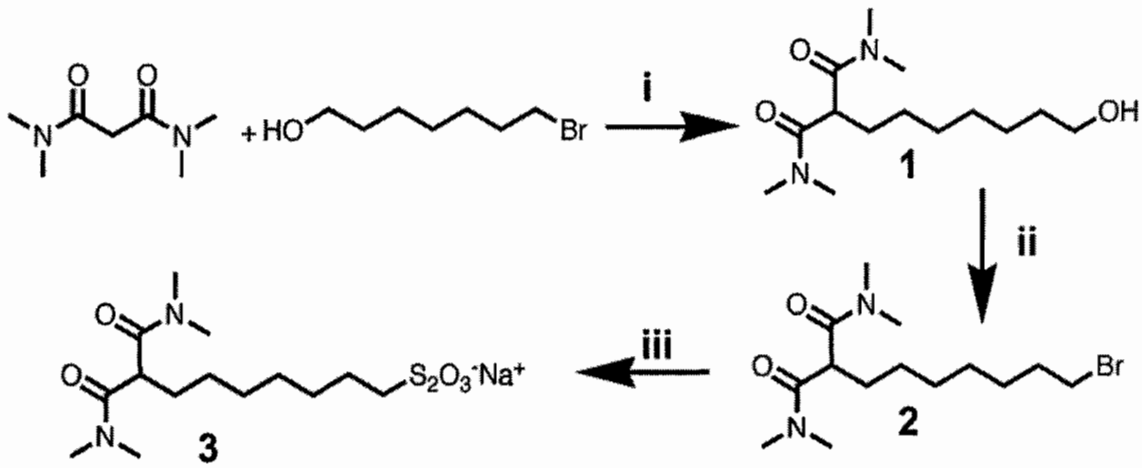

Scheme 3.2: Synthesis of the Bunte salt used to prepare MHTMMA stabilized AuNPs used for this study. (i) NaH, THF (ii) PBr_3, CH_2Cl_2 (iii) $Na_2S_2O_3$, EtOH, H_2O.

Reduction of an aqueous mixture of hydrogen tetrachloroaurate in the presence of MHTMMA ligand[a] results in direct synthesis of a AuNP sensor. Upon reduction the solution turns from yellow to dark brown and then to deep red, indicating the formation of nanoparticles. After stirring for three hours, the nanoparticles are purified by diafiltration to remove unreacted gold salt, unbound ligands, and other by-products.[60] Thorough purification is particularly important because free malonamide will compete with the nanoparticles in binding the Ln^{3+} analyte. The purified NPs are deep red in color, and stable in water. The MHTMMA particles have remained dispersed in solution without additional stabilizing buffers for over 6 months with no signs of degradation or particle aggregation. The absorption spectra of MHTMMA AuNPs in water (Figure 3.1) reveal the plasmon absorption centered at 520 nm that suggests the nanoparticles are greater than 3 nm in size. TEM images (Figure 3.1) show that the nanoparticles are 6.8 +/- 1.7 nm in diameter, spherical in shape, and well dispersed on the grid. These results confirm successful synthesis of MHTMMA AuNPs and, to our knowledge, constitute the first report of utilization of Bunte salt ligands to directly introduce terminal functionality designed for Ln^{3+} ion sensing during formation of AuNPs.

---

[a] Synthetic trials experimenting with the length of the alkyl spacer between the TMMA and thiosulfate groups were performed, and the seven-carbon spacer met the requirements of stabilization to the Au core, desired solubility in water, and successful Ln^{3+} binding.

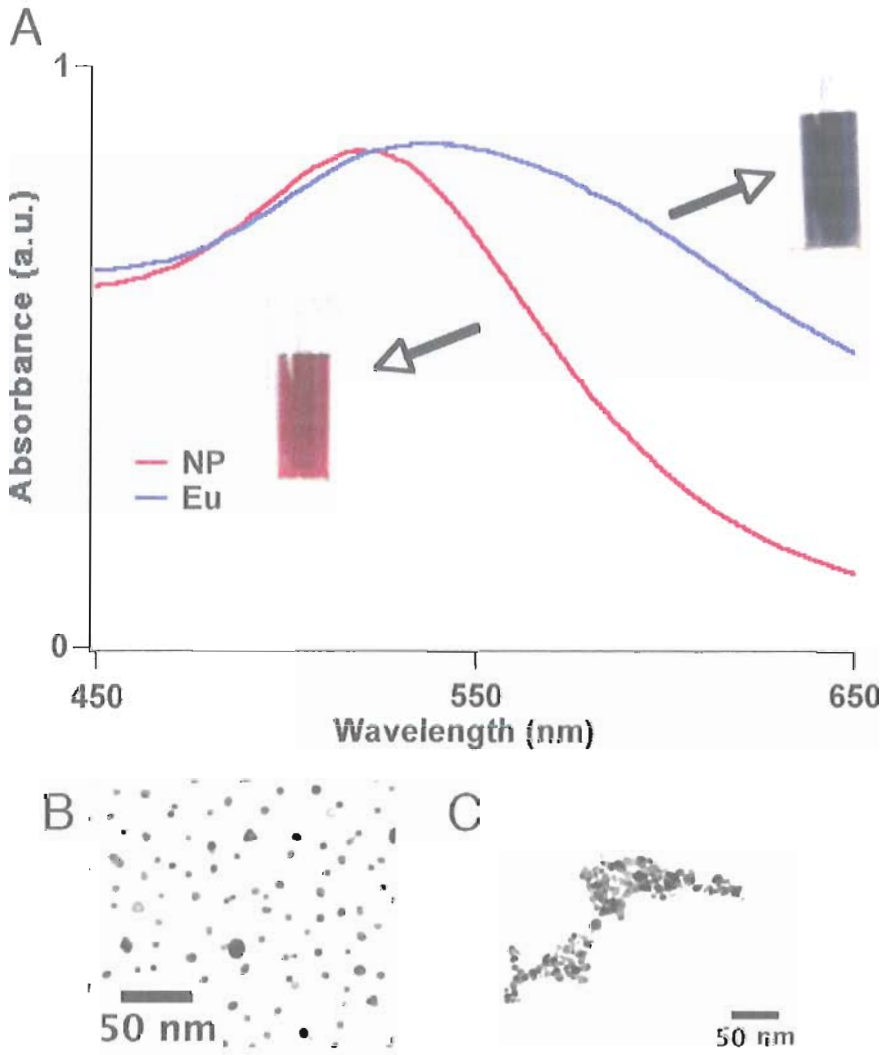

Figure 3.1: Absorbance spectra, aggregation of MHTMMA AuNPs, and corresponding color change upon introduction of Eu^{3+} ions to solution. MHTMMA AuNPs are red in color and show the characteristic plasmon absorbance at 520 nm (A, red trace) for large AuNPs. TEM images (B) of the MHTMMA AuNPs show the NPs to be dispersed in solution and have a mean core diameter of 6.8 ± 1.7 nm. After $Eu(NO_3)_3$ is added to the MHTMMA AuNP solution the absorbance shifts and broadens (A, blue trace) correlating with a color change to blue. The increase in the baseline indicates the scattering of light due to the formation of nanoparticle aggregates, which are confirmed by TEM (C).

Confirmation of Ln^{3+} binding as the mechanism for NP aggregation.

Solution-based investigations confirmed that MHTMMA nanoparticles aggregate in the presence of Ln^{3+} ions and that the mechanism was direct binding of TMMA ligands to these ions. Absorbance spectra and TEM images showed unambiguous changes with the addition of a solution of Eu^{3+} ion (Figure 3.1). Upon addition of an aliquot of $Eu(NO_3)_3$ to the MHTMMA functionalized AuNPs, an immediate, visible color change from red to blue occurred. In the UV-vis spectrum the plasmon absorption at 520 nm diminished and broadened in comparison with the dispersed nanoparticle solution. These spectral signatures have been observed in analogous systems and are due to the varied size distribution of the aggregated species.[24] The color change and resulting shift of the plasmon suggests that nanoparticles are being cross-linked through binding by Eu^{3+} ions. Additionally, the increased baseline in these samples suggests scattering of light by the large nanoparticle aggregates in solution. TEM images show these aggregated nanoparticles and confirm cross-linking under these conditions.

Several control experiments confirmed that the nanoparticle aggregation is a consequence of bridging between MHTMMA ligands on neighboring NPs by Eu^{3+} ions as opposed to non-specific interactions (e.g. aggregation around counter ions or binding to non-Ln metals). To establish that the observed nanoparticle aggregation and color change resulted from lanthanide binding, we added uranyl ion to the MHTMMA nanoparticles. Because malonamide ligands bind to the uranyl ion in a preferred 1:1 L:M binding ratio,[61] we would not expect nanoparticle cross-linking to occur in its presence. As shown in Figure 3.2, the addition of 20 uL of a 0.1 mM aqueous solution

of uranyl nitrate resulted in no color change and no noticeable shift in the position of the surface plasmon band in the absorbance spectrum. TEM images taken before and after addition of UO_2 further confirm that particles are not aggregating around this ion, as the particles remain dispersed on the surface of the grid.

The addition of excess $HAuCl_4$ to the purified MHTMMA AuNP solution served as a second control experiment to confirm that any remaining gold salt in the particle solution would not interfere with particle binding. The images of the solutions in Figure 3.2 (B, 1-4) show the changes in color of the nanoparticle solution from the as-synthesized red color to a yellow/brown color. The absorbance spectrum reveals a very high absorbance in the lower wavelength region that indicates an excess of Au^{3+} ions, however, the plasmon remains distinct with no indication of aggregation. A slight narrowing and red shift of the plasmon can be attributed to the presence of large, polydisperse AuNPs. TEM images taken after addition of $HAuCl_4$ support the presence of large particles of various shapes but do not show signs of nanoparticle aggregation. Although no further experiments were performed to explore the mechanism of AuNP growth, spectral and digital results confirm that the color and absorbance changes monitored for this system were not a result of the MHTMMA AuNPs binding to excess Au^{3+} ions.

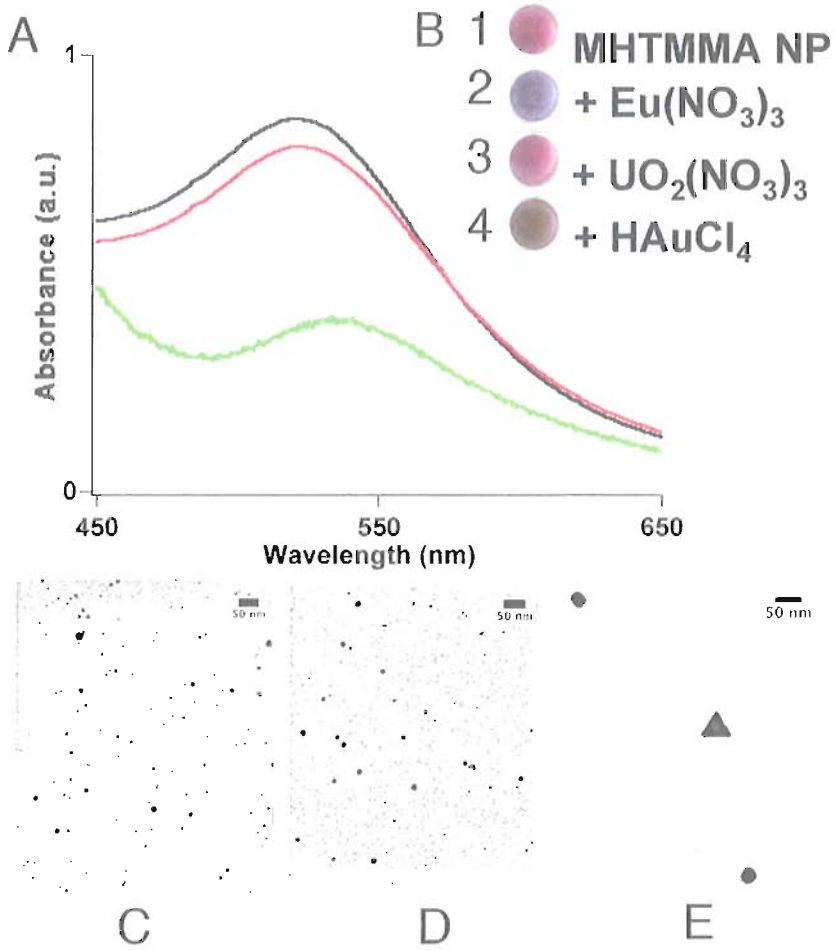

Figure 3.2: Spectral changes, color response, and micrographs of MHTMMA AuNPs after incubation with uranyl nitrate and excess $HAuCl_4$. In order to assess the difference between simple ion binding and cross linking, an ion known to bind to the TMMA in a 1:1 L:M ratio was added to the NP solution. A 1000 nM aliquot of $UO_2(NO_3)_3$ was added to the MHTMMA AuNPs in the same manner as trials performed with both the selected Ln^{3+} ions and interfering ions (Figures 3 and 4, respectively). Upon addition of the UO_2, no changes in MHTMMA AuNP absorbance (A, red trace) or color (B, 3) are noted. A MHTMMA AuNP sample treated with $Eu(NO_3)_3$ is shown for comparison (B, 2). TEM reveals the NPs to be dispersed prior to (C) and after UO_2 addition (D) that is in line with the results of the study. As a second control, excess $HAuCl_4$ was added to the MHTMMA AuNPs post synthesis and purification. Immediately upon addition of the Au salt, the NP solution becomes yellow-brown in color (B, 4). The UV-vis spectrum (A, green trace) shows a large absorbance at 430 nm, indicative of excess Au. The shift in absorbance from 520 nm to 540 nm indicates larger NP species. The micrograph (E) supports the presence of large NP species, as NPs in excess of 50-nm are present throughout the grid.

Results from the uranyl nitrate and gold salt additions suggest the MHTMMA-AuNP aggregation observed with lanthanide ions result from the binding of MHTMMA ligands to the Eu^{3+} ions, which drives the nanoparticle aggregation, absorbance shift, and subsequent color change to occur. In order to evaluate the binding preference of the MHTMMA AuNPs to metals other than europium, experiments involving additional lanthanide ions as well as selected non-rare earth ions were performed.

Determination of MHTMMA AuNP selectivity and response time.

Lanthanide ions are hard Lewis acids which should have a strong interaction to the hard oxygen donor of the amide functionality.[62] To determine if this interaction would provide selectivity for Ln^{3+} ions over other metals, we first tested the response of the MHTMMA AuNPs to additional Ln^{3+} ions. Results from trials evaluating the spectral response of the MHTMMA AuNPs to 20-uL aliquots of a 0.1 mM solution of the nitrate salts of all trivalent lanthanide ions tested (La, Nd, Sm, Eu, Gd, Tb, Ho, and Er) are shown in Figure 3.3. The position of the plasmon band shifts from 520 nm to 540 nm and shows the characteristic broadening and rise above the baseline. The resulting absorbance changes are analogous to the Eu^{3+} trials and indicate that the MHTMMA sensor shows little selectivity across the lanthanide series. A possible explanation for the lack of discretion among lanthanide ions is the high relative concentration of TMMA binding sites as compared with available Ln^{3+} ions. Studies have shown malonamides to display different binding affinities for different lanthanide ions.[63] Introducing a lower malonamide density on the nanoparticles through incorporation of a mixed ligand shell on the particle surface may facilitate lanthanide selectivity and result

in a distinct plasmon signature for each individual ion, as has been shown in the literature for several toxic heavy metal ions.[24]

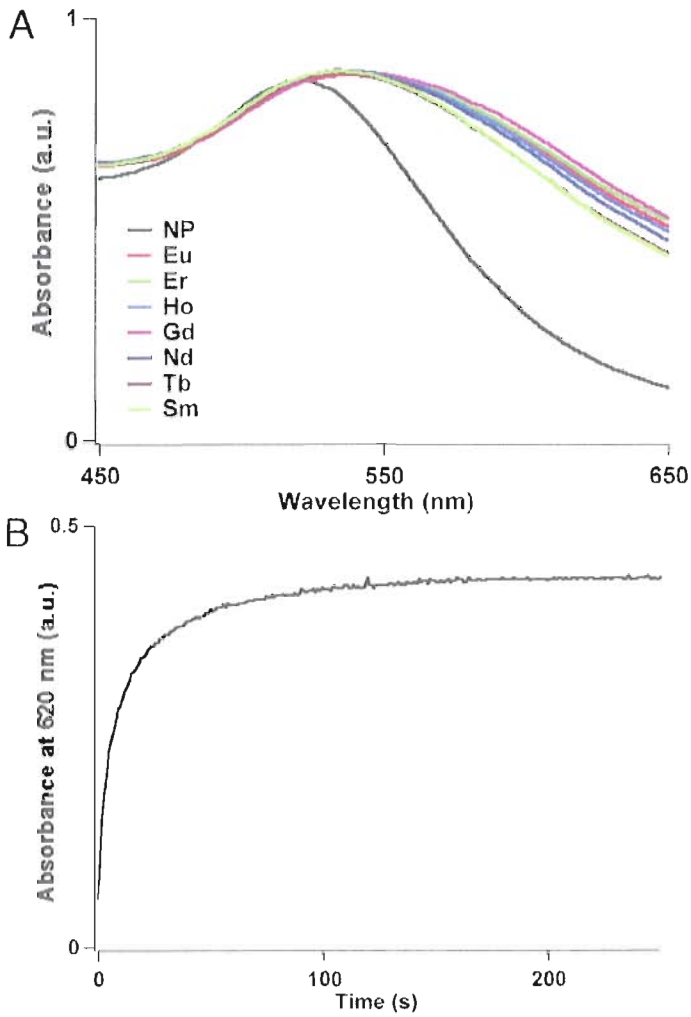

Figure 3.3: Spectral and temporal response of MHTMMA AuNPs to Ln^{3+} ions. When introduced to select Ln^{3+} ions the MHTMMA AuNPs show a distinct shift and broadening in absorbance (A) compared to the initial AuNP solution (isolated, black trace). The terminal TMMA functionality binds to all tested Ln^{3+} ions, effectively allowing the NPs to come within close proximity such that plasmon coupling may occur. The response time of the resulting absorbance change occurs instantly and saturates within a few minutes (B). The spectrum shown is for the response to a 150uL addition of a 0.1 mM Eu^{3+} solution (results were similar for all Ln^{3+} tested).

The temporal response of the sensor was measured by monitoring a region of the absorbance spectra corresponding to cross-linked nanoparticles and plotting the change in absorbance over time. The absorbance at 620 nm was chosen because it corresponds to Eu^{3+}-bound particles. Figure 3.3 B shows the temporal response after 150 uL of a 0.1 mM solution of $Eu(NO_3)_3$ was added to MHTMMA AuNPs. The onset of absorbance and subsequent color change occurs instantaneously and becomes saturated after approximately 120 seconds. The immediate response of MHTMMA particles is identical to the reported time for metal ion detection of peptide-functionalized AuNPs.[24] No changes in the response time of the MHTMMA AuNPs were detected when the particles were diluted to one-half of their synthesized concentration. This study shows that MHTMMA AuNPs can be used for visual, rapid detection of Ln^{3+} ions in water. In order to determine the overall potential application for our sensor we also tested the sensor's sensitivity to non-rare earth ions.

For the MHTMMA functionalized AuNPs to be considered for sensing applications in natural samples, the particles must provide selective binding for lanthanide ions in the presence of other metal ions that could compete for binding sites on the MHTMMA particles. Absorbance spectra and images of nanoparticle samples after 20-uL additions of 0.1 mM metal ion solutions are shown in Figure 3.4. Investigations of the colorimetric response to various metal ions determined the selectivity of the MHTMMA AuNPs as Ln^{3+} sensors.

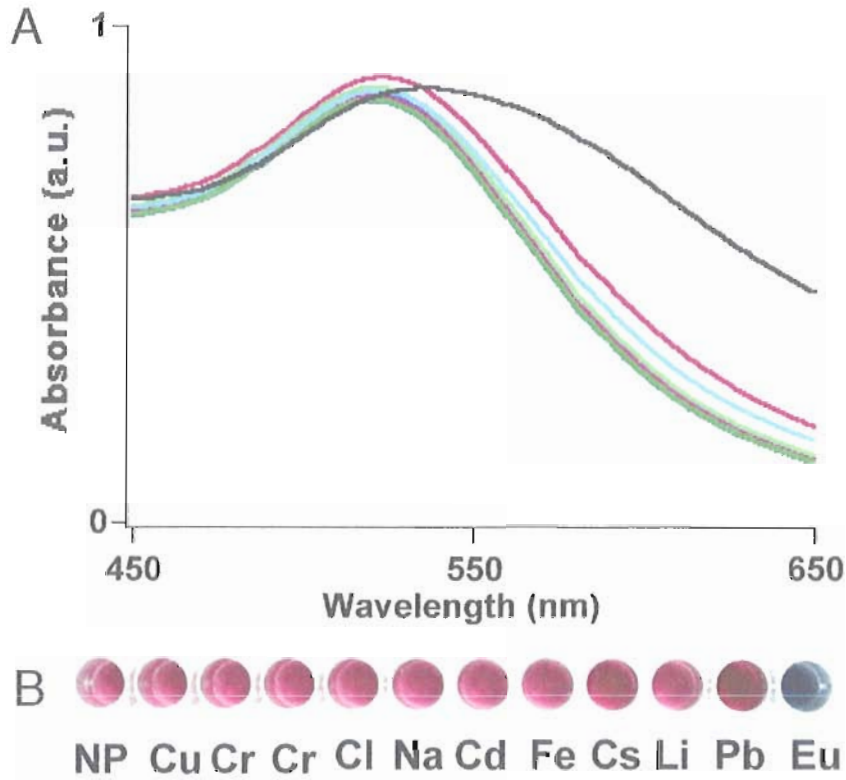

Figure 3.4: Spectral and color response of MHTMMA AuNPs to the addition of selected interfering metal ions. In order to assess binding preference of the MHTMMA AuNPs selected interfering ions were added to the NP solutions. The absorbance spectra (A) and color of NP solutions (B) remains unchanged after 1000 nM additions of each metal ion. The addition of 1000 nM Eu^{3+} to the MHTMMA AuNP solution is given as a comparison. Note the significant shift and broadening of the absorbance spectra (A, black trace) and the distinct color change (B) from red to blue upon addition of the Ln^{3+} ion.

The MHTMMA functionalized AuNPs showed no affinity for environmentally relevant samples of hard and soft metal ions in varying oxidation state (Cu^{2+}, Cr^{3+}, Cr^{6+}, Cl^{+}, Na^{+}, Cd^{2+}, Fe^{3+}, Cs^{+}, Li^{+}, and Pb^{3+}). No color change or shift in the absorbance at 520

nm occurred upon addition of these ions which suggests this system has a preferential selectivity for Ln^{3+} ions under the conditions tested.[b]

Determination of detection limit for Ln^{3+} binding. Titration of a 0.1 mM $Eu(NO_3)_3$ solution into the MHTMMA particles enabled the quantitative evaluation of the sensitivity that derives from particle binding to lanthanide ions. Figure 3.5 shows the absorbance spectra and plot of the change in absorbance upon addition of Eu^{3+} to the particles. The decrease in the absorbance at 520 nm and the appearance of an absorbance in the region of the spectra corresponding to Eu^{3+}-bound nanoparticles (620 nm) were monitored. The addition of only 2 uL of 0.1 mM Eu^{3+} resulted in a detectable increase in absorbance at 620 nm. The minimum concentration of Ln^{3+} that produced a detectable change in absorbance determined the detection limit of the sensor. These results are, to the best of our knowledge, the lowest reported detection limits for a selective colorimetric lanthanide ion sensor to date, and the low limits of detection are within the same order of magnitude as other AuNP based sensors utilizing biological molecules for metal ion recognition.[19,22,24] The titration data show the low and high limits of the working, or dynamic, range of the Eu^{3+}-bound nanoparticles to be 50 nM and 496 nM, respectively (Figure 3.5, B). An additional UV-vis titration using $Sm(NO_3)_3$ determined a detection limit to be 50 nM.

---

[b] It should be noted that the selectivity of the MHTMMA NPs declines as metal ion concentrations increase, as an aliquot of 1 M Pb^{3+} induced a color change in the particle solution. This is not expected to impact the utility of the sensor, as the level of this ion is typically in the parts per billion range, well below the concentration that induced particle interaction.

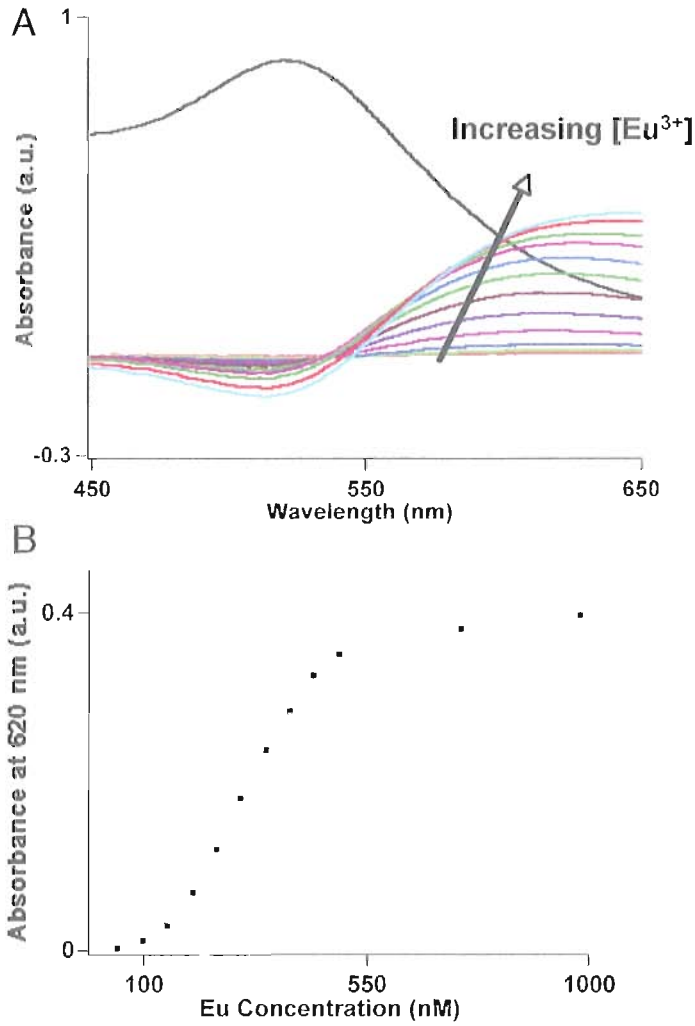

Figure 3.5: Spectral titration and resulting A vs. Eu concentration data that define the dynamic range of the MHTMMA AuNP sensor to Eu^{3+}. A UV-vis titration (A) was performed to determine the absorbance change as subsequent aliquots of Eu^{3+} were added to the MHTMMA AuNPs. An initial spectrum of the MHTMMA AuNPs was recorded (displayed as the isolated, black trace) and this solution was used as the blank. Upon addition of the Ln^{3+} solution, one can monitor either the loss of absorbance at 520 nm or the increase in the longer wavelength absorbance resulting from the interaction of surface plasmons of the particles. From the titration data, the absorbance at a single wavelength (620 nm) can be plotted as a function of concentration for the added Ln^{3+} metal ion (B) to determine the dynamic range of the sensor. The low limit of the sensor correlates to the detection limit of the system, and was determined to be 50 nM. In this sample the upper limit was 495 nM. Although the lower limit remained constant, the upper limit decreases as the concentration of nanoparticles increases.

Titrations performed with more concentrated samples of nanoparticles yield smaller dynamic ranges because, although the lower limit of detection appears unchanged, the upper limit trends to lower Ln^{3+} concentrations. At higher concentrations of nanoparticles the colorimetric change is more distinct, an attribute that could be of use in situations where semi-quantitative detection is needed, such as in the field where detection relies on visual assessment and access to UV-vis spectroscopy is unattainable. It may be possible to tune the dynamic range of these nanoparticle sensors through redesign of the lanthanide binding site or by diluting the binding sites within the ligand shell. Synthetic modification of the ligand to introduce bulky alkyl groups in place of the methyl groups may extend the upper limits of the dynamic range. Another approach to lowering the detection limit that we are currently exploring is the use of a stronger lanthanide binding ligand such as the bicyclic malonamide.[64] Finally, experiments to determine whether it may also be possible to tune the limits of the dynamic range by using a mixed ligand composition on the nanoparticle surface have begun. AuNPs functionalized with a ligand having no known binding affinity for lanthanide ions and a small number of malonamide ligands may allow the surface chemistry to be modified for specific applications that require a variety of detection levels.

Conclusions

The use of the Bunte salt analog of 2-(7-mercaptoheptyl)-N^1, N^1, N^3, N^3-tetramethylmalonamide (MHTMMA) affords access to functionalized AuNPs that can

detect the presence of Eu^{3+} at concentrations as low as 50 nM, which is the lowest reported detection for lanthanide ion colorimetric sensing. The rapid, selective, and sensitive response to lanthanide ions suggests this sensor may have potential application in the monitoring and detection for these ions in the environment. The nanoparticles selectively bind Ln^{3+} ions over a variety of potentially interfering metal ions, causing an instantaneous color change in the nanoparticle solution from red to blue effectively performing as a visual, colorimetric sensor for Ln^{3+} ions. The one-step preparation of MHTMMA functionalized AuNPs occurs at room temperature in water and does not require additional stabilizing agents.

Identification of several target attributes led to the design of a new approach for AuNP sensor development that overcame some of the limitations reported for previous AuNP sensors such as solubility, stability, selectivity and sensitivity. For environmental or biological applications, sensors must be utilized in water. Previous attempts to incorporate this attribute into AuNP sensor design have utilized biological molecules, such as DNA and peptides, to control particle aggregation[3,4,23,28] and provide low levels of analyte detection in aqueous environments. However, their use is limited due to requirements for stabilizing buffers to keep the particles dispersed in solution. Our approach complements those involving biomolecular ligands because the Bunte salt ligand derives its solubility from the functionality designed into the molecule. This method provides solubility in water and allows direct nanoparticle synthesis and stabilization to occur without the need for buffers or multiple ligand exchange processes, a requirement typical of particles functionalized with biological molecules.

We found that direct synthesis provides a facile route to achieving desired surface ligand composition. This process is an especially important consideration in the successful function of colorimetric AuNP sensors because the ligands dictate particle interaction upon analyte binding. A direct synthetic method for water-soluble, gallic acid functionalized AuNPs has been demonstrated to provide selective, colorimetric sensing for lead.[26] However, the nature of the chosen ligand used as the capping agent for the particle surface limits their use to a very narrow pH in which the nanoparticles are stable. The limited stability of this approach demonstrates that careful ligand choice is necessary for providing both stability *and* selectivity to the particle surface, ultimately leading to a better method for sensor development.

Finally, the design of our MHTMMA ligand provides, simultaneously, high selectivity and particle stability while facilitating controlled nanoparticle synthesis. These attributes remain key objectives in the development of sensors for use in a variety of applications since low selectivity in sensors increases the propensity for false positive results.[65,66] This new method, based on rational ligand design, will serve as a model to explore the possibilities of water-soluble colorimetric sensing across a broad spectrum of applications.

Bridge

Having demonstrated that selective, colorimetric sensing of lanthanide ions was possible through the use of a dual-functional precursor ligand, we wanted to explore the possibility of preparing a reversible colorimetric sensor for lanthanide ions. For

reversibility to be engineered into the function of the sensor, control over the ligand shell composition was necessary. Chapter IV describes our experiments to functionalize gold nanoparticles with a mixed ligand surface composition in a controllable manner. Rather than preparing the nanoparticles in batch, as in Chapter III, the mixed ligand nanoparticles were prepared using a microscale flow reactor. We demonstrate that use of the micro reactor provides control over the mixing and reagent delivery that is necessary to engineer reversibility into the function of a colorimetric gold nanoparticle-based sensor.

CHAPTER IV

SYNTHESIS OF A REVERSIBLE, COLORIMETRIC SENSOR FOR TRIVALENT EUROPIUM THROUGH USE OF A MICROSCALE FLOW SYSTEM

Note: Portions of Chapter IV are expected to appear in an upcoming publication, co-authored with J. E. Hutchison. The author designed the experiments and composed the manuscript corresponding to Chapter IV. The author performed most experiments, with the exception of assistance received in the set up of the flow system, which was performed by S. Lohse and P. Haben, and imaging of TEM samples, which was performed by S. Xie. J. E. Hutchison provided experimental and editorial guidance.

Introduction

In his classic talk 'There's plenty of room at the bottom', Richard Feynman spoke of the greater range of potential properties and applications accessible once the controlled arrangement of "things on a small scale" is achieved.[1] This is particularly true for nanoparticles because the spatial distribution and local chemical environment of nanoparticles dictate the observed optical, electronic, and chemical interactions, and therefore define the material properties of the system.[2,3] Analysis of the protecting

monolayer, or ligand shell, on nanoparticle surfaces allows scientists to understand the role that local environment[4,5] has on nanoparticle self-assembly,[6-8] ligand shell structure,[4,9,10] and changes in electronic behavior.[11] Manipulation of the molecular composition of the ligand shell environment allows nanoparticle functions including particle-particle interactions[9] and nanoscale assembly[6] to be explored for a range of applications including MRI contrasting agents,[12] energy storage,[13] conversion,[14] and sensing.[15]

Gold nanoparticles (AuNPs) are inorganic nanostructures that are interesting for sensing applications due to the unique optical properties that large (d_{core} > 3 nm) AuNPs exhibit when cross-linked by chemical analytes.[16] However, to take advantage of these optical properties the interparticle interactions must be controlled. To facilitate this type of control, AuNPs are often functionalized with molecular recognition sites.[17-20] We recently reported the direct synthesis of 2-(7-mercaptoheptyl)-N^1,N^1,N^3,N^3-tetramethylmalonamide (MHTMMA) functionalized gold nanoparticles for selective, colorimetric sensing of lanthanide ions (Ln^{3+}) in water.[21] The MHTMMA functionality has a 2:1 ligand-to-metal binding ratio that initiates nanoparticle cross-linking when the MHTMMA functionalized AuNPs are introduced to trivalent lanthanide solutions. The particle interaction can be detected by a colorimetric change in the nanoparticle solution from red to blue, a characteristic property of gold nanoparticle-based sensing systems.[16] Our MHTMMA AuNP sensor is both selective and sensitive, detecting europium and samarium at concentrations as low as 50 nM.

Although the cross-linking event is both selective and sensitive for lanthanide ions over potentially competing ion solutions, the resulting interaction was irreversible. The inability to reverse the binding interaction with EDTA, a chelator having a higher binding affinity for lanthanide ions, was thought to be due to the large networks of nanoparticles that form upon Ln^{3+} binding. Additionally, the aggregated networks lead to nanoparticle destabilization and precipitation. In order to overcome these limitations, and explore whether reversibility could be engineered into the function of our MHTMMA AuNP sensor, we sought a method to dilute the ligand shell in order to reduce cross-linking and irreversible aggregation.

Nanoparticles with mixed monolayers consisting of only a few MHTMMA ligands and a majority of a diluent molecule, such as 2-[2-(2-mercaptoethoxy)-ethoxy]ethanol (MEEE), would limit the extent of cross-linking while maintaining stability and solubility. MEEE does not bind to lanthanide ions, thus nanoparticles formed with a full MEEE ligand shell should show no response to the addition of a solution of Ln^{3+}. Similarly, if the synthesized nanoparticles are dominated by MHTMMA ligands, the colorimetric response and cross-linking event should mimic those of our previously reported system. A nanoparticle with a mixed MEEE/MHTMMA ligand shell should therefore limit the extent of cross-linking and allow EDTA to redisperse the nanoparticles (Figure 4.1). Furthermore, nanoparticles with varying amounts of MEEE and MHTMMA should respond differently to the addition of a solution containing Ln^{3+}, allowing the cross-linking event, colorimetric

response, and reversibility to serve as a semi-quantitative measurement for the relevant amount of MEEE and MHTMMA ligands on the surface of the prepared nanoparticles.

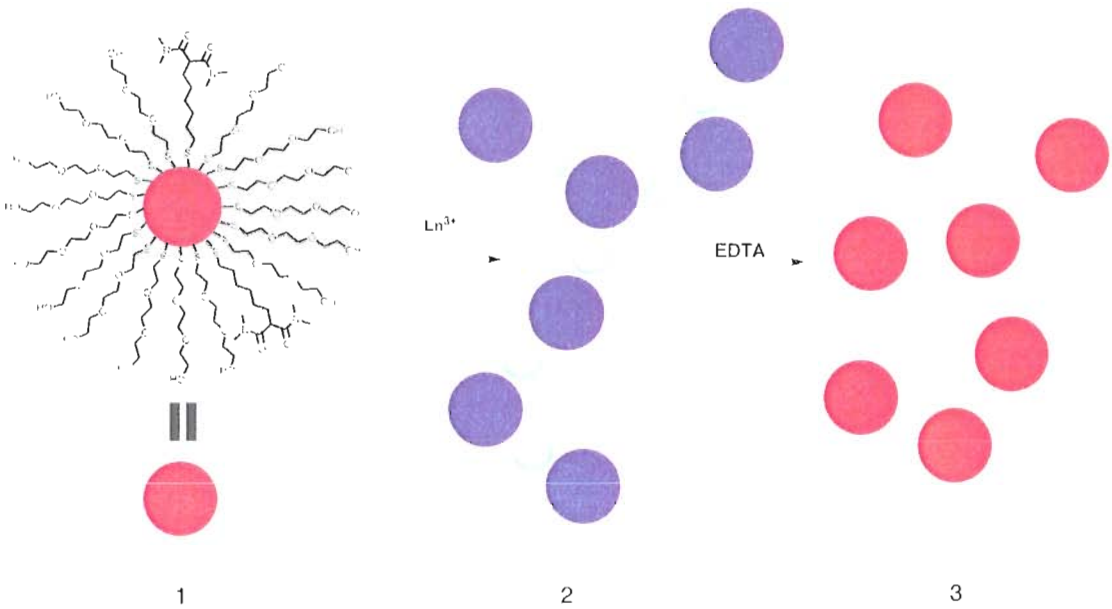

Figure 4.1: Schematic of a mixed monolayer nanoparticle system. Gold nanoparticles that incorporate a mixed ligand shell comprised of both MEEE and MHTMMA (1). When a lanthanide solution is introduced to the MEEE/MHTMMA functionalized particles, the MHTMMA ligand binds to the lanthanide, initiating nanoparticle cross-linking (2) and resulting in a color change from red to purple/blue. Since the number of MHTMMA ligands on the particle surface dictates the extent of particle cross-linking, a small number of MHTMMA ligands would allow the addition of EDTA to release the Ln^{3+} ion from the MHTMMA, and allow the nanoparticles to be dispersed back into solution (3), which would restore the initial color of the nanoparticle solution.

Samples of MEEE/MHTMMA AuNPs were prepared following the method used for our AuNP sensor containing full MHTMMA functionality, except that the amount of MHTMMA ligand was reduced and diluted with MEEE. Although some

trials exhibited reversibility, despite great care that was taken during NP synthesis, the results varied from batch to batch. The irreproducibility in the response appeared to trend with the size of the reaction vessel (e.g. 250-mL round bottomed flasks worked better than scintillation vials) that was used during synthesis. This led us to hypothesize that inadequate mixing of the reagents was leading to different compositions in our final NP product and hence varying colorimetric response and overall sensor performance. Thus, we sought methods for NP synthesis that would provide rapid mixing and more control over our reagent delivery. Microfluidic devices are one such method that have been shown to provide rapid mixing and controlled reagent delivery in order to synthesize nanoscale materials,[22-24]and were thus explored as our approach for producing MEEE/MHTMMA mixed ligand AuNPs.

The use of microfluidic devices offers rapid, facile control over reaction parameters that are not easily attained using traditional flask methods,[23,25] and have been reported to controllably synthesize nanoscale materials having inorganic/organic mixtures that include the synthesis of ligand-passivated nanoparticles.[22-24] Microfluidic reactors employ small volumes of solution through fabricated microchannels in order to control reaction conditions including time, temperature, mixing, and reagent delivery.[25,26] We have previously shown that use of a microscale flow system allowed the production of highly stable, atomically precise gold clusters,[27] producing gold nanoparticles with core diameters varying from less than 1- to greater than 5-nm. In this work, a microscale flow system was used to investigate whether microfluidics could

allow the synthesis of mixed monolayer nanoparticle designed for reversible, colorimetric detection of lanthanide ions in water.

Herein we report the synthesis and subsequent characterization of gold nanoparticles where the composition of the MEEE/MHTMMA ligand shell is systematically varied. Use of a microscale flow reactor provides precise control over reaction parameters, allowing the ligand concentration to be readily modified in order to tune the physical makeup of the final MEEE/MHTMMA AuNP product. The MEEE functionality stabilizes the nanoparticle and offers solubility in water, and the MHTMMA ligand provides lanthanide-binding functionality. Results show that the MEEE/MHTMMA gold nanoparticles bind europium in water, offering colorimetric lanthanide ion detection. This colorimetric response is reversible. The addition of EDTA releases the bound nanoparticles, an indication that the nanoparticle cross-linking event is controllable. The performance of the sensor is evaluated to correlate the efficacy of the microscale flow system as a method to introduce mixed monolayers on the surface of gold nanoparticles. MEEE/MHTMMA AuNPs prepared with less than 10% of MHTMMA ligand during NP synthesis results in reversible, colorimetric europium detection. However, when the concentration of MHTMMA ligand exceeds 10% of the total ligand solution used during synthesis, the colorimetric response is no longer reversible. Batch-based syntheses were explored to produce these same results, but did not give the required control of ligand composition that was necessary to control the cross-linking event.

Experimental Methods

Materials. All materials were obtained from their suppliers as given below and used as received: Hydrogen tetrachloroaurate hydrate (Strem), 2-[2-(2-chloroethoxy)-ethoxy]ethanol 99% (Aldrich), sodium hydroxide (Mallickandrot) and sodium borohydride (Aldrich, 98%). Deionized, Nanopure water (18.2 MΩ-cm) was purified with a Barnstead Nanopure Diamond system, and was used for the preparation of stock solutions and as a solvent for nanoparticle synthesis. Flow nanoparticle syntheses were driven using Kloehn syringe pumps (P/N 54022) and Kloehn 10 and 25 mL syringes. The flow system was created using IDEX Telfon tubing (0.75 mm ID, WO# 0554152) and Teflon tees. Lengths of tubing were used in assembling the reactor, to keep residence and mixing constant for all flow rates. Stock solutions of tris(hydroxymethyl)aminomethane (tris) buffer and ethylenediaminetetraacetic acid (EDTA) were prepared as 1 M and 0.5 M solutions, respectively, and diluted as needed with deionized water. All other reagents were obtained from Aldrich and used without further purification.

Synthetic procedures. *Synthesis of the Bunte salt analog of 2-[2-(2-mercaptoethoxy)-ethoxy]ethanol (MEEE).* The MEEE Bunte salt ligand precursor was prepared according to a reported procedure.[28] Briefly, 2-[2-(2-chloroethoxy)ethoxy]ethanol (5.8 g, 34.8 mmol) was combined in water with sodium thiosulfate (5.0 g, 31.6 mmol) and heated to reflux for three hours. The salts are filtered, and the water is removed by rotary evaporation. Trituration of the residual oil with ethanol affords the MEEE Bunte salt as a colorless oil.

Synthesis of the Bunte salt analog of 2-(7-mercaptoheptyl)-N^1,N^1,N^3,N^3-tetramethylmalonamide (MHTMMA). Synthesis of the MHTMMA ligand precursor followed previously reported procedures.[21] Briefly, sodium hydride (0.31 g, 12.9 mmol) was used to alkylate tetramethylmalonamide (1.92 g, 12.1 mmol) with 7-bromoheptan-1-ol (2.01 g, 10.3 mmol). The alcohol was then brominated with PBr_3 (0.19 mL, 2.0 mmol), and subsequently converted to the Bunte salt with sodium thiosulfate (1.04 g, 6.0 mmol) in a refluxing mixture of water and ethanol. The salts are filtered, and the solvent mixture is removed by rotary evaporation. Trituration of the residual oil with ethanol affords the MHTMMA Bunte salt as a colorless oil.

Batch-based synthesis of functionalized gold nanoparticles. An aqua regia (3:1 HCl:HNO_3) cleaned 250 mL round-bottom flask equipped with a stir bar was charged with 100 mL of H_2O, 1 mL of $HAuCl_4 \bullet xH_2O$ solution (0.1 M), and 500 uL of an aqueous MHTMMA or MEEE solution (0.1 M). The reaction mixture was allowed to stir for 10 minutes, and then 2.0 mL of a freshly prepared aqueous 0.1 M $NaBH_4$ solution was added. The reaction mixture was allowed to stir for 3 hours. The resulting nanoparticles are filtered through a coarse-fritted glass funnel, collected, and purified via diafiltration with twenty volume equivalents of Nanopure water through a 70 K membrane (Pall Corporation).[29]

Microscale flow system synthesis of functionalized gold nanoparticles. Individual stock solutions (10 mL) of aqueous hydrogen tetrachloroaurate (5.0 mM), Bunte salt ligand (MEEE, MHTMMA or a MEEE/MHTMMA mixture) (1.0 mM), and 20 mL of a solution of aqueous sodium borohydride (1.0 mM, adjusted to pH=10 with

NaOH), were prepared by serial dilution. The microscale system consists of two tees, automated syringe pumps, and Teflon tubing (Figure 4.2) that allows precise delivery of reagents and controls the reaction time. The pumps on the flow system are programmed to run at a flow rate of 3.0 mL/min. To begin the reaction, the syringe pumps aspirate 5.0 mL of the gold and ligand precursor solutions, as well as 10.0 mL of the borohydride solution. The syringes then dispense the gold and ligand solutions at a flow rate of 3.0 mL/min through 50 cm of tubing (retention time = 10 s), before joining the 3.0 mL/min stream of borohydride reagent in the second tee (Figure 4.2). Following the initiation of reduction by borohydride, the reaction solution flows through 329 cm of tubing (30 s residence time) in the reactor. The resulting dark red solutions of nanoparticles were collected in a flask at the end of the tubing, and filtered through a coarse-fritted glass funnel before purification via diafiltration with twenty volume equivalents of Nanopure water using a 50K membrane (Pall Corporation).[29]

Analytical procedures. Nanoparticles were characterized using a combination of transmission electron microscopy and UV-visible spectroscopy.

Transmission electron microscopy (TEM). TEM analysis was performed on a FEI Titan FEG-TEM equipped with an EDAX EDS detector. Gold nanoparticle samples were prepared for analysis by floating amine-functionalized Smart Grids™ (Dune Sciences) on top of a drop of solution (either MHTMMA, MEEE, or MEEE/MHTMMA AuNPs) for 1 minute followed by copious rinsing with Nanopure water. The grids were placed in a desiccator and allowed to dry overnight. After scanning the entire grid, five representative images were collected for each sample. A minimum of 600 nanoparticles

per sample was used for size analysis. The images were then processed using Image J software to determine average core diameter, size distribution and standard deviation following the reported method.[30]

To determine compositional make up of the nanoparticle networks, two TEM samples were prepared for EDX analysis. In the first, 1 mL of MEEE/MHTMMA AuNPs was added to 20 uL of an aqueous solution of 0.1 mM $Eu(NO_3)_3$. After one minute, the nanoparticles were centrifuged for 6 min at 6,000 rpm. The supernatant was discarded, and fresh water was added to the centrifuge tube. The process was repeated two more times to ensure removal of all europium not bound to the nanoparticle surface. The nanoparticles were deposited on the surface of the TEM grid using the above method. The second sample followed the same preparation except that one minute following the Eu^{3+} addition, an equal addition of EDTA was added to the nanoparticle solution.

UV-visible (UV-vis) spectroscopy. All measurements were performed using a Mikropack DH-2000 UV-vis-NIR light source equipped with an Ocean Optics USB2000 spectrophotometer. Absorbance of purified AuNPs was measured in a quartz cuvette that was cleaned with aqua regia and rinsed with copious amounts of Nanopure water in between all measurements. Absorbance spectra from nanoparticles that required dilution to prevent the absorbance from exceeding the saturation limit of the instrument were carried out using Nanopure water and were prepared to one-half the as-synthesized nanoparticle concentration (2:1 H_2O:NP).

Determination of detection limit. The detection limit of the nanoparticle sensors for europium was determined through a spectral titration of $Eu(NO_3)_3$ that was monitored via UV-vis spectroscopy.[21] The absorbance spectrum of 2 mL of purified 99.9:0.1 MEEE/MHTMMA AuNPs with 20 uL of 1 M Tris buffer was used as the blank. Successive aliquots of a 0.1 mM $Eu(NO_3)_{3\,(aq)}$ stock solution were added to the rapidly stirring nanoparticles, and the absorbance spectra recorded after each addition. A total of 12 aliquots of 0.1 mM $Eu(NO_3)_{3\,(aq)}$ were added during the titration (20 uL total, 10 successive 1 uL additions followed by two 5 uL additions), and the concentration of Eu^{3+}in the sample was calculated after each addition. Plotting the calculated Eu^{3+} concentration versus the absorbance at 570 nm determined the detection limit, which was defined as the minimum concentration of Eu^{3+} that caused an observable absorbance at 570 nm.

Investigation of reversibility. Reversibility of the prepared nanoparticle sensors was determined by monitoring the changes in absorbance as determined by UV-vis spectroscopy following subsequent additions of $Eu(NO_3)_{3\,(aq)}$ and $EDTA_{(aq)}$ stock solutions (1 mM). The initial absorbance of a rapidly stirring solution of 2 mL of 99.9:0.1 MEEE/MHTMMA and 20 uL of 1 M Tris buffer was measured. Further spectra were collected after 10-uL aliquots of Eu^{3+} solution were added to the nanoparticles. An equivalent aliquot of EDTA was then added to the solution, and the absorbance was again measured. The process was repeated using 20-uL, and 40-uL aliquots of the Eu^{3+} and EDTA stock solutions. The recorded absorbance at 540 nm was plotted versus the addition of Eu^{3+} or EDTA in order to determine the reversibility,

which was defined as the increase and subsequent decrease in absorbance at 540 nm following the addition of Eu^{3+} or EDTA, respectively.

Results and discussion

We wanted to control the extent of nanoparticle aggregation that occurs for our MHTMMA AuNP colorimetric lanthanide ion sensor,[21] to investigate whether the preparation of a reversible sensor was possible. To address this challenge, we incorporated a large amount of 'inert' MEEE ligand that provides the gold nanoparticle surface with solubility and stability with a small amount of 'active' MHTMMA ligand that drives nanoparticle cross-linking. The MEEE Bunte salt was chosen as the inert diluent ligand because MEEE has no affinity for lanthanide ions, but has demonstrated the ability to effectively passivate water-soluble gold nanoparticles[28] with core diameters greater than 3 nm. Synthesis of gold nanoparticles with core diameters greater than 3 nm is important parameter for this study because in this size regime, the surface plasmon absorbance at 520 nm becomes prominent, which enables colorimetric AuNP-based sensing.[31] Use of the MHTMMA Bunte salt ligand precursor has been shown to provide selective, colorimetric sensing of lanthanide ions in water.[21] We investigated whether sensor reversibility could be tuned by preparing gold nanoparticles comprised of a mixed ligand composition through combination of the MEEE and MHTMMA ligands. The main objective was to explore the hypothesis that a mixed-ligand composition, containing a few MHTMMA ligands on an otherwise MEEE

functionalized particle surface, could impart control over the nanoparticle cross-linking event and ultimately allow reversibility to be engineered into the function of the sensor.

Batch-based syntheses of MEEE/MHTMMA gold nanoparticles. Preparation of MEEE/MHTMMA mixed ligand nanoparticles through batch synthetic methods including direct synthesis and place exchange reactions were first investigated. [32,33] A total of 34 trials using various ratios of MEEE and MHTMMA were performed. The direct synthesis of MEEE/MHTMMA functionalized gold nanoparticles using mixtures of MEEE and MHTMMA ligand solutions resulted in the preparation of nanoparticle solutions that were stable and water-soluble. Of these experiments, 2 trials resulted in nanoparticles that showed spectral and colorimetric changes upon the addition of $Eu^{3+}$and EDTA. A total of 8 trials resulted in nanoparticles that responded to the addition of Eu^{3+}, but no changes were observed after EDTA addition. Nanoparticles that showed no spectral or colorimetric response after the addition of Eu^{3+} or EDTA dominated the experiments (24 of 35 total). The relative ligand composition was qualitatively determined using the spectral and colorimetric response of the nanoparticles after aqueous solutions of $Eu^{3+}$and EDTA were introduced to the particle solution. Nanoparticles functionalized primarily with MEEE displayed no changes; MHTMMA functionalized gold nanoparticles responded both visually and spectrally from the Eu^{3+} addition. Particles containing only a few MHTMMA ligands responded to both the Eu^{3+} and EDTA additions. The inconsistency of our results suggested that despite consistent synthetic procedures, the ligand shell composition varied greatly from batch to batch. Furthermore, efforts to functionalize gold nanoparticles with a small

number of MHTMMA ligands through introduction of low concentration MHTMMA solutions or through exposure of MHTMMA functionalized AuNPs to an excess of MEEE, led to nanoparticle solutions that aggregated upon exchange or during the purification process, preventing the nanoparticles to be captured for analysis. Both aggregation events suggest that the stability of the functionalized products were compromised during exchange. Although initial attempts to produce mixed ligand gold nanoparticles using these approaches were not reproducible, the two reaction trials that led to the synthesis of functionalized gold nanoparticles that showed reversible colorimetric response implied that fabrication of a reversible sensor *was* possible. However, the inconsistency in our results indicated that minor variations inherent in the batch conditions prevented control over the final ligand shell composition, proving to be detrimental to the reproducibility of our sensor. We thus sought an alternate method for nanoparticle production that would minimize variability during nanoparticle synthesis.

Microscale flow system for synthesis of MEEE/MHTMMA gold nanoparticles. Microscale reactors have been shown to impart precise control over synthetic parameters during nanoparticle synthesis.[22,23,27] Use of a microscale flow system was therefore investigated to control the delivery and mixing of reagents in order to reproducibly synthesize MEEE/MHTMMA mixed ligand nanoparticles. The system consisted of three automated syringes (one for each reagent), two tees, and a selection of Teflon tubing lengths (Figure 4.2). The mechanical syringe pumps eliminate small variations in reagent concentration and the tees provide enhanced reagent mixing. Both result in greater control over the nanoparticle products

synthesized from the microscale system. In this system the ligand and gold salt are introduced at the first tee, where the gold and ligand solutions react to form Au-ligand complexes. These complexes, or monomers, consist of precursor species that become the nanoparticle product upon addition of reductant.[34-37]

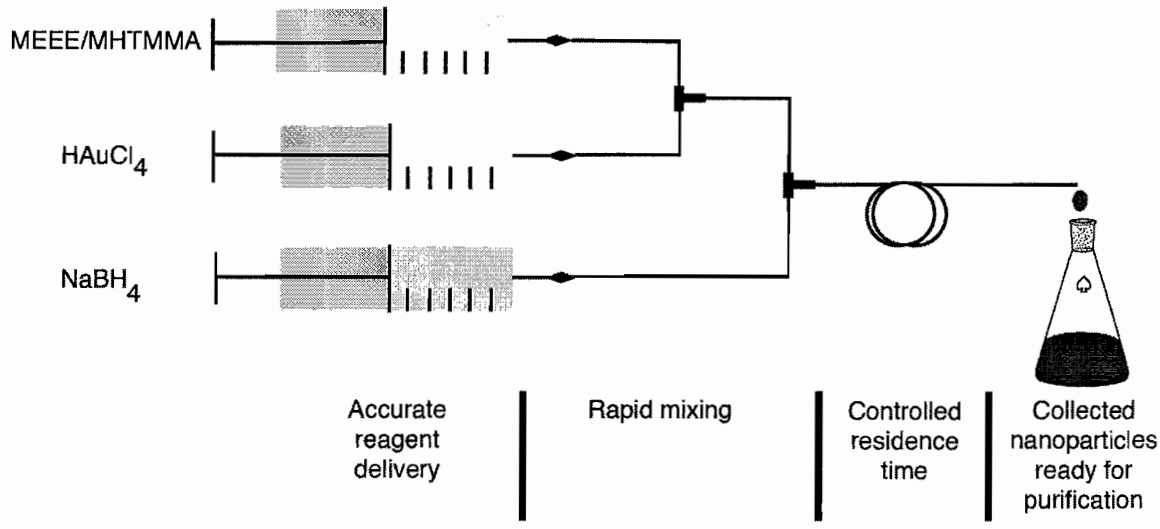

Figure 4.2: Schematic of a microscale flow system for mixed ligand AuNP production. Mechanical pump syringes provide accurate reagent delivery. Tees that connect the tubing on the syringe pumps provide rapid mixing of the reagents. The residence time for nanoparticle formation can be precisely controlled by the length and flow rate of the of the tubing. Nanoparticles are synthesized within minutes, and are ready for purification immediately following collection.

Following complex formation, the solution is carried to the second tee where introduction of a sodium borohydride solution occurs. Within two seconds of travel along the tube, the solution in the tubing shows an obvious color change after the addition of $NaBH_4$ that indicates nanoparticles are forming. The nanoparticle solution is collected at the end of the tubing and unreacted gold salt, unbound ligands, and other by-products are removed by diafiltration.[29]

Synthesis and evaluation of nanoparticles prepared with the microscale flow system. Two synthetic methods that produced the same nanoparticle product were investigated in order test the efficacy of our microscale system for nanoparticle production. Gold nanoparticles having a full MHTMMA ligand shell prepared using a batch synthesis resulted in particles with a prominent surface plasmon absorbance at 520 nm (Figure 4.3 A, red trace).

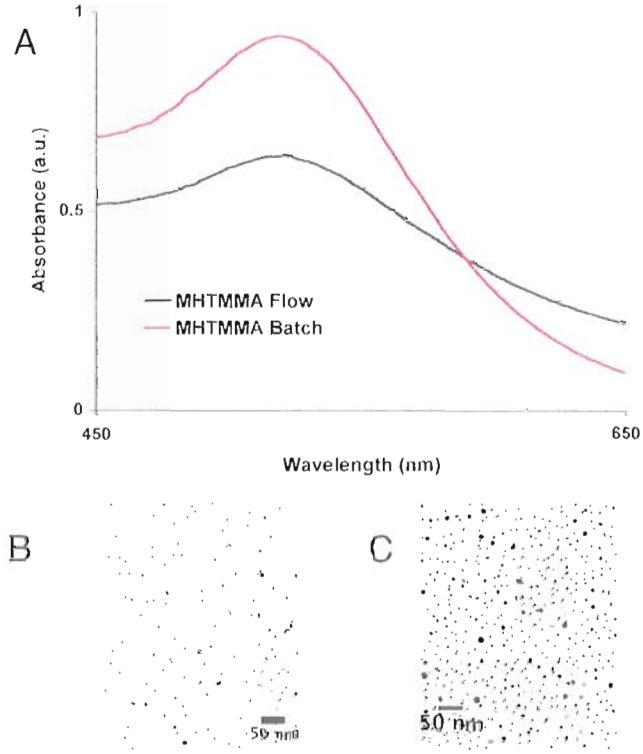

Figure 4.3: UV-vis spectra and TEM micrographs of MHTMMA AuNPs. The surface plasmon absorbance of the MHTMMA AuNPs prepared using the flow system (A, black trace) is not as distinct as the plasmon absorbance of the MHTMMA AuNPs prepared in batch (A, red trace) suggesting the AuNPs prepared in flow are not as large as those from the batch reaction. The micrographs show both methods for nanoparticle synthesis to provide dispersed solutions of nanoparticles. However, TEM analysis confirms the AuNPs prepared in flow (B) are approximately 2 nm smaller than those from the batch reaction (C), 4.5 nm versus 6.8 nm, respectively.

TEM confirmed these particles to be well dispersed, with a core diameter of 6.8 ± 2.7 nm (Figure 4.3, C). The analogous MHTMMA gold nanoparticles prepared using the microscale flow system also have a surface plasmon absorbance at 520 nm (Figure 4.3 A, black trace), but it is not as prominent as the particles prepared in batch. This suggested that the nanoparticles synthesized from the flow system were smaller than those prepared using the batch method. Size distribution analysis from the TEM images of the flow system MHTMMA AuNPs (Figure 4.3, B) confirm the product distribution is smaller, with a core diameter of 4.5 ± 1.7 nm. The nanoparticles synthesized from both synthetic methods, however, produced stable MHTMMA AuNPs that performed as colorimetric sensors for europium. This confirmed that use of the microscale flow system for nanoparticle production was possible with the MHTMMA ligand. In addition, these results also showed that nanoparticle size did not dictate reversibility, as addition of EDTA did not change the colorimetric or spectral response for either of the MHTMMA AuNPs prepared for this study.

Synthesis and characterization of a library of nanoparticles with varying ligand composition. Once the efficacy of nanoparticle production was confirmed with the microscale system, we investigated whether it could be used to prepare nanoparticles with varying ratios of MEEE and MHTMMA ligands (Chart 4.1). All of the nanoparticles that were synthesized for this study were water-soluble and stable. However, only some of the nanoparticles met the requirement for reversible detection of europium.

Chart 4.1: Nanoparticle mixtures prepared with the microscale flow system.

MEEE:MHTMMA ratio	Theoretical number of MHTMMA ligands on NP surface (d_{core}= 5 nm)	Colorimetric response to Eu^{3+}?	Reversible?
100:0	0	No	N/A
99.99:0.01	>1	No	N/A
99.9:0.1	>1	Yes	Yes
99:1	4	Yes	Yes
95:5	18	Yes	Yes
90:10	37	Yes	Yes
80:20	73	Yes	No
70:30	110	Yes	No
50:50	183	Yes	No
0:100	367	Yes	No

The theoretical number of total ligands available on the particle surface was approximated from the surface area of the particle and the footprint of the individual ligand.[38] This information was used to estimate the number of individual MHTMMA ligands on the particle surface after introduction of different MEEE/MHTMMA ligand ratios. A nanoparticle with a full MHTMMA ligand shell contains roughly 367 ligands on the particle surface. Although this provides for immediate and sensitive colorimetric detection of europium, the nanoparticle surface plasmon cannot be recovered even with the addition of a large excess of EDTA (Figure 4.4, A). Because the MEEE particles do not bind to lanthanide ions nanoparticle cross-linking does not occur, and no spectral

response is observed, after addition of Eu^{3+} to a solution of AuNPs functionalized with a full MEEE ligand shell (Figure 4.4, B).

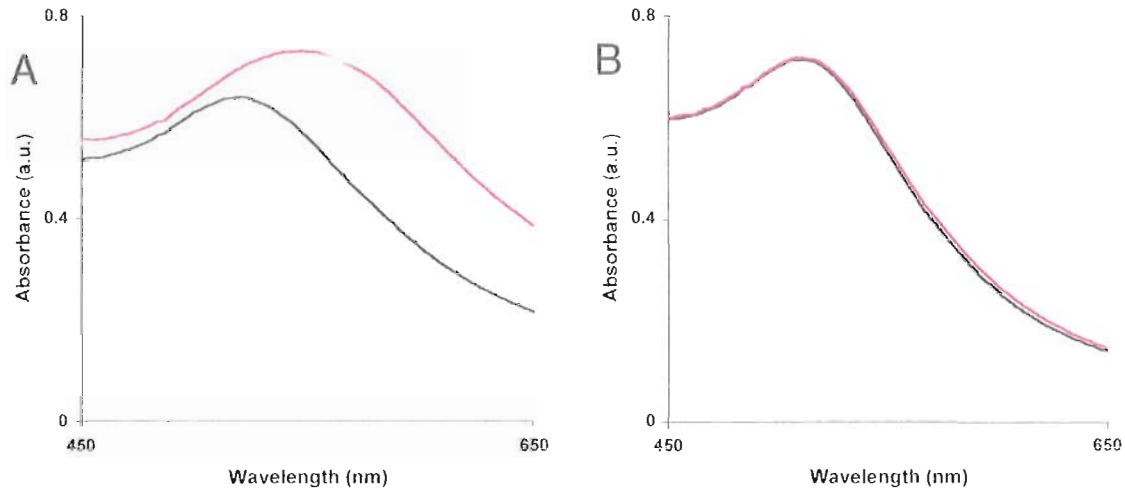

Figure 4.4: Spectral response of AuNPs passivated with a full ligand shell of either MHTMMA or MEEE. Gold nanoparticles with the MHTMMA ligand shell (A, black trace) show a distinct change upon the addition of Eu^{3+}(A, red trace). The shift and broadening of the surface plasmon is an indication of nanoparticle cross-linking. Upon addition of EDTA, the plasmon absorbance remains red-shifted (A, blue trace) indicating the nanoparticles remain bound to Eu^{3+}. Unlike the MHTMMA particles, AuNPs having a full MEEE ligand shell (B, black trace) show no spectral change upon addition of Eu^{3+}(B, red trace) indicating that the MEEE functionality does not bind to the Eu^{3+} ion, and no nanoparticle cross-linking occurs.

Finally, synthetic trials using MEEE/MHTMMA ratios to form nanoparticles with one MHTMMA ligand were performed to determine if nanoparticle dimer formation could be controlled. The 99.99:0.01 MEEE/MHTMMA AuNPs did not allow colorimetric sensing to occur, likely due to the ligand ratio being too dilute in MHTMMA to allow sufficient cross-linking to occur for spectral response. However, nanoparticles

synthesized with a 99.9:0.1 MEEE/MHTMMA ratio did show a colorimetric response to Eu^{3+}. Furthermore, all nanoparticle trials that contained 10% or less of the MHTMMA ligand during synthesis were reversible. The results of these studies confirm the successful synthesis of mixed ligand gold nanoparticles and also, to our knowledge, constitute the first report of a reversible, colorimetric AuNP-based sensor for europium.

Investigating MHTMMA concentration and nanoparticle cross-linking. The extent of nanoparticle cross-linking that occurs during Eu^{3+} addition was evaluated to assess the relationship between the concentration of MHTMMA precursor ligand used during nanoparticle synthesis and the extent of nanoparticle cross-linking after interaction with Eu^{3+}. TEM images of the resulting nanoparticle aggregates formed after introduction to a solution of Eu^{3+} (Figure 4.5) showed a direct relationship between MHTMMA concentration, nanoparticle cross-linking, and ultimately, the reversibility of the sensor. When a solution of gold nanoparticles with a full MHTMMA ligand shell was introduced to a Eu^{3+} solution, mass aggregation occurred during nanoparticle cross-linking. These large aggregates prevented EDTA from accessing the lanthanide ions bound to the malonamide functionality on the MHTMMA ligand. The binding affinity of malonamides for europium ions holds the nanoparticle networks together, thus the particles cannot be released from one another unless the ion is no longer chelated to the terminal malonamide group. Furthermore, when the large aggregates are unable to be re-dispersed back into solution, the particles eventually precipitate and are unable to be recaptured for further use. As the concentration of

MHTMMA ligand was decreased during nanoparticle synthesis, the resulting aggregates that formed upon addition of the Eu^{3+} solution also became reduced (Figure 4.5, A-C).

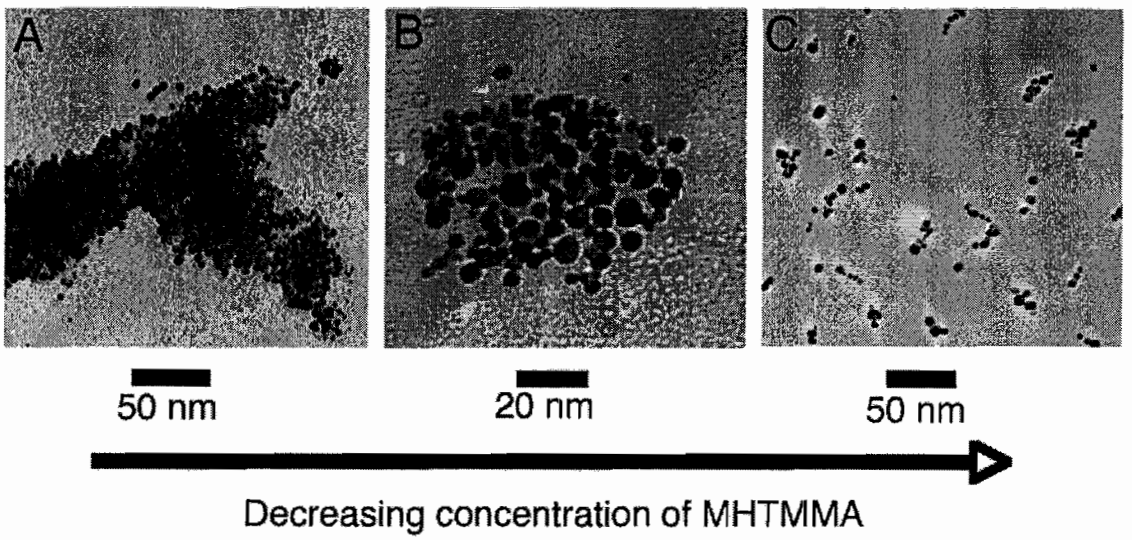

Figure 4.5: TEM micrographs of AuNP aggregates formed after introduction to a solution of Eu^{3+}. Nanoparticles that are passivated with a full MHTMMA ligand shell form large, extended networks of nanoparticle aggregates after introduction to Eu^{3+} (A). The mass aggregation prevents EDTA to access the bound europium, subsequently preventing the nanoparticle aggregates to be re-dispersed. As the number of MHTMMA ligands on the nanoparticle surface decreases, much smaller nanoparticle clusters form (B). This trend continues until only dimer, trimer and small chain clusters of nanoparticles can be seen (C). As the extent of nanoparticle aggregation declines, EDTA is able to release the Eu^{3+}-bound nanoparticles from the MHTMMA functionality, and provide the basis for sensor reversibility.

Nanoparticles that were synthesized with a MEEE/MHTMMA ratio consisting of 10% or less of the MHTMMA ligand showed reversibility, suggesting that the reduced number of MHTMMA ligands able to bind europium were the driving force behind the extent of nanoparticle aggregation. It is therefore necessary for nanoparticle networks small enough for EDTA to access the bound europium in order for the sensor to display

reversibility. The synthetic trial utilizing a 99.9:0.1 MEEE/MHTMMA ratio formed the smallest networks of nanoparticles upon addition of europium (Figure 4.5, C). This ratio of MEEE and MHTMMA should have a theoretical >1 MHTMMA on the surface. However, it is likely that the ligands on the particle surface were not evenly distributed, as the TEM images showed a mixture of single nanoparticles, as well as nanoparticle dimers, trimers, and small clusters (Figure 4.5, C). Further analysis of the ligand arrangement may be possible with use of a scanning tunneling microscope (STM), as information relating the spatial distribution of ligands on 2-D and 3-D gold surfaces have been reported.[10]

Investigating a reversible, colorimetric sensor for Eu^{3+}. Initial data from the nanoparticle library produced with the microscale system suggested that the nanoparticles prepared with a 99.9:0.1 MEEE/MHTMMA ratio formed the smallest networks of cross-linked particles, and met the requirement of reversible, colorimetric detection of europium. Nanoparticles prepared with this ligand ratio were thus chosen to further investigate whether Eu^{3+} is removed from the nanoparticle aggregates following addition of EDTA.

UV-vis spectra and TEM images were first obtained to confirm the performance of the 99.9:0.1 MEEE/MHTMMA AuNPs. The absorption spectra for these nanoparticles have a plasmon absorption centered at 520 nm that suggested the nanoparticles to be greater than 3 nm in size (Figure 4.6 A, black trace). Size distribution analysis[30] of the TEM images (Figure 4.6, B) show that the nanoparticles are 4.2 +/- 1.8 nm in diameter, are spherical in shape, and are well dispersed on the grid.

Absorbance spectra and TEM images showed obvious changes with the addition of $Eu(NO_3)_{3\,(aq)}$ and $EDTA_{(aq)}$ to the nanoparticle distribution. The addition of an aliquot of $Eu(NO_3)_{3\,(aq)}$ caused an immediate change in the color of the nanoparticle solution from red to blue. A broadening and bathochromic shift in the absorbance spectra accompanied the change in color (Figure 4.6 A, red trace). The changes in the absorbance spectra occurred as the nanoparticles were brought to within close proximity for nanoparticle cross-linking. The cross-linking event was driven by the malonamide functionality tethered to the nanoparticle surface by the MHTMMA ligand, and was confirmed by the presence of small nanoparticle clusters on the TEM grid surface (Figure 4.6, C). The addition of EDTA restored the plasmon absorbance back to 520 nm (Figure 4.6 A, blue trace), and changed the color of the nanoparticle solution back to red. Restoration of the initial absorbance spectra and nanoparticle color suggest that the nanoparticles were no longer cross-linked through the bound Eu^{3+} ion, and were freely dispersed back in solution. TEM images (Figure 4.6, D) reveal that no nanoparticle clusters remained on the grid and the particles were again well dispersed.

To confirm that europium had been removed from the dispersed nanoparticles, energy dispersive X-ray (EDX) spectra were obtained to analyze the composition of the nanoparticle networks following the addition of europium and EDTA. The EDX spectrum corresponding to a nanoparticle cluster after the addition of Eu^{3+} showed multiple peaks corresponding to europium (Figure 4.7, A), and confirmed the presence of this ion within the cross-linked structure. A second EDX spectrum was obtained for the dispersed nanoparticles following incubation with EDTA, and revealed that all of

the peaks corresponding to europium were no longer detectable (Figure 4.7. B). This suggests that europium was successfully removed from the bound nanoparticle networks. The combined UV-vis. TEM and EDX data provide conclusive evidence that upon addition of EDTA europium is removed from the MEEE/MHTMMA mixed ligand AuNPs. and which permits reversible. colorimetric detection of europium.

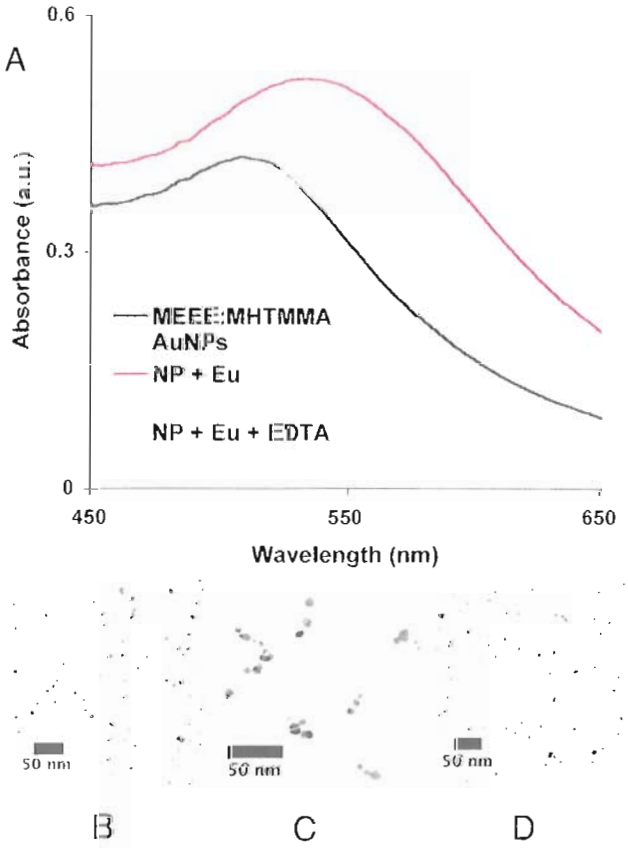

Figure 4.6: Absorbance spectra and TEM micrographs of MEEE/MHTMMA AuNPs. UV-vis spectra of 99.9:0.1 MEEE/MHTMMA AuNPs after purification (A, black trace) show a distinct absorption at 520 nm. Following the addition of europium (A, red trace). the absorption is red-shifted. The addition of EDTA (A, blue trace) restores the initial absorption at 520 nm. TEM micrographs show the nanoparticles to be well dispersed and spherical in shape (B). After addition of europium, small clusters of nanoparticles can be seen (C). Addition of EDTA removes the europium from the malonamide functionality, which enables the nanoparticles to be re-dispersed (D), and restores the initial plasmon absorbance at 520 nm (A, blue trace).

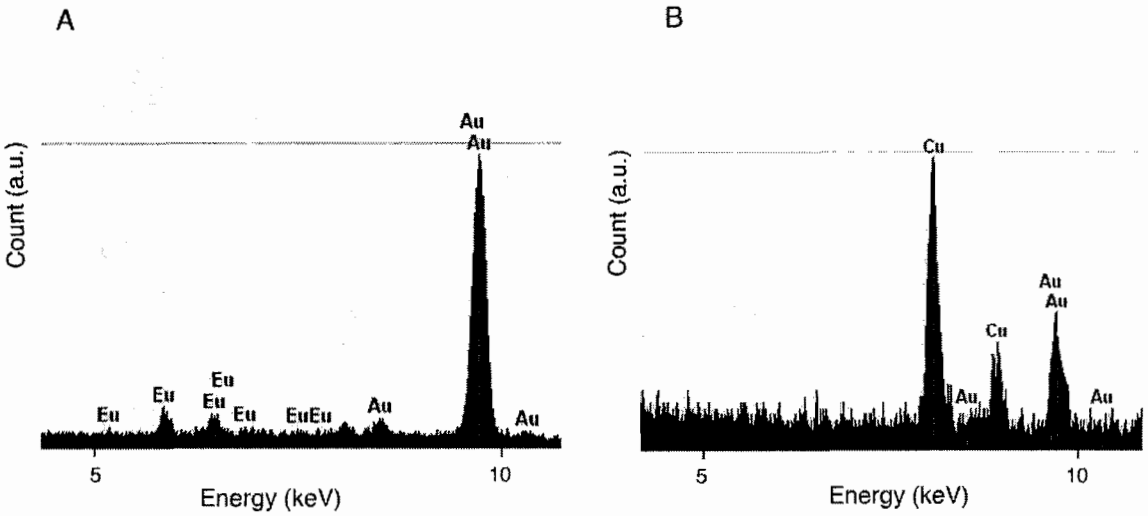

Figure 4.7: EDX spectra of MEEE/MHTMMA AuNPs after introduction to solutions of Eu^{3+} and EDTA. Europium can be detected within the nanoparticle cluster after introduction to europium (A). Following addition of EDTA, the same nanoparticle sample shows no europium on the particle surface (B). This indicates that the EDTA can successfully remove all measurable amounts of europium from the nanoparticle sample.

Determination of detection limit for Eu^{3+} binding. The dynamic range of the MEEE/MHTMMA AuNP sensor is defined as the upper and lower limits that display a change in the UV-vis absorbance spectra upon addition of a solution of Eu^{3+}. The lower limit of the dynamic range corresponds to the detection limit of the sensor. Titration of a 0.1 mM $Eu(NO_3)_3$ solution into the 99.9:0.1 MEEE/MHTMMA functionalized gold nanoparticles allowed the quantitative determination of the detection limit for this system (Figure 4.8). The change in the absorbance spectra at 570 nm was monitored as the concentration of Eu^{3+} was increased. An increase in this region of the spectra corresponds to nanoparticle cross coupling, induced by Eu^{3+}-particle binding. The second 1 uL addition of 0.1 mM Eu^{3+} resulted in a measurable increase in the in the

absorbance at 570 nm. The absorbance continued to increase as the concentration of Eu^{3+} increased, until the upper limit of the dynamic range was reached. Beyond this point the absorbance did not change and presumably, all of the Eu^{3+} binding ligands were occupied. The titration data show the upper and lower limits of the dynamic range for this system to be 500 nM and 100 nM, respectively (Figure 4.8, B). The 100 nM detection limit of the MEEE/MHTMMA mixed ligand sensor is two times higher than that of the full MHTMMA AuNP sensor.[21] Because the mixed ligand system has fewer TMMA functionalities to cross-link particles, more Eu^{3+} might be needed to initiate substantial particle interaction for the detector to measure. In addition, the smaller aggregate size may impact the lower measurable limit of the sensor, as the shift of the surface plasmon absorption that occurs when particles interact is directly related to the extent of interaction.[16] The titration data for the full MHTMMA AuNP system used 620 nm as the wavelength corresponding to interacting particles. The nanoparticle solution prior to europium addition has a very small absorbance in this region. Thus, when the nanoparticle solution was blanked, there was little overlap between the regions of the absorbance spectra corresponding to dispersed and coupled particles. On the contrary, the mixed ligand system has a much higher relative absorbance at the wavelength (570 nm) corresponding to nanoparticle cross-linking.

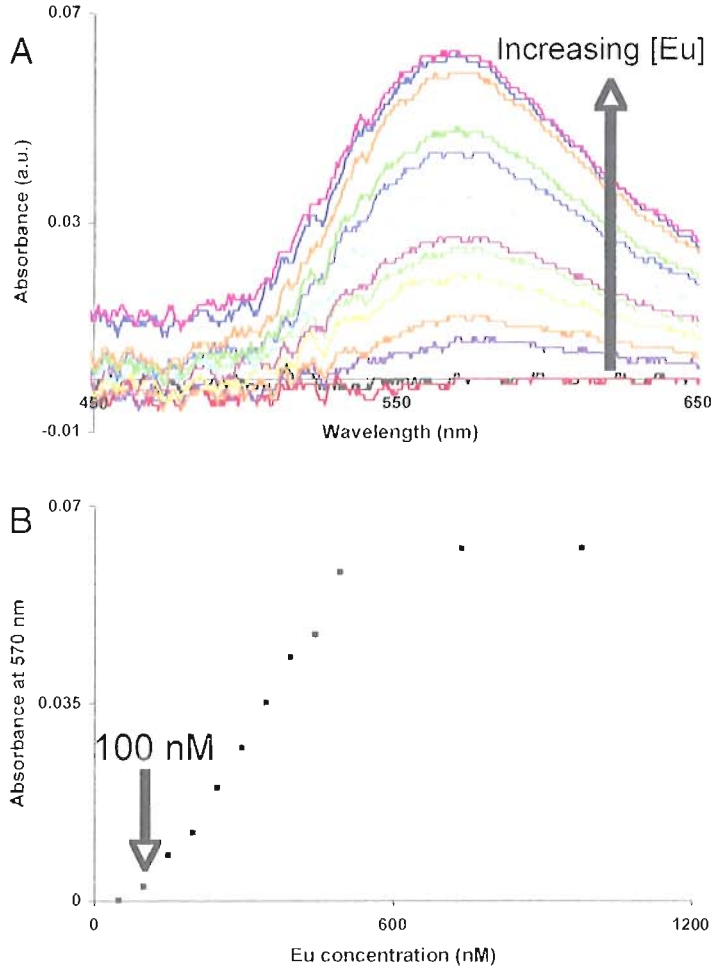

Figure 4.8: Spectral titration and resulting A vs. Eu concentration data that define the dynamic range of the mixed ligand AuNP sensor to Eu^{3+}. A UV-vis titration (A) was performed to determine the absorbance change as subsequent aliquots of Eu^{3+} were added to the MEEE/MHTMMA AuNPs. An initial spectrum of the MEEE/MHTMMA AuNPs was recorded and this solution was used as the blank. Upon addition of the Eu^{3+} solution, one can monitor the increase in the longer wavelength absorbance resulting from the interaction of surface plasmons of the particles. From the titration data, the absorbance at a single wavelength (570 nm) can be plotted as a function of concentration for the added Eu^{3+} metal ion (B) to determine the dynamic range of the sensor. The low limit of the sensor correlates to the detection limit of the system, and was determined to be 100 nM. In this sample the upper limit was 500 nM, though the upper limit can be tuned as a function of nanoparticle concentration, as the upper limit decreases as the concentration of nanoparticles increases.

However, regardless of whether the increase in detection limit was due to spectra subtraction during the titration, or the overall lower number of malonamide groups on the particle surface, the 100 nM detection limit is well within the same order of magnitude as our previously reported lanthanide sensor that contains the lowest reported detection limit for AuNP-based colorimetric detection of this ion.[21]

Determination of MEEE/MHTMMA AuNP reversibility. Reversibility is defined for our system as the ability to control particle-particle interactions of MEEE/MHTMMA functionalized gold nanoparticles. Particle interaction was initiated by introduction of a Eu^{3+} solution. EDTA was used to unlock the nanoparticle networks by releasing the bound europium ion, allowing the nanoparticles to become re-dispersed into solution. Subsequent addition of europium resulted in nanoparticle cross-linking once again. Control over the cross-linking event must occur without interruption to the stability of the particle solution. Nanoparticle stability was an important factor because precipitation would imply that the nanoparticle binding event was perturbed but not manipulated. The absorbance spectra and color of the nanoparticle solution were monitored during additions of Eu^{3+} and EDTA to the 99.9:0.1 MEEE/MHTMMA functionalized AuNPs (Figure 4.9). The absorbance at 540 nm increased and subsequently decreased as equivalent aliquots of Eu^{3+} and EDTA solutions were added to the NP solution (Figure 4.9, A).

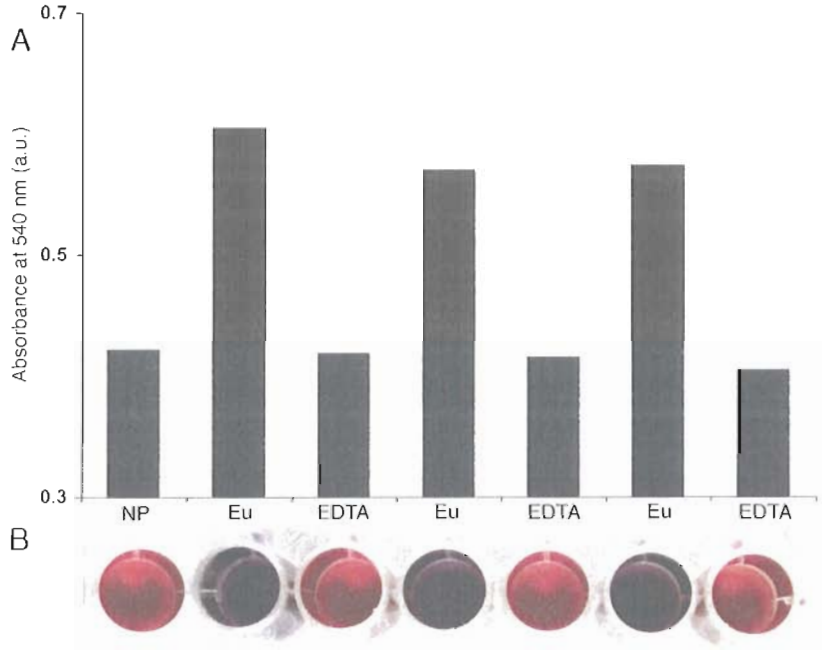

Figure 4.9: Absorbance data and images confirming sensor reversibility. Control over the composition of the ligand shell allows reversibility to be engineered into the function of the sensor. The nanoparticles can cross-link and be subsequently released after multiple additions of europium and EDTA, respectively. Reversibility is monitored by the increase and decrease in absorbance at 540 nm after europium and EDTA additions (A), respectively. The color of the nanoparticle solution toggles back and forth as the nanoparticles become cross-linked and re-dispersed (B), suggesting that the EDTA is successfully removing the lanthanide ion from the nanoparticle surface, allowing the malonamide functionality on the nanoparticle surface to become available for binding to additional europium ions added to the nanoparticle solution.

No scattering was detected in the UV-vis absorbance spectra suggesting that the nanoparticles remained dispersed and well solvated. Furthermore, the final nanoparticle solution following the third EDTA addition showed no sign of aggregation or precipitation. In addition to changes in the absorbance spectra, the color of the nanoparticle solution was monitored by visual changes that occurred during each addition. The nanoparticle solution toggled between blue and red after addition of

europium and EDTA, respectively (Figure 4.9, B). The ability to restore both the absorbance and color of the initial nanoparticle solution after repeated additions of Eu^{3+} and EDTA confirmed the reversibility of this system. Reversibility can be advantageous for applications requiring multiple test iterations. The results of this study show that it is possible to control the nanoparticle cross-linking event through ligand-ion interactions that occur at a gold nanoparticle surface.

Conclusions

In summary, gold nanoparticles comprised of a mixed MEEE/MHTMMA ligand shell have enabled reversible, colorimetric sensing of europium to occur. The MHTMMA-Eu^{3+} binding event drove particle interaction and the MEEE ligand controlled the extent of nanoparticle cross-linking by diluting the particle surface with inert, non-Eu^{3+} binding functionality. The detection limit was found to be 100 nM for the MEEE/MHTMMA AuNP sensor. Use of a microscale flow reactor over traditional batch syntheses provided the necessary control over reaction conditions, namely the accurate delivery and thorough mixing of reagents, to prepare these mixed ligand nanoparticles. The ligand shell composition varied according to the ratio of MEEE and MHTMMA ligand precursor solution used during synthesis and was used to tune the extent of nanoparticle cross-linking, which allowed reversibility to be engineered into the function of the sensor. Use of the microscale flow system has shown that the surface ligand chemistry can be controlled. This type of control may prove useful for future studies to allow the spatial assembly of nanoparticles, including the assembly of higher

ordered nanoparticle architectures, to occur and provide access to applications not currently available using traditional, batch techniques.

Bridge

During the trials to prepare MEEE/MHTMMA mixed ligand gold nanoparticles using batch synthetic methods, we noticed that several of the control experiments involving the synthesis of MEEE functionalized AuNPs resulted in nanoparticle solutions that were not stable to the addition of Eu^{3+}. These nanoparticle solutions formed mass agglomerates that immediately precipitated upon the addition of europium, and were not consistent with previous MEEE functionalized AuNPs that showed no response to excess amounts of this lanthanide ion. Agglomeration occurred with the addition of any solution that changed the ionic concentration of the prepared nanoparticles. In addition, the nanoparticles would precipitate from solution over the course of several days without any perturbation to the ionic concentration of the nanoparticle solution. Despite keeping the synthetic conditions constant, the MEEE AuNP products varied greatly. The reaction trials either produced stable nanoparticles that showed no response to changes in ionicity or resulted in solutions of unstable nanoparticles that precipitated from solution. The lack of reproducibility led to the investigation of the nature of the observed instability. Chapter V consists of experiments that were carried out by Sam Lohse and myself to understand the role that synthetic batch conditions have on the stability of MEEE gold nanoparticles prepared from the MEEE Bunte salt ligand precursor.

CHAPTER V

INVESTIGATING THE ROLE OF REDUCING AGENT ON THE STABILITY OF GOLD NANOPARTICLES PRODUCED FROM BUNTE SALT LIGAND PRECURSORS

Note: Experimental design and data acquisition corresponding to Chapter V were executed in equal parts by the author and S. Lohse. S. Golledge performed acquisition and peak fitting of XPS data. J. E. Hutchison provided experimental and editorial guidance.

Introduction

The high surface area, reactivity, and unique, size-dependant properties of inorganic nanoparticles (NPs) has prompted numerous developments for functional hybrid nanomaterials in sensing[1-3], bio-molecular tagging,[4-6] microelectronic,[7,8] and optical device application.[9-11] A well-defined molecular coating, or ligand shell, on the nanoparticle surface is crucial for proper performance. The ligand shell helps to prevent irreversible fusion, or aggregation, of the nanoparticle cores, controls interparticle interactions, and enhances nanoparticle solubility.[12-15] These attributes determine the

nanoparticles stability, and capability for additional functions that include ligand exchange[16] subsequent synthetic modification,[17,18]functionalization to solid supports,[19,20] and molecular recognition to chemical analytes.[21-24] However, surface ligands that are not securely anchored to the particle core can become dissociated from the surface, which causes the particles to aggregate.[25-28] This can negatively impact particle solubility and stability, two key requirements for performance. For these reasons, a well-defined ligand shell is vital for proper functional nanomaterial design.

Ligand shells can be comprised of a complex multilayered assembly of organic molecules held to the particle surface by electrostatic interaction, such as that of citrate-stabilized nanoparticles.[12,29] Alternately, nanoparticles can also be stabilized by ligands that form a covalent interaction between a terminal ligand functionality and the particle core. Thiols are one terminal ligand functionality that are often used to provide a stable surface coating for gold nanoparticles (AuNPs), due to the strong covalent bond that forms between sulfur and gold.[16,27,29,30] This strong interaction has prompted the development of a vast library of thiol ligands designed to provide passivation of the gold nanoparticle core while also allowing ω-functionalities to be displayed on the particle surface. In addition, thiol ligands can permit direct AuNP synthesis, but the range of nanoparticle core sizes available using thiol ligands is limited to core diameters less than 4.0 nm.[9,31,32] Direct methods to produce functionalized AuNPs having a variety of sizes thus require the use of alternate ligand functionalities.

Protected, or masked, thiols are a group of ligands that form ω-functionalized thiolate monolayers on both 2-D gold surfaces and gold nanoparticles. This class of

ligand precursor includes sodium thiosulfates, or Bunte salts, ($R\text{-}S_2O_3Na$),[33-35] disulfides (R-SS-R),[36] and thiocyanantes, (R-SCN).[37,38]and have allowed the preparation of thiol-protected gold nanoparticles to be synthesized in a single, direct step, while providing access to particle sizes that are unavailable in direct syntheses with unmasked thiol ligands.[39] In particular, Bunte salts have been used to access thiol-protected gold nanoparticles with core diameters ranging from 1.5 to 20 nm in diameter,[40] as well as functionalized AuNPs designed for functional application.[21] In these cases, the larger particle sizes were thought to result from the slower passivation kinetics of monolayer formation from the terminal Bunte salt functionality. Despite the differences in their chemical and electronic behavior,[41,42] the mechanism of Bunte salts monolayer formation on gold nanoparticle surfaces is understood primarily by analogy to thiolate monolayer formation studies on 2-D gold substrates,[33,37,38,43] where the formation of the thiolate-Au bond is thought to occur via adsorption of the protected thiol followed by catalytic sulfur-sulfur bond breakage at the gold surface.[33]

Surface characterization of gold nanoparticles produced using masked thiol ligands suggests that the final nanoparticle product is stabilized with a protective Au-thiol monolayer,[12-14,29]analogous to AuNPs produced using traditional, unprotected thiol ligands,[35,40] and should therefore have the same chemical behavior and stability against aggregation and precipitation. However, in the course of synthesizing gold nanoparticles from the Bunte salt analog of 2-[2-(2-mercaptoethoxy)-ethoxy]ethanol (MEEE), we found that our final nanoparticle products were inconsistently stable. The MEEE nanoparticles would precipitate when the environment of the nanoparticle

solution was perturbed. Such perturbations included extensive purification by diafiltration,[44] changes in the nanoparticle concentration from centrifugation, and changes to the solution pH, as well as ionic strength. In addition, MEEE AuNPs produced in 250-mL round bottomed flasks were often stable, producing nanoparticles that remained dispersed in solution indefinitely, regardless to purification, changes in pH, ionicity, or concentration. Conversely, all synthetic trials to produce MEEE AuNPs 20-mL scintillation vials resulted in unstable nanoparticles that could not be purified, and eventually precipitated over the course of a few hours to a couple of days. The precipitation event could be expedited when the volume of the nanoparticle solution was reduced, or the ionic strength was altered by addition of a metal ion solution. Although the precipitation event was not desirable, addition of $Eu(NO_3)_3$ or $Gd(NO_3)_3$ could be used as a rapid assay to monitor the stability of our prepared AuNPs. These results were in direct contrast to AuNPs produced from the traditional MEEE thiol ligand, which are reproducibly synthesized, purified, and stable to wide variations in pH and ionic strength.[16,44]

The observed inconsistencies in our nanoparticle products led us to hypothesize that instability may be the result of insufficient reduction of the Bunte salt, which would prevent the formation of the Au-thiolate linkage on the nanoparticle surface. An investigation of thiolate formation on the surface of gold nanoparticles from Bunte salt precursor ligands should provide insight into the mechanism of ligand transformation during nanoparticle synthesis, and lead to an improved synthetic method for gold nanoparticle formation from Bunte salt ligand precursors. To investigate our

hypothesis, the reaction variables present during ligand shell formation were systematically evaluated, including reaction vessel size, heat, mixing time allowed for reaction between the ligand and gold precursors, and concentration of the reducing agent.

Herein we report the investigation of the thiolate monolayer formation on AuNP surfaces during direct nanoparticle synthesis from the Bunte salt analog of 2-[2-(2-mercaptoethoxy)-ethoxy]ethanol (MEEE). XPS analysis confirmed that the surface of unstable MEEE AuNPs were dominated by oxidized sulfur species, present from the incomplete reduction of the Bunte salt precursor. Conversely, stable MEEE AuNPs were passivated with a ligand shell that was predominantly composed of a thiolate monolayer. The concentration of sodium borohydride used during synthesis impacted the composition of the monolayer on the AuNP surface (Figure 5.1). The results of this study confirm that the reducing agent plays a role in the ligand transformation from thiosulfate to thiolate functionality, which impacts the formation of the thiolate monolayer, a mechanism that was previously attributed to the catalytic reduction of the sulfur-sulfur bond at the gold nanoparticle surface.[33,35] The formation of a complete thiolate monolayer was found to have a direct relationship to the stability of the nanoparticle solution. All of the nanoparticle samples that were passivated with a MEEE ligand shell bound to the gold core by thiolate linkage remained in solution after extensive purification, and were resistant to changes in pH and ionic strength. The nanoparticles passivated with oxidized species were unstable under analogous conditions.

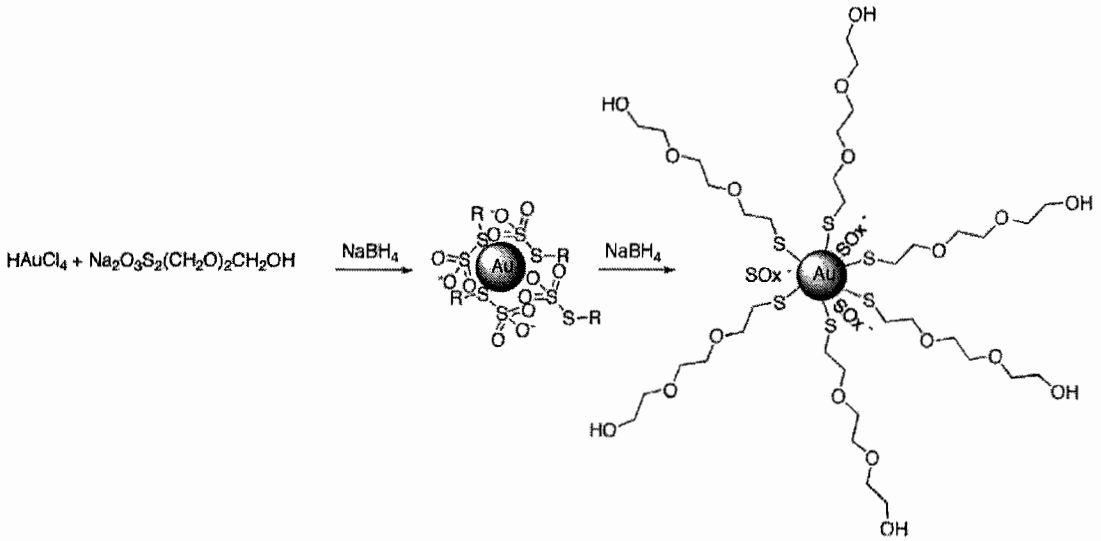

Figure 5.1: Schematic of AuNP formation from Bunte salt ligand precursors. An initial addition of sodium borohydride to an aqueous solution of gold tetrachloroaurate and MEEE Bunte salt ligand forms nanoparticles stabilized with a shell of oxidized sulfur species. A subsequent addition of borohydride results in the conversion of oxidized sulfur to thiolate linkage, producing stable solutions of MEEE functionalized gold nanoparticles.

Experimental methods

Materials. Hydrogen tetrachloroaurate was obtained from Alfa Aesar. All other reagents were obtained from Aldrich and used without further purification. Deionized, Nanopure water (18.2 MΩ-cm) was purified with a Barnstead Nanopure Diamond system, and was used for the preparation of stock solutions and as a solvent for nanoparticle synthesis.

Synthetic procedures. *Synthesis of the Bunte salt analog of 2-[2-(2-mercaptoethoxy)-ethoxy]ethanol (MEEE).* The MEEE Bunte salt ligand precursor was prepared according to a reported procedure.[39] Briefly, 2-[2-(2-

chloroethoxy)ethoxy]ethanol (5.8 g, 34.8 mmol) was combined in water with sodium thiosulfate (5.0 g, 31.6 mmol) and heated to reflux for three hours.

Flask-based synthesis of functionalized gold nanoparticles. An aqua regia (3:1 $HCl:HNO_3$) cleaned 250-mL round bottom flask equipped with a stir bar was charged with 100 mL of H_2O, 1 mL of $HAuCl_4 \bullet xH_2O$ solution (0.1 M), and 500 uL of an aqueous MEEE solution (0.1 M). The reaction mixture was allowed to stir for 10 minutes, and then 2.0 mL of a freshly prepared aqueous 0.1 M $NaBH_4$ solution was added. The reaction mixture was allowed to stir for 3 hours. The resulting nanoparticles are filtered through a coarse-fritted glass funnel, collected and purified via diafiltration with twenty volume equivalents of Nanopure water through a 70 K membrane (Pall Corporation).[44]

Vial-based synthesis of functionalized gold nanoparticles. An aqua regia (3:1 $HCl:HNO_3$) cleaned 20-mL scintillation vial equipped with a stir bar was charged with 10 mL of H_2O, 0.1 mL of $HAuCl_4 \bullet xH_2O$ solution (0.1 M), and 50 uL of an aqueous MHTMMA or MEEE solution (0.1 M). The reaction mixture was allowed to stir for 10 minutes, and then 0.2 mL of a freshly prepared aqueous 0.1 M $NaBH_4$ solution was added. The reaction mixture was allowed to stir for 3 hours. The resulting nanoparticles are filtered through a coarse-fritted glass funnel, collected, and purified via diafiltration with twenty volume equivalents of Nanopure water through a 70 K membrane (Pall Corporation).[44]

Determining the effect of reducing agent concentration on particle stability. AuNPs were synthesized using the standard flask synthesis method described above.

Following diafiltration, the AuNP solution was divided into thirds, and placed in three separate 100-mL round bottom flasks. 5.0 mL of Nanopure water was added to the first flask. 3 mL of aqueous $NaBH_4$ (0.1 M) and 2 mL of Nanopure water were added to the second flask. This solution remained a vibrant red color. To the final flask, 3.0 mL of aqueous $NaBH_4$ (0.1 M) and 2 mL of MEEE (0.01 M) were added. This solution remained a vibrant red color. Samples of all solutions were retained for UV-vis and TEM analysis.

Analytical procedures. Nanoparticles were characterized using a combination of transmission electron microscopy, UV-visible spectroscopy, and X-ray photoelectron spectroscopy.

Transmission electron microscopy (TEM). TEM analysis was performed on a FEI Titan FEG-TEM. Gold nanoparticle samples were prepared for analysis by floating amine-functionalized Smart Grids™ (Dune Sciences) on top of a drop of MEEE AuNP solution for 1 minute followed by copious rinsing with Nanopure water. The grids were placed in a desiccator and allowed to dry overnight. After scanning the entire grid, five representative images were collected for each sample. A minimum of 600 nanoparticles per sample was used for size analysis. The images were then processed using Image J software to determine average core diameter, size distribution and standard deviation following the reported method.[45]

UV-visible (UV-vis) spectroscopy. All measurements were performed using a Mikropack DH-2000 UV-vis-NIR light source equipped with an Ocean Optics USB2000 spectrophotometer. Absorbance of purified AuNPs was measured in a quartz

cuvette that was cleaned with aqua regia and rinsed with copious amounts of Nanopure water in between all measurements. Absorbance spectra from nanoparticles that required dilution to prevent the absorbance from exceeding the saturation limit of the instrument were carried out using Nanopure water.

Determination of stability. Stability measurements of the AuNPs formed from the Bunte salt ligand precursor of MEEE were carried out through the addition (100-uL) of an aqueous solution of either 0.1 M $Gd(NO_3)_3$ or $Eu(NO_3)_3$ to 1-mL of NPs.

X-ray photoelectron spectroscopy (XPS). XPS analysis was performed on a ThermoScientific ESCALAB 250 XPS. NP samples prepared for XPS analysis were first centrifuged for 6 min at 6,000 rpm to concentrate the NP solution. A 20-uL droplet of concentrated MEEE AuNPs were then placed on the surface of a 1 x1 mm segment of silicon wafer that was covered by an approximately 500 angstrom layer of evaporated chromium. This process was repeated 5 times, or until the deposited NPs formed a non-transparent sample layer on the wafer surface.

Results and discussion

The formation of a robust ligand shell can impact nanoparticle solubility, as well as provide the ability to withstand changes to the local chemical environment that can lead to irreversible nanoparticle aggregation.[12-14,29] Bunte salt ligand precursors produce colloidal solutions of functionalized nanoparticles, where the ligand is held to the nanoparticle surface through thiolate linkage.[35] The synthesis of gold nanoparticles from Bunte salt ligand precursors has allowed the direct synthesis of AuNPs with

various core sizes and surface functionality.[21,35,40] In the course of our previous investigation of gold nanoparticles functionalized with Bunte salt ligands designed for colorimetric Ln^{3+} detection, we explored the synthesis of AuNPs from Bunte salt ligands having various terminal functionality.[21] However, it was found that the synthesis of AuNPs from Bunte salt ligand precursors did not consistently result in a final product that remained well dispersed in solution after perturbation of the nanoparticle solution.

AuNPs synthesized from a MEEE Bunte salt precursor ligand resulted in the formation of nanoparticles that were not reliably stable to purification by diafiltration,[44] or concentration by centrifugation. In addition, the synthesis of MEEE AuNPs produced particles that were inconsistently stable to changes in ionic strength, or the size of reaction flask used during synthesis. This type of sensitivity to changes in the local chemical environment is characteristic of ionically stabilized nanoparticles, such as particles that have a citrate-passivated shell.[29,42] To understand the origin of the instability displayed between various trials of synthesized MEEE AuNPs, comparisons between stable and unstable samples were performed.

Comparing stable and unstable MEEE AuNPs. Despite analogous reaction conditions, the synthesis of MEEE AuNPs resulted in products that were inconsistently resistant to the addition of an aqueous $Gd(NO_3)_3$ metal ion solution, resulting in particles that sometimes aggregated upon ion addition. The sensitivity to the Gd^{3+} metal was used as a rapid method to assay the stability of the nanoparticle solution. The spectral response of stable and unstable MEEE AuNP solutions was monitored using

UV-vis spectroscopy before and after the addition of this trivalent cation (Figure 5.2, A). The addition of a 0.1 M aliquot of Gd^{3+} to the unstable MEEE AuNPs (Figure 5.2 A, blue trace) caused a bathochromic shift and significant broadening in the absorbance spectra (Figure 5.2 A, red trace). In addition, the shifted absorbance spectra showed a distinct rise above the baseline that was consistent to light scattering off of aggregated nanoparticles that were no longer in solution. NP aggregation was confirmed by eye as well as TEM, where large aggregated masses of NPs were seen throughout the grid surface (Figure 5.2, C). We observed that the aggregation event occurred slowly over time, but could be induced by changing the concentration or ionic strength of the NP solution. In contrast, the stable solution of MEEE AuNPs showed no spectral response to an equal addition of Gd^{3+} (Figure 5.2 A, black and orange traces), and TEM analysis of this NP sample revealed the NPs to remain well dispersed on the grid surface (Figure 5.2, B). Although the absorbance spectra of both the stable and unstable NP solutions appeared similar after synthesis, the drastic difference in the spectral response to the addition of gadolinium suggested compositional discrepancies.

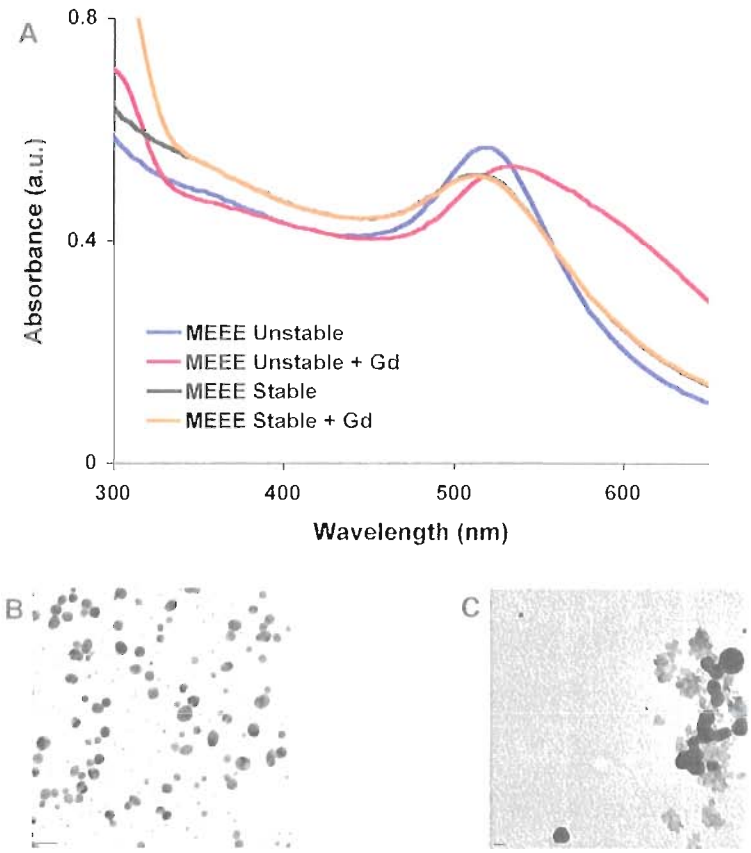

Figure 5.2: UV-vis spectra and TEM micrographs of MEEE functionalized AuNPs. Stable and unstable MEEE particles have a plasmon absorbance at 520 nm, characteristic for NPs greater than 3 nm in size (A, black and blue traces, respectively). The stable MEEE AuNPs show no response to the addition of Gd^{3+} (A, orange trace), suggesting the particles remain dispersed in solution. The addition of Gd^{3+} results in a rise of the baseline and bathochromic shift in the absorbance spectra of the unstable MEEE AuNPs (A, red trace), indicative of particle aggregation. TEM images confirm these UV-vis results, where the stable MEEE particles remain dispersed on the grid (B), and large aggregated clusters of NPs dominate the unstable MEEE AuNP sample(C).

To gain further insight about the differences that existed between the two MEEE AuNP samples, X-ray photoelectron spectroscopy (XPS) was used to analyze the surface of the stable and unstable AuNP samples (Figure 5.3). Nanoparticle size and

ligand footprint were used to estimate the theoretical ligand coverage for functionalized gold nanoparticles.[31] From this information it was possible to use the thiolate to gold ratio (thiolate S2P:Au4f) for each analyzed sample to understand differences that existed in the passivating ligand shell surrounding the gold cores. The stable particles have a thiolate:gold ratio of 0.11 ± 0.02 (Figure 5.3, A). In contrast, the unstable MEEE AuNPs contain a thiolate to gold ratio of 0.05 ± 0.02 (Figure 5.3, C). These differences were significant considering that the mean core diameter of the stable and unstable MEEE AuNPs were nearly the same, at 5.0 ± 0.9 nm (Figure 5.3, B) and 4.5 ± 1.9 nm (Figure 5.3, D), respectively. It is expected that a fully functionalized gold nanoparticle (d_{core} ~ 5-nm) should have a S:Au ratio of 0.14, and a 7-nm AuNP should have a S:Au ratio of 0.11. The unstable MEEE AuNP sample was found to have a S:Au ratio that is less than half the predicted value, while the stable MEEE AuNPs display nearly full monolayer coverage. These results suggested that the particle instability was from the incomplete transformation of the thiosulfate Bunte salt functionality to that of a bound thiolate at the gold particle surface, which caused the nanoparticles to lose solubility and undergo irreversible aggregation. Conversely, the MEEE AuNPs that were passivated with a shell of ligands held to the particle surface primarily by thiolate linkage remained stable, suggesting that the thiolate ligand shell acts as a physical barrier to aggregation. Several control experiments were performed to understand the parameters necessary to form a robust thiolate ligand shell on the gold nanoparticle core and to determine the effects that variable reaction conditions have on the final MEEE AuNP product.

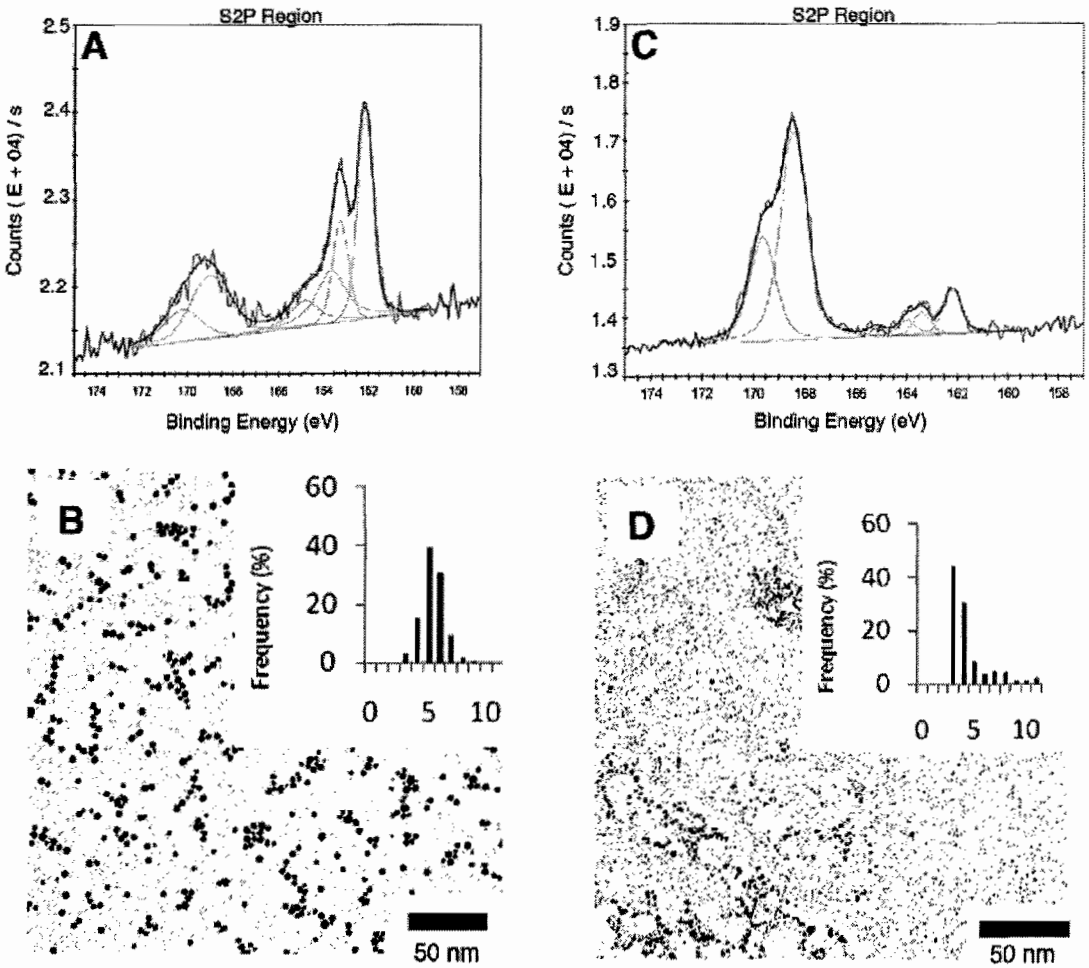

Figure 5.3: XPS spectra and TEM micrographs of stable and unstable MEEE AuNPs. The XPS data reveal the ligand shell on the stable MEEE AuNPs to be predominantly bound to the AuNP surface through covalently bound thiols (A). In contrast, the unstable MEEE AuNPs are predominantly passivated with oxidized sulfur species (C). The core diameters of both synthesized particles are similar. The stable particles are 5.0 ± 0.9 nm (B) and the unstable particles are 4.5 ± 1.9 nm (D). However, the micrographs show that the stable MEEE AuNPs are more evenly distributed on the grid surface as compared to the unstable MEEE AuNP sample.

Evaluation of ligand solution and reaction vessel size as causes for particle instability. First, two trials to prepare MEEE functionalized AuNPs were performed using analogous experimental procedures except for the age of the prepared MEEE

Bunte salt precursor ligand solution. The first batch employed a MEEE ligand solution that had been aged for a two-month period in a scintillation vial. The second batch of AuNPs was synthesized from a freshly prepared solution of the same precursor ligand. UV-vis spectroscopy was used to determine the resulting stability of each nanoparticle sample. Following synthesis and purification, both samples of MEEE AuNPs showed a distinct absorption at 520 nm (Figure 5.4 A, green and purple traces). No spectral response was noted for either NP solution upon the addition of $Gd(NO_3)_3$ (Figure 5.4 A, pink and blue traces), indicating that the age of the ligand solution did not play a contributing role in complete thiolate monolayer formation of MEEE functionalized AuNPs.

The second control study was designed to understand the role that reaction vessel size had on the final stability of MEEE AuNPs. Specifically, reaction vessel size was tested to determine the impact that surface area plays in monolayer formation. A series of reactions having identical synthetic conditions except for vessel size were performed. All 10 reactions carried out in 20-mL scintillation vials produced AuNPs that were not stable to the addition of Gd^{3+} (Figure 5.4 B, black and green traces). Of the 10 trials performed in a 250-mL round bottomed flask, 6 of the trials produced MEEE AuNPs that were stable to the addition of Gd^{3+} (Figure 5.4 B, blue and red traces). The production of both stable and unstable MEEE AuNPs from the larger reaction flask implied that surface area was not a primary contributing factor to stability. However, the inability to prepare stable NPs in the scintillation vials

suggested that mixing, the only variable we were unable to keep constant between the two trials, contributed to particle instability.

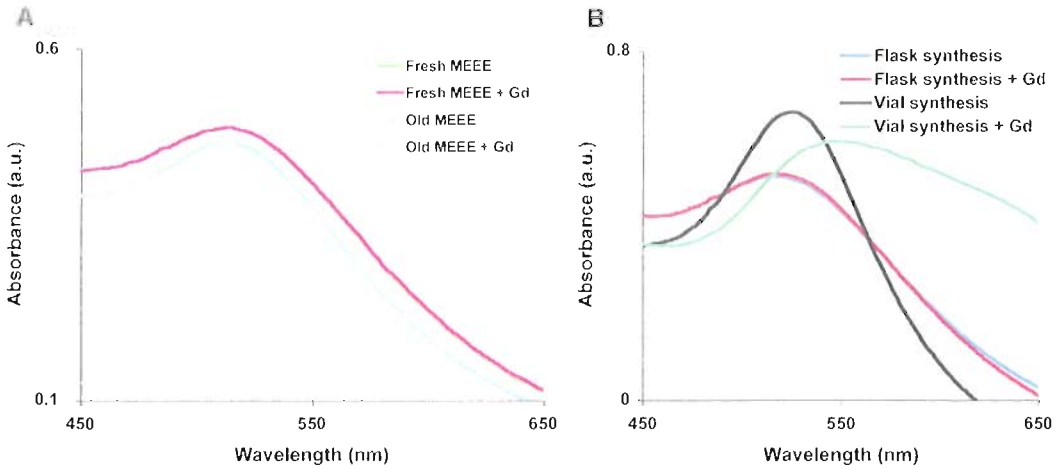

Figure 5.4: UV-vis spectra for control experiments designed to explore ligand solution age and reaction vessel size. The initial absorbance spectra for particles synthesized using a freshly MEEE ligand solution (A, green trace) and particles prepared from an aged MEEE solution (A, purple trace) both have a distinct absorbance at 520 nm. The absorbance remains unchanged upon the addition Gd^{3+}, indicating that the age of ligand solution does not play a significant role in the final nanoparticle product. MEEE AuNPs prepared in a 250-mL reaction flask (B, blue trace) and a 20-mL scintillation vial (B, black trace) also have a distinct absorption at 520 nm. The particles prepared in the larger flask show no response to the addition of Gd^{3+} (B, red trace), while the particles prepared in the smaller vial aggregate immediately upon the addition of Gd^{3+} (B, green trace). These results indicate that variations in reaction conditions generated from the vessel impact the stability of the final nanoparticle product.

Evaluation of reagent addition and mixing on particle stability. The time of addition of the reducing agent was varied in order to determine the necessity to mix the gold salt and ligand prior to reduction. Synthetic trials to produce AuNPs that involved the addition of $NaBH_4$ immediately following the addition of gold and ligand solutions consistently resulted in AuNP aggregation and precipitation. Conversely, NP trials that allowed the gold and ligand solutions to stir before the addition of the reducing agent

resulted in a higher proportion of stable AuNPs. This suggested that an interaction between the gold and ligand species must take place prior to the addition of reductant in order for NP formation to occur. UV-vis spectroscopy was used to monitor a mixture of Au salt and ligand solution over time. Two distinct absorbencies corresponding to the gold salt and precursor ligand were seen (Figure 5.5 A, red and blue traces, respectively). The UV-vis spectra showed a distinct change from the initial mixture of Au salt and precursor ligand to the formation of a new species at t = 6.5 minutes. By t = 9 minutes, formation of this species was complete and no further changes were monitored. The formation of a complex, or monomer, species has been reported for nanoparticle formation, and this change over time is consistent with previous reports[46] for complex formation between gold salt and the thiosulfate functionality on the precursor ligand. As a final confirmation that the formation of this monomer was occurring and the heat from the UV-vis light source did not impact the changes in absorbance observed, the gold salt was heated and monitored by UV-vis. An aqueous solution of gold salt was first heated for 40 minutes (Figure 5.5 B, red trace). No change in the absorbance spectra was determined after prolonged, gentle heating. The gold salt solution was then subjected to quick, intense heating (Figure 5.5 B, red trace). Once again, no changes were observed in the absorbance spectra. These studies confirmed that the spectral changes observed for the gold salt and precursor ligand were the result of the formation of a gold-ligand species, and suggested that the ligand and gold salt should be allowed to stir for a minimum of 10 minutes prior to addition of the reducing agent.

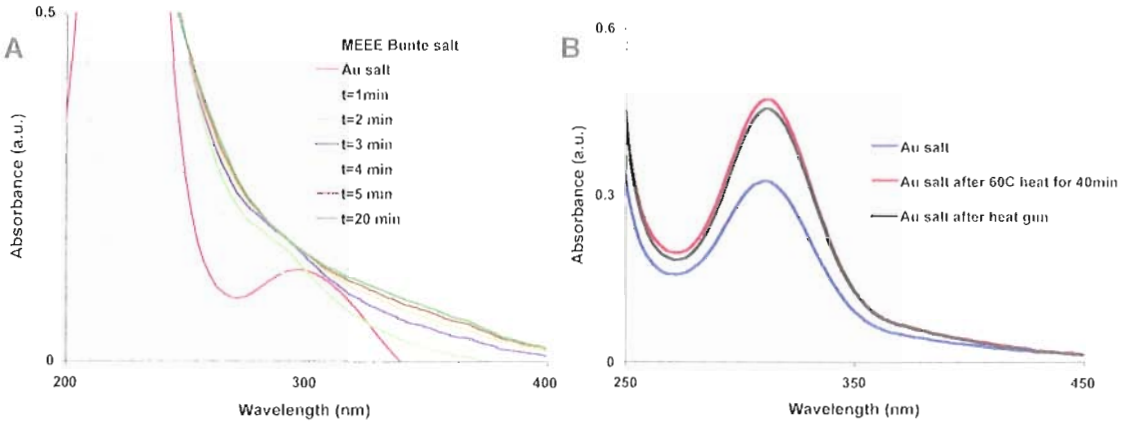

Figure 5.5: UV-vis spectra of Au-ligand complex formation and the impact of heat on $HAuCl_{4\,(aq)}$. The absorbance spectra of the gold salt and ligand solution (A) were collected over a 20 min time interval to monitor the Au-ligand complex formation that occurs prior to the $NaBH_4$ addition. Initially, the gold salt shows an absorbance peak at 300 nm corresponding to the presence of Au^{3+} in solution (A, red trace). Within a minute, the formation of a new gold species begins to change the absorbance spectra. After 4 minutes the absorbance peak at 300 nm has disappeared, suggesting Au^{3+} is no longer present. In order to explore whether heat causes changes to the gold salt, UV-vis spectra were collected after sustained heating (B, red trace) and direct high temperature heating (B, black trace). No changes in the absorbance spectra were observed under either of these conditions, suggesting that the heat from the UV-vis lamp was not responsible for the changes in the absorbance spectra observed during experiment A.

The results of our initial experiments examining reaction variables did not provide sufficient data to determine the direct cause for MEEE gold nanoparticle instability. However, the inability to prepare stable nanoparticles in the scintillation vials, even after the ligand and gold precursors were given sufficient time to form the Au-ligand complex, suggested that the borohydride was prevented from interacting with the precursor complex. This may have been due to inefficient mixing in the vials which caused the formation of a concentration gradient in the reaction media, a variation that

is known to impact NP species.[47] This would result in variable concentrations of the reducing agent available to the complex, which would prevent complete reduction of the Bunte salt ligand, and provide explanation for the inconsistencies in particle stability observed for our MEEE AuNP system. We therefore chose to investigate the role that reducing agent has on MEEE AuNP stability.

Investigating reducing agent concentration on particle stability. In order to test whether borohydride concentration played a role in the formation of stable AuNPs, we prepared MEEE-stabilized gold nanoparticles using varying concentrations of sodium borohydride. We found that unstable particles were more likely to form when the ratio of gold:reducing agent was low (1:2.5 molar equivalents or less), but at higher reducing agent concentrations (1:5-10 molar equivalents), the final nanoparticle products were stable, and did not aggregate during the metal ion assay. Furthermore, XPS analysis indicated that the AuNPs prepared with 5-10 equivalents of $NaBH_4$ were protected by a monolayer that was dominated by covalently bound thiolate ligands, but AuNPs produced with low concentrations of sodium borohydride showed significantly more oxidized sulfur in the XPS analysis, results that were consistent with the XPS data acquired for our initial stable and unstable particles samples provided in Figure 5.3. Based on this data we hypothesized that the reducing agent impacts the formation of the thiolate monolayer, ultimately determining the stability of the MEEE-functionalized AuNPs in solution, as irreversible aggregation during perturbations of the nanoparticle solution is more consistent with particles that are passivated with adsorbed anionic ligands.[48]

Bunte salt reduction to thiolate functionality by sodium borohydride has been reported,[49] and is likely the driving force for ligand transformation in our system, either by direct reduction of the Bunte salt, or by indirect methods, allowing reduction at the gold surface, which then catalyzes the Bunte salt reduction. If sodium borohydride was responsible for Bunte salt conversion to thiolate linkage, the addition of sodium borohydride to an unstable nanoparticle solution should result in the formation of a complete thiolate monolayer, and therefore stabilize the nanoparticle sample.

Transformation of MEEE AuNPs from unstable to stable. To test the ability of sodium borohydride to complete the formation of a thiolate ligand shell on unstable nanoparticles, a sample of purified, unstable MEEE AuNPs was treated with additional borohydride and the resulting changes in particle stability were evaluated with our metal ion assay and XPS analysis. First, a single batch of unstable MEEE AuNPs was divided into three equal parts. To the first sample, three additional molar equivalents of $NaBH_4$ (with respect to gold) were added. To the second portion, an additional three molar equivalents of $NaBH_4$, combined with two additional equivalents of MEEE precursor ligand, were added. To the final portion, an equal volume of Nanopure (no reducing agent, no ligand) was added as a control. Each solution was then stirred for three hours.

The AuNP sample that only received additional water slowly transformed in color from red to deep purple, and eventually resulted in the precipitation of gold metal. The loss of NP stability was observed with UV-vis spectroscopy, where the absorption at 520 nm was lost (Figure 5.6 A, green trace). TEM confirmed the loss of NP stability, where the micrograph image clearly showed the presence of highly aggregated AuNP

species (Figure 5.6, C). The AuNPs treated with additional sodium borohydride (whether in the presence or absence of additional ligand precursor) became stabilized to perturbation in ionicity, pH, or centrifugation. The AuNP solution that received additional $NaBH_4$ retained the distinct plasmon absorbance at 520 nm (Figure 5.6, red trace), and the plasmon absorption remained unchanged after the addition of Eu^{3+} (Figure 5.6, black trace). The increased resistance to solution perturbation suggested that the second $NaBH_4$ addition completed the formation of a thiolate monolayer on the surface of the gold nanoparticles. TEM provided further evidence that the AuNPs treated with additional $NaBH_4$ became stabilized, as the micrograph revealed the particles to have remained well dispersed on the grid surface after the lanthanide ion addition (Figure 5.6, B). Size analysis of the stable and unstable samples show that the stable particles have a diameter of 11.1 ± 5.7 nm, and the unstable particles have a mean diameter of 26.7 ± 15.9. This suggests that the additional $NaBH_4$ suppressed particle growth, but the untreated AuNPs continued to increase in size via aggregation (Figure 5.6, C).

XPS analysis was used to determine the monolayer coverage by comparing the S:Au ratio and the oxidation state of the sulfur on the AuNP surface of the stable and unstable samples. XPS analysis of the stabilized particles revealed a thiolate:Au ratio of 0.17 ± 0.05, while the untreated particles had a thiolate:Au ratio of 0.05 ± 0.01. This data provided final confirmation that the increased stability of the AuNPs treated with additional $NaBH_4$ was due to the formation of a more complete thiolate monolayer on the nanoparticle surface (Figure 5.6, D).

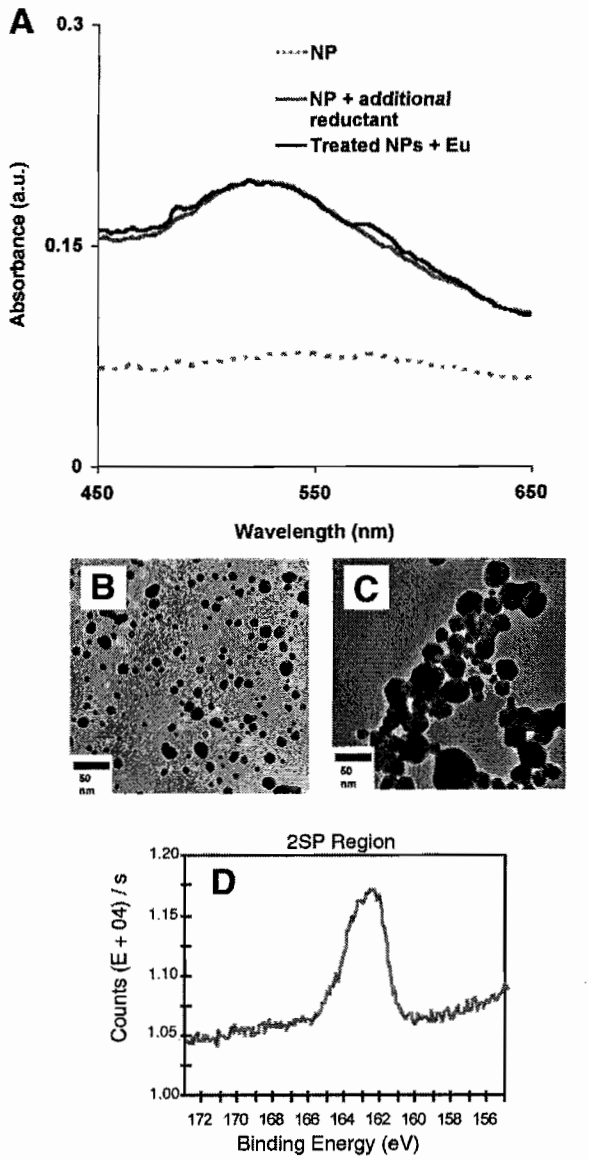

Figure 5.6: UV-vis spectra, TEM micrographs, and XPS spectra of MEEE AuNPs. MEEE AuNPs treated with a second addition of $NaBH_4$ (A, gray trace) show no spectral response to the addition of Eu^{3+} (A, black trace). Micrograph images confirm that these NPs remain well dispersed after the addition of this trivalent cation (B). XPS reveal the MEEE ligand is bound to the AuNP surface through thiolate linkage (D). MEEE AuNPs that were not treated with a second addition of $NaBH_4$ do not remain stable in solution (A, broken trace), and aggregate over time (C).

Conclusions

The use of Bunte salts as ligand precursors offers the distinct advantage of direct synthesis of large gold nanoparticles. However, the unique thiosulfate functionality that enables large AuNP syntheses also makes the prepared AuNPs susceptible to incomplete ligand shell formation. Initial investigations of this transformation suggests that incomplete reduction of the thiosulfate functionality to allow thiolate linkage on the AuNP surface can lead to unstable nanoparticle solutions. To date, the combined results from UV-vis, TEM, and XPS analysis indicate that sodium borohydride, the reducing agent used during synthesis, plays a significant role in this transformation. Several additional experiments are currently underway to provide conclusive confirmation of these results. First, the preparation of MEEE AuNPs in a microreactor are being synthesized to determine the impact that mixing has on NP formation. Secondly, an investigation pertaining to monolayer coverage after additional $NaBH_4$ is added to stable MEEE AuNPs is in progress, and finally, trials have begun to complete the formation of the thiolate monolayer on unstable MEEE AuNPs through ligand exchange and/or addition of the thiol-terminated MEEE precursor ligand. The completion of these experiments should lead to a more reliable synthetic method for producing stable gold nanoparticles from Bunte salt ligand precursors. The ability to prepare stable nanoparticle solutions from Bunte salt ligand precursors will advance our current understanding of nanoparticle formation, and will enable their desirable properties to be reliably incorporated into hybrid materials designed for functional application.

Bridge

Having demonstrated that proper reaction conditions and appropriate synthetic design can permit incorporation of malonamide functionality onto the surface of nanoparticles, we wanted to explore whether this was possible for our bicyclic malonamide (BMA) ligand. However, the previously reported BMA synthesis does not allow synthesis of BMA derivatives that would permit surface functionalization to inorganic substrates to occur. A synthetic strategy that allows differentiation to be incorporated into the BMA molecule was necessary prior to developing materials containing this unique molecule. Chapter VI describes the synthetic strategy to produce differentially substituted BMA molecules. We demonstrate the capability of this new synthetic method to produce molecules for hybrid material design by synthesizing a BMA molecule that incorporates gold nanoparticle-binding thiol functionality within the backbone of the molecule.

CHAPTER VI

SYNTHESIS OF BIFUNCTIONAL BICYCLIC MALONAMIDES DESIGNED FOR HYBRID MATERIAL APPLICATION

Note: Portions of Chapter VI are expected to appear in an upcoming publication, co-authored by C. E. Lisowski, T. Zaikova, B.W. Parks, D.W. Domaille, R. Gilbertson, and J. E. Hutchison. R. Gilbertson, B. W. Parks, and D. W. Domaille developed the initial synthetic strategy. T. Zaikova assisted in the purification of several intermediates and the final protected thiol product. The first author performed the experiments necessary to optimize the synthesis and composed the manuscript corresponding to Chapter VI. J. E. Hutchison provided experimental and editorial guidance.

Introduction

Rational, molecular design allows binding interactions, assembly, and reactivity to be considered in order to aid in the development of next-generation molecules for functional materials designed for application in sensing,[1] optoelectronics,[2,3] energy storage,[4-6] enzyme activation,[7] and environmental remediation.[8-10] Diamide, or malonamide, molecules are one class of ligand that has benefited from the use of rational design in order to enhance the molecular recognition of lanthanide ions. Acyclic malonamides have been studied as agents for f-block ion extraction and

sequestration.[11-13] The increased use of lanthanides for commercial application[14-17] has generated concern about their potential for pollution and warrants the need for agents able to detect and remove these ions from the environment.[10,18-20] The ability to incorporate surface-binding functionality within the backbone of acyclic malonamides ligands without interference to the lanthanide-binding site permits the synthesis of acyclic malonamides able to simultaneously bind f-block ions and inorganic nanostructures. Organic/inorganic hybridization of acyclic malonamides with mesoporous supports[13] and gold nanoparticles[21] have shown the potential use of this ligand class for f-block ion extraction and detection. However, similar efforts to incorporate bicyclic malonamides into hybrid organic/inorganic substrates have not yet been realized.

Recent reports from the Hutchison lab describe the synthesis of 6,6,-bicyclic malonamides (BMAs) and highlight the utility of computer-aided molecular design.[22-25] The substituent on each of the two amide groups (R_1 and R_2) in the BMA structure permit functionality to be incorporated into the molecule. The synthetic approach allows the preparation of bis-functionalized (R_1=R_2) 6,6-BMA (R_2BMA) derivatives using the same strategy. With this general synthetic method we can prepare a diverse library of R_2BMA molecules that includes alkyl chains, alcohols, esters, and fluorinated functional groups.[22] R_2BMAs bind lanthanide and actinide (Ln/Ac) ions in acidic aqueous environments and are able to compete with water and nitrate ions under the same conditions.[24,25] Furthermore, preorganization of the BMA ring structure locks the molecule into the preferred conformation for binding, which results in an enhanced

binding affinity and extraction for Ln/Ac ions over that of its acyclic analogs. Spectrophotometric titration of dimethyl BMA (Me_2BMA) and tetramethyl malonamide (TMMA) with Ho(III) confirm the increased binding of BMAs over analogous acyclic malonamides (Figure 6.1).[24] The binding affinity, ability to bind under harsh conditions, and the relatively simple synthesis make R_2BMA molecules ideal ligands for potential application in f-block ion-based functional materials.

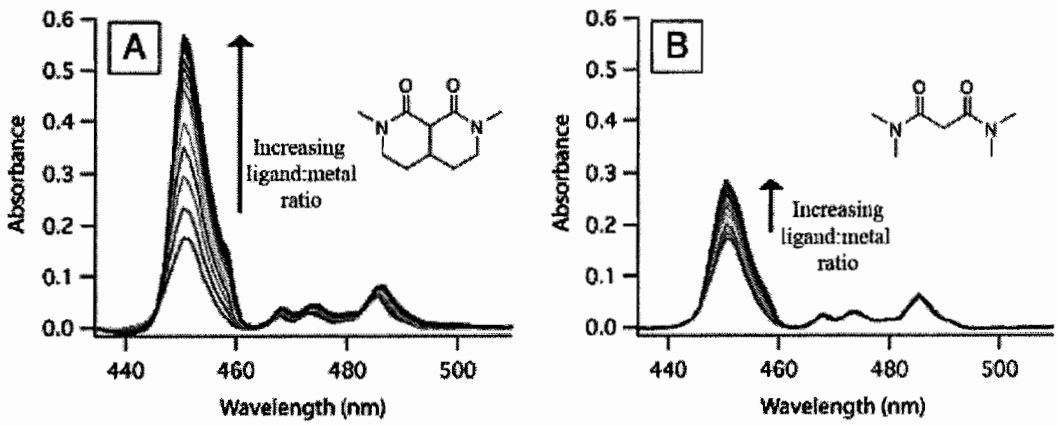

Figure 6.1: UV-vis spectra showing the enhanced binding of BMAs over acyclic malonamides. Me_2BMA (A) or TMMA (B) is slowly titrated into a 1M HNO_3 solution of Ho(III) ion. The absorbance of the peak at 451 nm increases as the ratio of ligand-to-metal is increased, and the intensity of the peak correlates to stronger binding of the ligand to the Ho(III) ion. The increased intensity of the ligand-to-metal peak confirms the enhanced binding of bicyclic over acyclic malonamides.[24,25] Adapted from Parks, B. W.; Gilberston, R. D.; Hutchison, J. E.; Healey, E. R.; Weakley, T. J. R.; Rapko, B. M.; Hay, B. P.; Sinkov, S. I.; Broker, G. A.; Rogers, R. D. *Inorganic Chemistry* **2006**, 45, 1498-1507. Copyright 2006, American Chemical Society.

However, the incorporation of BMA ligands into hybrid complexes remains challenging due to the potential for more reactive derivatives wherein the functional groups attached to the amide lead to polymerization through cross-linking. The synthetic approach is also limited by the inability to incorporate certain (thiol and alkene) functional groups

into the ligand structure. These limitations make it desirable to develop an approach to allow synthesis of BMA ligands where $R_1 \neq R_2$.

Access to differentially substituted BMAs ($R_1 \neq R_2$) eliminates the potential for cross-linking, and permits BMA derivatives to be developed for organic/inorganic material hybridization. Independence of the lanthanide-binding site from the amide substituent allows the binding affinity to be maintained, while the amide groups can be individually functionalized to exploit each R group for separate functions (Figure 6.2).

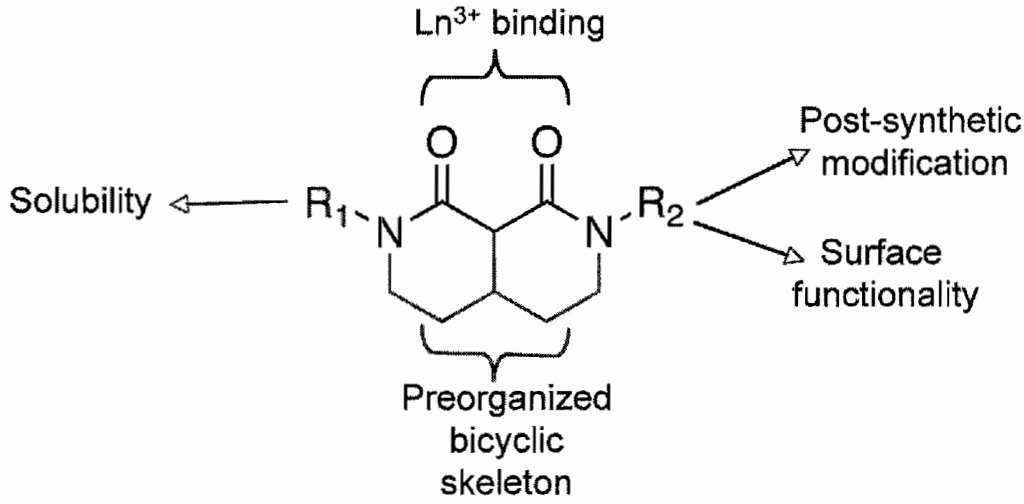

Figure 6.2: Schematic depiction of bifunctional bicyclic malonamide **1**. Successful incorporation of two different groups on each amide substituent decreases the propensity for cross-linking. One group can be used to tune solubility and the other to interact with other molecules or substrates. The preparation of R_1R_2BMA derivatives with R_1 = methyl and R_2 = octyl, octadecyl, and pentanethiol are herein described.

For example, one side of the BMA ligand can be incorporated with functionality designed to control solubility, while the other amide substituent can be designed to incorporate functionality to allow post-synthetic modification and surface functionalization. The incorporation of bicyclic malonamides into hybrid materials

designed for f-block ion extraction and detection should result in enhanced performance due to the increased binding affinity gained from preorganization. Thus, in order to access bifunctional BMAs (R_1R_2BMAs) capable of inorganic hybridization, a successful organic synthetic strategy that permits not only the incorporation of unique functionality on each amide substituent, but also the ability to prepare BMAs with reactive functional groups must occur.

A new synthetic approach is reported that yields three examples of bifunctional BMA molecules that incorporate different functional groups on each amide substituent of the lanthanide binding site. The amide functionalities can be introduced by two stepwise reductive aminations to a mono protected dialdehyde that is the key intermediate in the synthesis. After each of the reductive aminations, one of the rings in the bicyclic structure is closed. Each of the three syntheses can be carried out in seven steps in modest overall yields (23-35%). Purification is facilitated by either a complexation-based method that was developed in our lab,[22] or by standard chromatographic methods. The generality of the synthesis allowed all three different R_1R_2BMA molecules to be prepared using the same synthetic strategy. The stepwise approach permits introduction of more sensitive functionality late in the reaction sequence. Sequential ring closure along with the mild reaction conditions used in the final steps, allow preparation of a bifunctional BMA containing sensitive thiol functionality. Synthesis of a bifunctional bicyclic malonamide containing thiol functionality was not accessible by our previously reported method, and can be used

prepare functional, hybrid materials designed for applications including colorimetric detection of f-block ions.[21]

Experimental methods

Materials. ^{1}H and ^{13}C NMR spectra were recorded on a Varian Inova 300 MHz spectrometer (^{1}H, 299.95 MHz and ^{13}C, 75.43 MHz). Beta-Alanine Ethyl Ester hydrochloride was obtained from TCI America. All other reagents were obtained from Aldrich and used without further purification. Dichloromethane was distilled from calcium hydride prior to use. Tetrahydrofuran was distilled from potassium prior to use. Deionized water (18.2 MΩ-cm) was purified with a Barnstead Nanopure Diamond system.

Synthetic procedures. *5-(tritylthio)pentanenitrile,* ***6****.* To a solution of 120 mL of freshly distilled THF at 0 °C, triphenylmethanethiol (6.98 g, 0.025 mol) and sodium hydride (NaH) (0.66g, 0.028 mol) were added, followed by fast addition of 5-bromopentanenitrile (4.09 g, 0.025 mol). The reaction was stirred for 2 hours while warming to room temperature. 40 mL of CH_3OH was added to quench unreacted NaH and concentrated by rotary evaporation. 120 mL of EtOAc was added and the resulting precipitate filtered. The organic layer was washed 2 x 100 mL H_2O, followed by 1 x 100 mL of aqueous saturated NaCl. The organic layer was dried over $MgSO_4$ and the solvent was removed by rotary evaporation to yield a pale yellow solid. Recrystallization from acetone/water yielded nitrile **6** as needle-like white crystals (7.2

g, 80 %). ^{1}H NMR (300 MHz, CD_2Cl_2) δ 7.2-7.45 (m, 15H), 2.18 (t, 2H), 1.4-1.6 (m, 6H).

*5-(tritylthio)pentan-1-amine, 7.*To a solution of 200 mL of freshly distilled diethyl ether (Et_2O) at 0 °C nitrile **6** (7.2 g, 0.020 mol) was added, followed by slow addition of lithium aluminum hydride ($LiAlH_4$) (0.030 mol, 1.15 g). The reaction was stirred an additional 45 minutes while coming to room temperature. The reaction was quenched by sequential addition of 1.3 mL H_2O, 1.3 mL of aqueous 15 % NaOH, and 4.55 mL H_2O. The resulting solids were removed by vacuum filtration, and the solvent was removed by rotary evaporation to give amine **7** as yellow oil, which solidified upon standing. Triturating with 4 x 3 mL of pentane gave compound **7** as a white solid (6.4 g, 89 %). ^{1}H NMR (300 MHz, CD_2Cl_2) δ 7.2-7.45 (m, 15H), 2.53 (t, 2H), 2.18 (t, 2H), 1.3 (m, 6H), 1.25 (t, 2H).

diethyl 2-(1,1-diethoxy-5-oxopentan-3-yl)malonate, **4**. To 70 mL of freshly distilled THF in a 125 mL round-bottomed flask equipped with a stir bar NaH (0.067 g, 2.9 mmol) and diethyl malonate (0.468 g, 2.9 mmol) was added under inert atmosphere, and the mixture stirred for 10 minutes, followed by rapid addition of aldehyde **3** (0.505 g, 2.9 mmol).[26] The solution was stirred at 25°C until TLC indicated complete consumption of the starting aldehyde (approximately 30 min). 1 mL of deionized H_2O was added to quench unreacted NaH. Most of the THF was removed by rotary evaporation, and the resulting solution diluted with 100 mL of CH_2Cl_2. The aqueous phase was extracted with 2 x 50 mL of CH_2Cl_2 and the combined organics were washed with 1 x 50 mL dilute aqueous acid (pH = 5) and 2 x 100 mL saturated aqueous NaCl.

The organic layer was dried over Na_2SO_4, filtered, and the solvent was removed using rotary evaporation. The resulting oil was triturated with 5 x 10 mL of n-heptane, and the remaining solvent was removed via rotary evaporation. Due to rapid decomposition of the product under ambient conditions, the resulting yellow oil was used immediately without further purification: ^{1}H NMR (300 MHz, $CDCl_3$) δ 9.71 (s, 1H), 4.5 (t, 1H), 4.18 (q, 4H), 3.6 (m, 4H), 3.41 (m, 2H), 2.8 (m, 1H), 2.6 (m, 1H), 1.8 (m, 2H), 1.15-1.25 (mm, 12H).

diethyl 2-(5-(benzyl(methyl)amino)-1,1-diethoxypentan-3-yl)malonate, **9**. To a solution of 30 mL of freshly distilled 1,2-dichloroethane in a 125 mL round-bottomed flask equipped with a stir bar, aldehyde **4** (0.55 g, 1.7 mmol) and methylbenzylamine (0.23 g, 1.9 mmol) was added under inert atmosphere. After the reaction mixture was stirred for 1 h, $Na(OAc)_3BH$ was added (0.52 g, 2.4 mmol) and stirred for an additional 12 h. The organic layer was then washed with 3 x 100 mL saturated aqueous $NaHCO_3$, and 2 x 100 mL saturated aqueous NaCl. The organic layer was dried over Na_2SO_4, filtered, and the solvent was removed using rotary evaporation. The product was purified by thin-layer rotary chromatography (purification started with a CH_2Cl_2/CH_3OH ratio of 5:0.1, which was slowly transitioned to a 5:1 CH_2Cl_2/CH_3OH ratio to allow adequate separation of the polar impurities) to give **9** as a pale yellow oil (0.43 g, 58%). ^{1}H NMR (300 MHz, CD_2Cl_2) δ 7.25 (m, 5H), 4.5 (t, 1H), 4.18 (q, 4H), 3.6 (q, 4H), 3.41 (m, 4H), 2.38 (m, 3H), 2.1 (s, 3H), 1.67 (m, 4H), 1.15-1.25 (mm, 12H). ^{13}C NMR (75 MHz, CD_2Cl_2) δ 169.2, 169.1, 129.1, 128.2, 126.9, 101.8, 62.5, 61.5, 61.2, 61.2, 61.0, 41.9, 35.1, 32.7, 28.9, 15.3, 14.1.

ethyl 4-(2,2-diethoxyethyl)-1-methyl-2-oxopiperidine-3-carboxylate, **10**. To 10 mL of absolute ethanol in a 500 mL Parr hydrogenation flask, **9** (0.75 g, 1.7 mmol) and 20% palladium hydroxide on charcoal (150 mg) were added. Hydrogenolysis of the benzyl group was carried out at 50 psi until H_2 uptake had ceased (~12 h). The suspension was filtered through Celite to remove catalyst, and the remaining solvent removed using rotary evaporation to afford **10** as a colorless oil. The product was purified using thin-layer rotary chromatography (CH_2Cl_2 in CH_3OH) (0.51 g, 99 %). ^{1}H NMR (300 MHz, $CDCl_3$) δ 4.5 (t, 1H), 4.18 (q, 2H), 3.2 - 3.7 (mm, 9H), 3.1 (d, 1H), 2.9 (s, 3H), 2.35 (m, 1H), 2.2 (m, 1H), 1.7 (m, 2H), 1.5 (m, 2H), 1.15-1.25 (mm, 9H). ^{13}C NMR (75 MHz, CD_2Cl_2) δ 181.0, 170.9, 100.8, 85.6, 85.4, 62.2, 61.4, 60.2, 61.0, 55.8, 48.6, 37.5, 33.0, 27.1, 15.6, 15.5.

ethyl 1-methyl-2-oxo-4-(2-oxoethyl)piperidine-3-carboxylate, **11**. To a solution of 5 mL of acetone and 2 mL of 10% aqueous HCl in a 25 mL round-bottomed flask equipped with a stir bar, acetal **10** (0.19 g, 0.6 mmol) was added, and the solution was stirred for 30 minutes. The acetone was removed by rotary evaporation, and the resulting solution diluted with 10 mL of CH_2Cl_2. The aqueous phase was extracted with 2 x 10 mL CH_2Cl_2 and the organic layer washed 1 x 20 mL aqueous saturated NaCl, dried over Na_2SO_4, and filtered. The solvent was removed by rotary evaporation to afford **11** as a colorless oil that was used immediately without further purification due to decomposition of the product under ambient conditions. ^{1}H NMR (300 MHz, $CDCl_3$) δ 9.74 (t, 1H), 4.18 (q, 2H), 3.21 - 3.55 (mm, 2H), 3.1 (d, 1H), 2.9 (s, 3H), 2.45 (m, 1H), 2.2 (m, 2H), 1.45 (m, 2H), 1.25 (t, 3H).

General procedure A: Reductive amination to afford secondary amine 12a-c. To freshly distilled 1,2-dichloroethane in a 125 mL round-bottomed flask equipped with a stir bar, aldehyde **11** (1 equiv.) and primary R_2-amine (1.1 equiv.) were added under an inert atmosphere, and the reaction mixture was stirred for 1 h. $Na(OAc)_3BH$ was then added (1.4 equiv.) and the solution stirred for 12 h. The organic layer was then washed with 3 x 100 mL saturated aqueous $NaHCO_3$, and 2 x 100 mL saturated aqueous NaCl. The organic layer was dried over Na_2SO_4, filtered, and the solvent was removed using rotary evaporation. The product was carried to the next reaction step without purification.

General procedure B: Ring closing to afford 1a-c. Amine **12** (1 equiv.) was added to absolute ethanol and brought to reflux. The solution was stirred until NMR analysis revealed that final ring closure had occurred (24-76 h). Ring closure was indicated by the downfield shift of the methylene proton bridging the two carbonyls. The solvent was removed using rotary evaporation. The crude product was purified by the uranyl precipitation method or thin-layer radial chromatography.

General procedure for purification of 1a and 1b by uranyl precipitation. Purification by uranyl precipitation followed previously reported methods.[22] Briefly, a 2 mL methanolic solution of crude **1** (maximum 0.76 mmol) was added to a 2 mL methanolic solution of uranyl nitrate (0.76 mmol). The resulting yellow precipitate was recovered, washed with 10 mL of CH_3OH, and stirred with 0.5 M EDTA (aqueous, pH 8.0, 5 mL) for 30 min. This solution was extracted with 6 x 15 mL $CHCl_3$, and the

combined organics concentrated using rotary evaporation to afford **1a** as oil (0.35 g, 40% from crude product). [**1b** yields a white solid (0.67 g, 56% from crude product).]

2-methyl-7-octylhexahydro-2,7-naphthyridine-1,8(2H,8aH)-dione, **1a**. ^{1}H NMR (300 MHz, $CDCl_3$) δ 3.3 (m, 6H), 3.16 (d, 1H), 2.89 (s, 3H), 2.4 (m, 1H), 1.93 (m, 2H), 1.64 (m, 2H), 1.56 (t, 3H), 1.5 (m, 2H), 1.28 (m, 10H), 0.87 (t, 3H). ^{13}C NMR (75 MHz, CD_2Cl_2) δ 166.9, 166.8, 50.8, 48.5, 47.6, 45.6, 34.9, 32.3, 31.4, 29.7, 27.7, 27.5, 27.4, 27.3, 27.1, 23.2, 14.4.

2-methyl-7-octadecylhexahydro-2,7-naphthyridine-1,8(2H,8aH)-dione, **1b**. ^{1}H NMR (300 MHz, $CDCl_3$) δ 3.3 (m, 6H), 3.16 (d, 1H), 2.89 (s, 3H), 2.4 (m, 1H), 1.93 (m, 2H), 1.69 (m, 2H), 1.5 (m, 2H), 1.28 (m, 32H), 0.87 (t, 3H). ^{13}C NMR (75 MHz, CD_2Cl_2) δ 166.4, 166.3, 48.1, 47.3, 45.3, 34.5, 32.1, 31.1, 29.9, 29.8, 29.6, 29.5, 27.4, 27.2, 27.0, 26.8, 22.9, 14.1.

Purification of 2-methyl-7-(5-(tritylthio)pentyl)hexahydro-2,7-naphthyridine-1,8(2H,8aH)-dione, **1c**. Amide **1c** (0.7 g, 1.3 mmol) was purified using thin-layer radial chromatography (CH_2Cl_2 in CH_3OH) to afford **1c** as a pale yellow solid (0.42 g, 60% from crude product). ^{1}H NMR (300 MHz, CD_2Cl_2) δ 7.23 – 7.43 (m, 15H), 3.26 (m, 7H), 2.93 (s, 3H), 2.4 (m, 1H), 2.17 (t, 2H), 1.97 (m, 2H), 1.67 (m, 2H), 1.38 (p, 4H), 1.26 (m, 2H). ^{13}C NMR (75 MHz, CD_2Cl_2) δ 167.7, 145.3, 129.7, 128.0, 126.7, 97.5, 97.0, 88.7, 66.5, 50.2, 48.1, 47.1, 45.3, 31.9, 31.0, 28.5, 26.9, 26.8, 26.8, 26.5.

Results and discussion

The previous method to prepare our bis-functionalized bicyclic malonamide efficiently allowed the preparation of R_2BMAs having enhanced binding affinity to f-block ions over analogous acyclic malonamides.[22,24,25] In that synthesis the key intermediate is cyclopentene **2** that affords a dialdehyde upon ozonolysis of the ring, which, after reductive amination with benzyl-protected alkylamines, deprotection and ring closing, yields the R_2BMA. This approach, however, did not permit incorporation of different groups on each of the two amide positions. In order to explore the utility of this extraordinary binding site, a strategy was established to allow individual functionalization of each amide group in order to obtain a bifunctional bicyclic malonamide. The key was to tap the strengths of the established R_2BMA synthetic method, but find a way to break the symmetry of the dialdehyde intermediate. Thus, we chose the diethylacetal aldehyde **4** as the key intermediate that would provide access to BMAs that have different functional groups on each amide substituent.

We initially considered the Schreiber ozonolysis method[27] followed by monoprotection to prepare a protected dialdehyde because it would make use of the cyclopentene starting material, **2**, from our R_2BMA synthesis, offering a route to **4** (Scheme 6.1). However, purification of the intermediates led to significant loss of product, and separation of the product following monoprotection was difficult due to the instability of **4**. The better route to **4** was determined to be conjugate Michael addition of aldehyde **3** to diethyl malonate. Aldehyde **3** could be prepared from commercially available materials in a single step.[26]

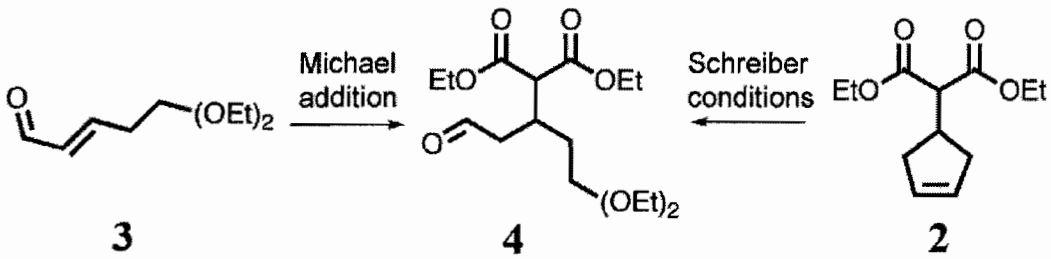

Scheme 6.1: Possible route to a monoprotected dialdehyde.

At first, proline catalyzed Michael addition to provide **4** from protected aldehyde **3** and diethyl malonate was explored because simple synthetic procedures and high yields have been reported.[28-30] However, the use of diethyl malonate with aldehyde **3** using proline salts of lithium and sodium led to the production of side products that proved to be detrimental to subsequent reaction steps. Because aldehyde **4** readily decomposes under ambient conditions, and extensive purification leads to significant product loss, a synthetic method to afford **4** without significant side products was necessary. Deprotonation of diethyl malonate by K_2CO_3 has been reported,[31] but results showed that conjugate addition did not occur. The use of sodium ethoxide also did not provide the desired aldehyde. However, deprotonation of diethyl malonate by NaH led to appreciable yield of aldehyde **4** with very little side product. It was therefore determined that use of the NaH method was the preferred route to **4** because the crude product could be used with minimal purification, affording **4** in high enough purity to proceed without detriment to subsequent reactions (Scheme 6.2).

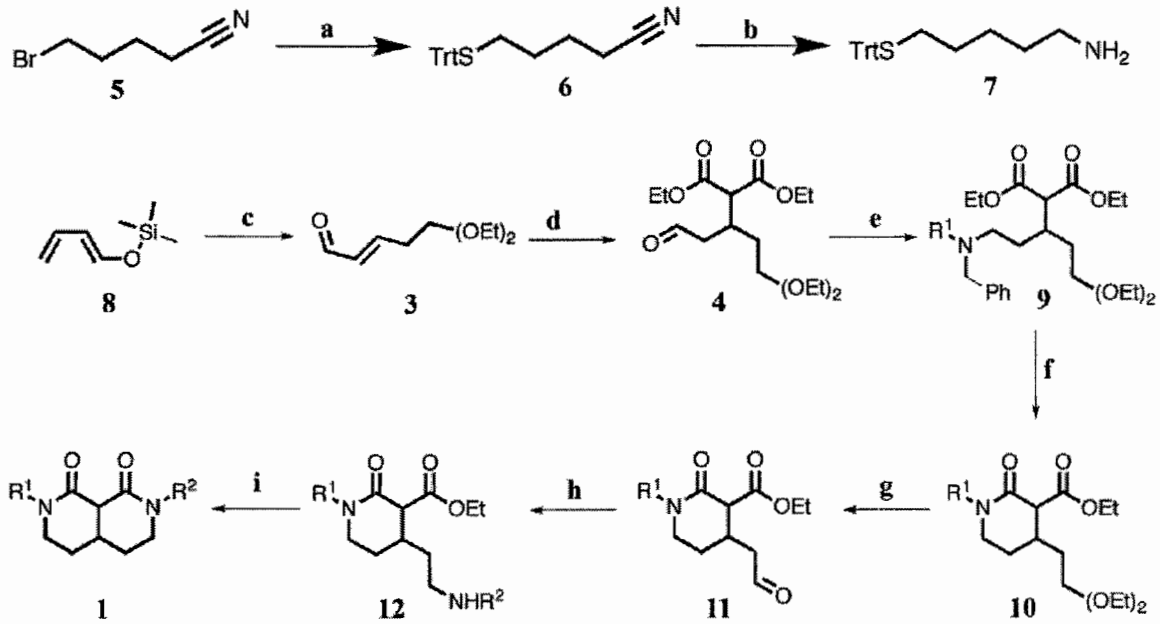

Scheme 6.2: General synthetic route to derivatives of bifunctional bicyclic malonamide **1**. Reagents and conditions: (a) TrtSH, NaH, THF; (b) $LiAlH_4$, Et_2O; (c) 1M $ZnCl_2$ in Et_2O, CH_2Cl_2; (d) diethylmalonate, NaH, THF, N_2; (e) $BnNHR^1$, $NaBH(OAc)_3$, 1,2-dichloroethane; (f) H_2, 20% $Pd(OH)_2$, CH_3CH_2OH; (g) 10% $HCl_{(aq)}$, acetone, rt; (h) NH_2R^2, 1,2-dichloroethane, $NaBH(OAc)_3$, N_2; (i) CH_3CH_2OH, reflux.

For simplicity in synthesis and characterization, the first amide substitution was held constant (R_1 = methyl). Benzyl methylamine was chosen for the initial reductive amination of **4** to form **9**, providing a distinct singlet corresponding to the methyl group as a simple spectroscopic handle to follow though the reaction sequences. The use of a benzyl-protected methylamine at this step afforded an intermediate that was shelf stable, and amenable to chromatographic purification methods. Palladium catalyzed hydrogenation of **9** selectively cleaved the benzyl protecting group. Intramolecular reaction of the methylamine with the ethyl ester to form lactam **10** occurred rapidly

during the hydrogenolysis, providing methyl functionality on the amide substituent, and leaving the diethyl acetal intact. The formed lactam was readily soluble in a 2:1 acetone/10% aqueous HCl mixture that allowed transformation of protected aldehyde **10** to aldehyde **11** within minutes with little to no decomposition.

Reductive amination of **11** with a primary amine leads to **12**. Heating at reflux in ethanol leads to formation of BMA **1**. The second amide substituents (R_2 = octyl, octadecyl) were initially chosen for their usefulness in synthetic development (e.g. good solubility and stability). The use of primary amines during the second reductive amination allows the second amide functionality to be incorporated into the BMA molecule without the use of hydrogenolysis. Elimination of catalytic hydrogenation enables the incorporation of functionalities that cannot tolerate the conditions (alkenes) or might poison the catalyst (thiols). A thiol derivative was also prepared to demonstrate the utility of this synthetic method to incorporate functional groups that were inaccessible by our previous method. The methyl- tritylthiopentyl- BMA derivative was readily synthesized from primary amine **7** in 35% yield over 6 steps.

In addition to serving as confirmation of the utility of the mild synthetic conditions that our new synthetic method provides, BMA **1c** will permit the preparation of BMA-functionalized gold nanoparticles through one of its functional groups (R_2 = protected thiol).[32] We recently reported the preparation of an acyclic malonamide functionalized gold nanoparticle sensor that provides selective, colorimetric detection of lanthanide ions.[21] A hybrid organic/inorganic nanostructure that incorporates **1c** should therefore serve as a colorimetric gold nanoparticle sensor for f-block ion detection.

However, the higher binding affinity of BMAs over analogous acyclic malonamides should result in a lanthanide sensor with even higher sensitivity. Successful use of BMA **1c** will provide a way to compare the performance of this bicyclic malonamide to the acyclic analog that we investigated earlier, and will allow the impacts that molecular structure and binding affinity have on gold nanoparticle-based detection strategies.

Conclusions

The described synthesis focuses on the preparation of bifunctional bicyclic malonamides. The key modification of the BMA synthesis was a successful route to a mono protected dialdehyde that permitted stepwise reductive amination and subsequent ring closing. This class of f-block ion coordinating ligand provides differentiation of the amide substituent, and the mild synthetic procedure allows BMAs containing sensitive functional groups not previously attainable with our previous method to be achieved. Synthesis of a bifunctional BMA containing thiol functionality confirms the ability to incorporate sensitive functionality and represents the synthesis of a R_1R_2BMA capable of inorganic surface functionalization. Thus, our flexible and mild synthetic strategy not only allows BMAs with diverse functionality to be prepared, but also enables future studies designed to explore the potential utility of these molecules for incorporation into functional materials designed for f-block ion application.

CHAPTER VII

CONCLUDING SUMMARY

In this dissertation, a strategy to allow the synthesis and characterization of hybrid nanoscale materials for application in spectroscopic and colorimetric lanthanide ion detection was described. Construction of the hybrid materials were made possible through the successful design of dual function molecular linkers able to bind lanthanide ions and nanoscale substrates simultaneously. The linkers incorporated malonamide functionality that provided a site for lanthanide binding and maintained flexibility for further synthetic modification. Carboxylic acid and thiosulfate functionalities were used to functionalize the surface of zinc oxide (ZnO) and gold (Au) nanoparticles (NPs), respectively, to take advantage of the spectroscopic and colorimetric properties inherent to these inorganic nanoscale substrates. The generality of our design strategy enabled our gold nanoparticle colorimetric sensor to be adapted in order to engineer reversibility into the function of the sensor. The use of Bunte salts to synthesize our functionalized gold nanoparticles also provided an opportunity to investigate the requirements necessary to produce stable gold nanoparticle solutions. Finally, development of a synthetic organic strategy that permitted amide differentiation in our

bicyclic malonamide ligand to allow the synthesis of BMA derivatives able to be incorporated in hybrid nanoscale material design was described.

Chapter II described a method for enhanced europium sensitization through the use of an inorganic antenna. We designed a molecular receptor to contain malonamide and carboxylate functionality in order to tether europium ions close to the surface of zinc oxide nanoparticles. This ligand allowed the synthesis of a ZnO-ligand-Eu^{3+} hybrid complex to occur. Upon excitation, the ZnO-ligand-Eu^{3+} complex resulted in europium sensitization. The europium emission observed for the ZnO-ligand-Eu^{3+} complex was enhanced over that of the individual components of the system. The enhanced emission observed from our hybrid structure confirmed that, with use of a molecular linker, the absorption properties of ZnO, and the emission properties of europium, could be hybridized for lanthanide sensitization. Study of the sensitization of other lanthanide ions with this system can be envisioned. In addition, the general design used to synthesize the molecular linker created for this system can be extended to study the modification of additional inorganic substrates.

Chapters III and IV build off of the successful synthesis of a specific molecule designed for simultaneous lanthanide ion coordination and nanoparticle functionalization, and describe the development of colorimetric sensors for lanthanide ion detection. The sensors incorporate the binding affinity and binding preference of a malonamide ligand with the size-dependant optical properties of gold nanoparticles to synthesize colorimetric sensors that are both selective and sensitive to the detection of lanthanide ions in water. The sensor in Chapter III utilized the MHTMMA ligand to

functionalize the entire gold nanoparticle surface, which resulted in a sensor having a detection limit of 50 nM for Eu^{3+} and Sm^{3+}, which are the lowest reported limits for lanthanide detection for colorimetric sensors of this kind. Chapter IV described the use of a microscale flow reactor to synthesize gold nanoparticles with a mixed ligand shell in order for reversibility to be engineered into the function of our AuNP based lanthanide sensor. The flow system provided the necessary control over the mixing and reagent delivery during NP synthesis to allow formation of a ligand shell comprised mostly of an inert MEEE ligand and only a small amount of the MHTMMA ligand. Dilution of the MHTMMA ligand on the nanoparticle surface limited the extent of nanoparticle cross-linking that occurred during lanthanide recognition, which ultimately determined the extent of reversibility for our sensor. The MEEE/MHTMMA mixed ligand AuNPs maintained sensitive lanthanide detection; we calculated the detection limit to be 100 nM for Eu^{3+}. The nanoparticle cross-linking event that provided the colorimetric sensor response maintained reversibility over several iterations. Additionally, we were able to use the colorimetric response and nanoparticle cross-linking event to provide semi-quantitative assessment of the efficacy of the microscale flow reactor to generate mixed ligand nanoparticles. One can envision using ligands with specific binding functionalities to prepare mixed ligand nanoparticles able to direct the deposition of nanoparticles on surfaces. Specific ligand-binding properties can also be used to assemble higher ordered nanoscale architectures. Use of the microscale flow system to prepare nanoparticles with mixed ligand compositions other than MEEE and MHTMMA are currently underway.

Chapter V explored the reaction parameters necessary to produce stable AuNP solutions from Bunte salt ligand precursors. Reaction parameters including concentration, ligand age, heat and order of reagent addition during nanoparticle synthesis were investigated in order to determine that inadequate mixing and insufficient reducing agent available during nanoparticle formation and stabilization led to unstable AuNPs. The instability was found to be related to the relative amount of oxidized sulfur species on the nanoparticle surface. Upon adequate addition of $NaBH_4$, AuNPs that were stable to perturbations in solution pH and ionicity were prepared. The observed increased stability was the result of the Bunte salt precursor ligand being fully transformed from its oxidized state, to that of bound thiolate linkage on the AuNP surface.

To take advantage of the enhanced lanthanide ion binding of bicyclic malonamides in hybrid nanoscale materials, a synthetic strategy that differentiates the functionality on each amide group was needed. Chapter VI described the preparation of bifunctional bicyclic malonamides (R_1R_2BMAs) with two different functional groups attached to each amide group. Stepwise closing of the rings allowed unique functionality to be individually incorporated on each side of the bicyclic structure. In addition, the mild conditions used during synthesis permitted sensitive functionality not previously attainable with known methods to be realized. Differentiation of the amide groups allows one substituent to be explored for solubility control, and the second amide group to be used to explore reactive groups that would enable functionalization to various surfaces. The successful synthesis of a BMA having protected thiol

functionality allows the development of a R_1R_2BMA functionalized gold nanoparticle to be envisioned. Much like the studies of our acyclic malonamide AuNP system, BMA AuNPs can be used to prepare colorimetric lanthanide ion sensors. However, the enhanced binding affinity of the BMA molecules should permit the fabrication of AuNP sensors with higher sensitivity to occur. Future studies comparing the detection limit for lanthanide ions with gold nanoparticle sensors prepared with acyclic versus bicyclic malonamides can thus be anticipated.

REFERENCES

Chapter I

(1) Barber, D. J.; Freestone, I. C. *Archaeometry* **1990**, *32*, 33-45.

(2) Wiesner, M. R.; Bottero, J. Y. *Environmental Nanotechnology: Applications and Impacts of Nanomaterials*; McGraw Hill: New York, 2007.

(3) Fang, B.; Zhang, C.; Zhang, W.; Wang, G. *Electrochemica Acta* **2009**, *55*, 178-182.

(4) Zhao, L.; Ji, X.; Sun, X.; Li, J.; Yang, W.; Peng, X. *Journal of Physical Chemistry C* **2009**, *113*, 16645-16651.

(5) Kim, Y. J.; Yoo, J.; Kwon, B.; Hong, Y. S.; Lee, C.; Yi, G. *Nanotechnology* **2008**, *19*, 315202/1-315202/5.

(6) Shirai, Y.; Osgood, A.; Zhao, Y.; Yao, Y.; Saudan, L.; Yang, H.; Chiu, Y.; Alemany, L.; Sasaki, Y.; Morin, J.; Guerrero, J.; Kelly, K.; Tour, J. *Journal of the American Chemical Society* **2006**, *128*, 4854-4864.

(7) Mohanty, P.; Landskron, K. *Nanoscale Research Letters* **2009**, *4*, 169-172.

(8) Wiley, B.; Chen, Y.; McLellan, J.; Xiong, Y.; Li, Z.; Ginger, D.; Xia, Y. *Nano Letters* **2007**, *7*, 1032-1036.

(9) Wang, H.; Brandl, D.; Le, F.; Nordlander, P.; Halas, N. *Nano Letters* **2006**, *6*, 827-832.

(10) Dahoumane, S.; Nguyen, M.; Thorel, A.; Boudou, J.; Chehimi, M.; Mangeney, C. *Langmuir* **2009**, *25*, 9633-9638.

(11) Fokin, A.; Schreiner, P. *Molecular Physics* **2009**, *107*, 823-830.

(12) Vaijayanthimala, V.; Tzeng, Y.; Chang, H.; Li, C. *Nanotechnology* **2009**, *20*, 425103/1-425103/9.

(13) Reches, M.; Gazit, E. *Nature Nanotechnology* **2006**, *1*, 195-200.

(14) Zhang, Y.; Lau, S.; Li, H. *Journal of Applied Physics* **2007**, *101*, 033524/1-033524/5.

(15) Fink, D.; Petrov, A.; Fahrner, W.; Hoppe, K.; Papaleo, R.; Berdinsky, A.; Chandra, A.; Zrineh, A.; Chadderton, L. *International Journal of Nanoscience* **2005**, *4*, 965-973.

(16) Desvaux, C.; Amiens, C.; Fejes, P.; Renaud, P.; Respaud, M.; Lecante, P.; Snoeck, E.; Chaudret, B. *Nature Materials* **2005**, *4*, 750-753.

(17) Wang, J.; Chen, Y.; Blau, W. *Journal of Materials Chemistry* **2009**, *19*, 7425-7443.

(18) Elezzabi, A.; Han, Z.; Sederberg, S.; Van, V. *Optics Express* **2009**, *17*, 11045-11056.

(19) Hernandez, R.; Dondapati, S.; Ozalp, V.; Pinto, A.; O'Sullivan, C.; Klar, T.; Katakis, L. *Journal of Biophotonics* **2009**, *2*, 227-231.

(20) Lu, C.; Hao, Q.; Saha, S.; Shi, L.; Kong, X.; Wang, X. *Applied Physics Letters* **2005**, *86*, 063101/1-063101/3.

(21) Zhao, L.; Steinhart, M.; Yosef, M.; Lee, S. H.; Schlecht, S. *Sensors and Actuators b: Chemical* **2005**, *B109*, 86-90.

(22) Hou, C.; Chen, C.; Hou, S.; Li, Y.; Lin, F. *Biomaterials* **2009**, *30*, 4700-4707.

(23) Jiang, B.; Barnett, J.; Li, B. *Nanotechnology, Science and Applications* **2009**, *2*, 21-27.

(24) Rotello, V. M. *Nanoparticles : Building Blocks for Nanotechnology*; Kluwer Academic/Plenum Publishers: New York, 2004.

(25) Dahl, J. A.; Maddux, B. L. S.; Hutchison, J. E. *Chemical Reviews* **2007**, *107*, 2228-2269.

(26) Duchesne, L.; Gentili, D.; Comes-Franchini, M.; Fernig, D. G. *Langmuir* **2008**, *24*, 13572-13580.

(27) Love, J. C.; Estroff, L. A.; Kriebel, J. K.; Nuzzo, R. G.; Whitesides, G. M. *Chemical Reviews* **2005**, *105*, 1103-1169.

(28) Lumetta, G. J.; Rapko, B. M.; Garza, P. A.; Hay, B. P.; Gilbertson, R. D.; Weakley, T. J. R.; Hutchison, J. E. *Journal of the American Chemical Society* **2002**, *124*, 5644-5645.

(29) Manchanda, V. K.; Pathak, P. N.; Rao, A. K. *Solvent Extraction and Ion Exchange* **2004**, *22*, 353-375.

(30) Sessler, J. L.; Melfi, P. J.; Seidel, D.; Gorden, A. E. V.; Ford, D. K.; Palmer, P. D.; Tait, C. D. *Tetrahedron* **2004**, *60*, 11089-11097.

(31) Berthon, L.; Morel, J. M.; Zorz, N.; Nicol, C.; Virelizier, H.; Madic, C. *Separation Science and Technology* **2001**, *36*, 709-728.

(32) Facchini, A.; Amato, L.; Modolo, G.; Nannicini, R.; Madic, C.; Baron, P. *Separation Science and Technology* **2000**, *35*, 1055-1068.

(33) McNamara, B. K.; Lumetta, G. J.; Rapko, B. M. *Solvent Extraction and Ion Exchange* **1999**, *17*, 1403-1421.

(34) Spjuth, L.; Liljenzin, J. O.; Hudson, M. J.; Drew, M. G. B.; Iveson, P. B.; Madic, C. *Solvent Extraction and Ion Exchange* **2000**, *18*, 1-23.

(35) Spjuth, L.; Liljenzin, J. O.; Skalberg, M.; Hudson, M. J.; Chan, G. Y. S.; Drew, M. G. B.; Feaviour, M.; Iveson, P. B.; Madic, C. *Radiochimica Acta* **1997**, *78*, 39-46.

(36) Lumetta, G. J.; Rapko, B. M.; Hay, B. P.; Garza, P. A.; Hutchison, J. E.; Gilbertson, R. D. *Solvent Extraction and Ion Exchange* **2003**, *21*, 29-39.

(37) Sinkov, S. I.; Rapko, B. M.; Lumetta, G. J.; Hay, B. P.; Hutchison, J. E.; Parks, B. W. *Inorganic Chemistry* **2004**, *43*, 8404-8413.

(38) Parks, B. W.; Gilbertson, R. D.; Domaille, D. W.; Hutchison, J. E. *Journal of Organic Chemistry* **2006**, *71*, 9622-9627.

(39) Nogami, M.; Ismail, I. M.; Yamaguchi, M.; Suzuki, K. *Journal of Solid State Chemistry* **2003**, *171*, 353-357.

(40) Bourg, S.; Broudic, J. C.; Conocar, O.; Moreau, J. J. E.; Meyer, D.; Man, M. W. C. *Chemistry of Materials* **2001**, *13*, 491-499.

(41) Broudic, J. C.; Conocar, O.; Moreau, J. J. E.; Meyer, D.; Man, M. W. C. *Journal of Materials Chemistry* **1999**, *9*, 2283-2285.

(42) Eustis, S.; El-Sayed, M. A. *Chemical Society Reviews* **2006**, *35*, 209-217.

(43) Taratula, O.; Galoppini, E.; Wang, D.; Chu, D.; Zhang, Z.; Chen, H.; Saraf, G.; Lu, Y. *Journal of Physical Chemistry B* **2006**, *110*, 6506-6515.

(44) Perera, W. N.; Senanayake, G.; Nicol, M. J. *Inorganica Chimica Acta* **2005**, *358*, 2183-2190.

(45) Distler, H. *Angewandte Chemie International Edition* **1967**, *6*, 544-553.

(46) Shon, Y. S.; Gross, S. M.; Dawson, B.; Porter, M.; Murray, R. W. *Langmuir* **2000**, *16*, 6555-6561.

(47) Daniel, M. C.; Astruc, D. *Chemical Reviews* **2004**, *104*, 293-346.

(48) Hayat, M. A. *Colloidal Gold : Principles, Methods, and Applications*; Academic Press: San Diego, 1989.

(49) Mulvaney, P. *Langmuir* **1996**, *12*, 788-800.

(50) Yonzon, C. R.; Stuart, D. A.; Zhang, X. Y.; McFarland, A. D.; Haynes, C. L.; Van Duyne, R. P. *Talanta* **2005**, *67*, 438-448.

(51) Aslan, K.; Zhang, J.; Lakowicz, J. R.; Geddes, C. D. *Journal of Fluorescence* **2004**, *14*, 391-400.

(52) Elghanian, R.; Storhoff, J. J.; Mucic, R. C.; Letsinger, R. L.; Mirkin, C. A. *Science* **1997**, *277*, 1078-1081.

(53) Kim, Y. J.; Johnson, R. C.; Hupp, J. T. *Nano Letters* **2001**, *1*, 165-167.

(54) Liu, J. W.; Lu, Y. *Journal of the American Chemical Society* **2003**, *125*, 6642-6643.

(55) Zayats, M.; Baron, R.; Popov, I.; Willner, I. *Nano Letters* **2005**, *5*, 21-25.

(56) Liu, J. W.; Lu, Y. *Journal of the American Chemical Society* **2004**, *126*, 12298-12305.

(57) Aili, D.; Selegard, R.; Baltzer, L.; Enander, K.; Liedberg, B. *Small* **2009**, *5*, 2245-2252.

(58) Slocik, J. M.; Zabinski, J. S.; Phillips, D. M.; Naik, R. R. *Small* **2008**, *4*, 548-551.

(59) Golub, E.; Pelossof, G.; Freeman, R.; Zhang, H.; Willner, I. *Analytical Chemistry* **2009**, *81*, 9291-9298.

(60) Diamente, P.; van Veggel, F. *Journal of Fluorescence* **2005**, *15*, 543-551.

(61) Frindell, K. L.; Bartl, M. H.; Robinson, M. R.; Bazan, G. C.; Popitsch, A.; Stucky, G. D. *Journal of Solid State Chemistry* **2003**, *172*, 81-88.

(62) Pauporte, T.; Yoshida, T. *Journal of Materials Chemistry* **2006**, *16*, 4529-4534.

(63) Peng, H.; Wu, C.; Jiang, Y.; Huang, S.; McNeill, J. *Langmuir* **2007**, *23*, 1591-1595.

(64) Stouwdam, J.; Raudsepp, M.; van Veggel, F. *Langmuir* **2005**, *21*, 7003-7008.

(65) Tang, E.; Cheng, G.; Ma, X.; Pang, X.; Zhao, Q. *Applied Surface Science* **2006**, *252*, 5227-5232.

(66) Tien, L. C.; Sadik, P. W.; Norton, D. P.; Voss, L. F.; Pearton, S. J.; Wang, H. T.; Kang, B. S.; Ren, F.; Jun, J.; Lin, J. *Applied Physics Letters* **2005**, *87*, 222106-222112.

(67) Wang, H. T.; Kang, B. S.; Ren, F.; Tien, L. C.; Sadik, P. W.; Norton, D. P.; Pearton, S. J.; Lin, J. *Applied Physics Letters* **2005**, *86*, 243503-243501.

(68) Padmavathy, N.; Vijayaraghavan, R. *Science and Technology of Advanced Materials* **2008**, *9*, 035004-035012.

(69) Oh, B. Y.; Jeong, M. C.; Moon, T. H.; Lee, W.; Myoung, J. M.; Hwang, J. Y.; Seo, D. S. *Journal of Applied Physics* **2006**, *99*, 124505-124509.

(70) Bohle, S.; Spina, C. *Journal of the American Chemical Society* **2009**, *131*, 4397-4404.

(71) Doutt, D.; Mosbacker, H.; Cantwell, G.; Zhang, J.; Song, J.; Brillson, L. *Applied Physics Letters* **2009**, *94*, 042111/1-042111/3.

(72) Hauser, M.; Hepting, A.; Hauschild, R.; Wissinger, M.; Zhou, H.; Stelzl, F.; Fallert, J.; Kalt, H.; Klingshirn, C. *Journal of the Korean Physical Society* **2008**, *53*, 2826-2829.

(73) Lai, C.; An, J.; Ong, H. C. *Applied Physics Letters* **2005**, *86*, 251105/1-251105/3.

(74) Ma, D.; Ye, Z.; Yang, Y. *Applied Physics b: lasers and optics* **2006**, *82*, 85-87.

(75) Pan, A.; Liu, R.; Wang, S.; Wu, Z.; Cao, L.; Xie, S.; Zou, B. *Journal of Crystal Growth* **2005**, *282*, 125-130.

(76) Yamamoto, T.; Wada, Y.; Miyamoto, H.; Yanagida, S. *Chemistry letters* **2004**, *33*, 246-247.

(77) Klonkowski, A. M.; Lis, S.; Pietraszkiewicz, M.; Hnatejko, Z.; Czarnobaj, K.; Elbanowski, M. *Chemistry of Materials* **2003**, *15*, 656-663.

(78) Wu, Y. L.; Lim, C. S.; Fu, S.; Tok, A. I. Y.; Lau, H. M.; Boey, F. Y. C.; Zeng, X. T. *Nanotechnology* **2007**, *18*, 215604-215613.

(79) Yan, B.; Chen, X.; Wu, J. *Applied Surface Science* **2007**, *253*, 8575-8580.

(80) Lima, S. A. M.; Sigoli, F. A.; Davolos, M. R.; Jafelicci, M. *Journal of Alloys and Compounds* **2002**, *344*, 280-284.

(81) Hong, R.; Pan, T.; Qian, J.; Li, H. *Chemical Engineering Journal (Lausanne)* **2006**, *119*, 71-81.

(82) Liufu, S.; Xiao, H.; Li, Y. *Powder Technology* **2004**, *145*, 20-24.

(83) Grasset, F.; Saito, N.; Li, D.; Park, I.; Sakaguchi, N.; Ohashi, H.; Haneda, T.; Roisnel, S.; Mornet, E. *Journal of Alloys and Compounds* **2003**, *360*.

(84) Jackson, A.; Hu, Y.; Silva, P.; Stellacci, F. *Journal of the American Chemical Society* **2006**, *128*, 11135-11149.

(85) Shon, Y. S.; Mazzitelli, C. M.; Murray, R. W. *Langmuir* **2001**, *17*, 7735-7741.

(86) Claridge, S. A.; Goh, S. L.; Frechet, J. M. J.; Williams, S. C.; Micheel, C. M.; Alivisatos, A. P. *Chemistry of Materials* **2005**, *17*, 1628-1635.

(87) Fahmi, A. W.; Stamm, M. *Langmuir* **2005**, *21*, 1062-1066.

(88) Lin, Y.; Boker, A.; J., H.; Sill, K.; Xiang, H.; Abetz, C.; Li, X.; Wang, J.; Emrick, T.; Long, S.; Wang, Q.; Balazs, A.; Russell, T. *Nature* **2005**, *434*, 55-59.

(89) Taton, T. A.; Mucic, R. C.; Mirkin, C. A.; Letsinger, R. L. *Journal of the American Chemical Society* **2000**, *122*, 6305-6306.

(90) Lim, S.; Zhong, C. *Accounts of Chemical Research* **2008**, *42*, 798-808.

(91) Sardar, R.; Heap, T. B.; Shumaker-Parry, J. S. *Journal of the American Chemical Society* **2007**, *129*, 5356–5357.

(92) Rechberger, W.; Hohenau, A.; Leitner, A.; Krenn, J. R.; Lamprecht, B.; Aussenegg, F. R. *Optics Communications* **2003**, *220*, 137-141.

(93) Novak, J.; Feldheim, D. *Journal of the American Chemical Society* **2000**, *122*, 3979-3980.

(94) Chen, G.; Wang, Y.; Tan, L. H.; Yang, M. X.; Tan, L. S.; Chen, Y.; Chen, H. Y. *Journal of the American Chemical Society* **2009**, *131*, 4218-4221.

(95) Shen, C.; Buck, M.; Wilton-Ely, J. D. E. T.; Weidner, T.; Zharnikov, M. *Langmuir* **2008**, *24*, 6609-6615.

(96) Liu, X.; Atwater, M.; Wang, J.; Huo, Q. *Colloids and Surfaces B: Biointerfaces* **2007**, *58*, 3-7.

(97) Woehrle, G. H.; Hutchison, J. E.; Ozkar, S.; Finke, R. G. *Turkish Journal of Chemistry* **2006**, *30*, 1-13.

(98) Kearns, G. J.; Foster, E. W.; Hutchison, J. E. *Analytical Chemistry* **2006**, *78*, 298-303.

(99) Beamson, G.; Briggs, D. *High Resolution Xps of Organic Polymers*; John Wiley & Sons: Chichester, 1992.

(100) Kibel, M. H. In *Surface Analysis Methods in Materials Science*; O'Connor, D. J., Sexton, B. A., Smart, R. S. C., Eds.; Springer: Berlin, 2003, p 175-201.

(101) Jukna, T.; Baltrusaitis, J.; Sinkevicius, V.; Virzonis, D. *Thin Solid Films* **2008**, *516*, 2943-2947.

(102) Lohse, S. E.; Dahl, J. A.; Hutchison, J. E. *Langmuir accepted* **2010**.

Chapter II

(1) Bekiari, V.; Judeinstein, P.; Lianos, P. *Journal of Luminescence* **2003**, *104*, 13-15.

(2) Bunzli, J. C.; Piguet, C. *Chemical Society Reviews* **2005**, *34*, 1048-1077.

(3) Hanaoka, D.; Kikuchi, K.; Kojima, H.; Urano, Y.; Nagano, T. *Journal of the American Chemical Society* **2004**, *126*, 12470-12476.

(4) Jin, T.; Tsutsumi, S.; Deguchi, Y.; Machida, K.; Adachi, G. *Journal of Alloys and Compounds* **1997**, *252*, 59-66.

(5) Kido, J.; Okamoto, Y. *Chemical Reviews* **2002**, *102*, 2357-2368.

(6) Aspinall, H. C. *Chemistry of the F-Block Elements*; Taylor & Francis, 2001.

(7) Gschneidner, K. A.; Eyring, L. R. *Handbook on the Physics and Chemistry of Rare Earths*; North-Holland Publishing Company: Amsterdam, 1979.

(8) D'Aleo, A.; Xu, J.; Moore, E. G.; Jocher, C. J.; Raymond, K. N. *Inorganic Chemistry* **2008**, *47*, 6109-6111.

(9) Diaz-Garcia, M. A.; Fernandez De Avila, S.; Kuzyk, M. G. *Applied Physics Letters* **2002**, *81*, 3924-3926.

(10) Giraud, M.; Andreiadis, E. S.; Fisyuk, A. S.; Demadrille, R.; Pecaut, J.; Imbert, D.; Mazzanti, M. *Inorganic Chemistry* **2008**, *47*, 3952-3954.

(11) Samuel, A. P. S.; Xu, J.; Raymond, K. N. *Inorganic Chemistry* **2009**, *48*, 687-698.

(12) Zhang, J.; Badger, P. D.; Geib, S. J.; Petoud, S. *Angewandte Chemie International Edition* **2005**, *44*, 2508-2512.

(13) *Handbook of Confocal Microscopy*; 2nd ed.; Plenum Press: New York, 1995.

(14) Neckers, D. C.; Valdes-Aguilera, O. M. *Advances in Photochemistry*; Wiley Interscience: New York, 1993; Vol. 18.

(15) Bol, A. A.; van Beek, R.; Meijerink, A. *Chemistry of Materials* **2002**, *14*, 1121-1126.

(16) Peng, H.; Wu, C.; Jiang, Y.; Huang, S.; McNeill, J. *Langmuir* **2007**, *23*, 1591-1595.

(17) Vela, J.; Prall, B. S.; Rastogi, P.; Werder, D. J.; Casson, J. L.; Williams, D. J.; Klimov, V. I.; Hollingsworth, J. A. *Journal of Physical Chemistry C* **2008**, *112*, 20246-20250.

(18) van Veggel, F.; Stouwdam, J.; Hebbink, G.; Huskens, J. *Proceedings of SPIE - The International Society for Optical Engineering* **2003**, *5224*, 164-175.

(19) Chengelis, D. A.; Yingling, A. M.; Badger, P. D.; Shade, C. H.; Petoud, S. *Journal of the American Chemical Society* **2005**, *127*, 16752-16753.

(20) Huhtinen, P.; Kivela, J.; Kuronen, O.; Hagren, V.; Takalo, H.; Tenhu, H.; Lovgren, T.; Harma, H. *Analytical Chemistry* **2005**, *77*, 2643-2648.

(21) Li, H. R.; Zhang, H.-J.; Li, H. C.; Fu, L.-S.; Meng, Q.-G. *Chemical Communications* **2001**, 1212-1213.

(22) Liu, Z.; Liu, M.; Song, W.; Pan, K.; Li, J.; Bai, Y.; Li, T. *Materials Letters* **2006**, *60*, 1629-1633.

(23) Zhong, H.; Wang, J.; Zhou, M.; Wang, S.; Li, Z.; Xu, W.; Chen, X.; Lu, W. *Proceedings of SPIE - The International Society for Optical Engineering* **2005**, *6029*, 60290W1-60290W5.

(24) Klonkowski, A. M.; Lis, S.; Pietraszkiewicz, M.; Hnatejko, Z.; Czarnobaj, K.; Elbanowski, M. *Chemistry of Materials* **2003**, *15*, 656-663.

(25) Wu, Y. L.; Lim, C. S.; Fu, S.; Tok, A. I. Y.; Lau, H. M.; Boey, F. Y. C.; Zeng, X. T. *Nanotechnology* **2007**, *18*, 215604-215613.

(26) Yan, B.; Chen, X.; Wu, J. *Applied Surface Science* **2007**, *253*, 8575-8580.

(27) Lima, S. A. M.; Sigoli, F. A.; Davolos, M. R. *Journal of Solid State Chemistry* **2003**, *171*, 287-290.

(28) Ningthoujam, R. S.; Gajbhiye, N. S.; Ahmed, A.; Umre, S. S.; Sharma, S. J. *Journal of Nanoscience and Nanotechnology* **2008**, *8*, 3059-3062.

(29) Pauporte, T.; Yoshida, T. *Journal of Materials Chemistry* **2006**, *16*, 4529-4534.

(30) Renikuntla, B. R.; Rose, H. C.; Eldo, J.; Waggoner, A. S.; Armitage, B. A. *Organic Letters* **2004**, *6*, 909-912.

(31) Lisowski, C. E.; Hutchison, J. E. *Analytical Chemistry* **2009**, *81*, 10246-10253.

(32) Hong, R.; Pan, T.; Qian, J.; Li, H. *Chemical Engineering Journal (Lausanne)* **2006**, *119*, 71-81.

(33) Sinkov, S. I.; Rapko, B. M.; Lumetta, G. J.; Hay, B. P.; Hutchison, J. E.; Parks, B. W. *Inorganic Chemistry* **2004**, *43*, 8404-8413.

(34) Calefi, P. S.; Ribeiro, A. O.; Pires, A. M.; Serra, O. A. *Journal of Alloys and Compounds* **2002**, *344*, 285-288.

(35) Horrocks, W. D.; Sudnick, D. R. *Journal of the American Chemical Society* **1979**, *101*, 334-340.

(36) Horrocks, W. D.; Sudnick, D. R. *Accounts of Chemical Research* **1981**, *14*, 384-392.

(37) Yin, J.; Xiang, L.; Zhao, X. *Applied Physics Letters* **2007**, *90*, 1131121-1131123.

(38) D'Aleo, A.; Moore, E. G.; Szigethy, G.; Xu, J.; Raymond, K. N. *Inorganic Chemistry* **2009**, *48*, 9316-9324.

(39) Herron, N.; Wang, Y.; Eckert, H. *Journal of the American Chemical Society* **1990**, *112*, 1322-1326.

Chapter III

(1) Kim, Y. J.; Johnson, R. C.; Hupp, J. T. *Nano Letters* **2001**, *1*, 165-167.

(2) Zampolli, S.; Betti, P.; Elmi, I.; Dalcanale, E. *Chemical Communications* **2007**, 2790-2792.

(3) Choi, Y.; Ho, N. H.; Tung, C. H. *Angewandte Chemie, International Edition in English* **2007**, *46*, 707-709.

(4) Gates, A. T.; Fakayode, S. O.; Lowry, M.; Ganea, G. M.; Murugeshu, A.; Robinson, J. W.; Strongin, R. M.; Warner, I. M. *Langmuir* **2008**, *24*, 4107-4113.

(5) Acharya, G.; Doorneweerd, D. D.; Chang, C. L.; Henne, W. A.; Low, P. S.; Savran, C. A. *Journal of the American Chemical Society* **2007**, *129*, 732-733.

(6) Basabe-Desmonts, L.; van der Baan, F.; Zimmerman, R. S.; Reinhoudt, D. N.; Crego-Calama, M. *Sensors* **2007**, *7*, 1731-1746.

(7) Colton, R. J.; Russell, J. N. *Science* **2003**, *299*, 1324-1325.

(8) Stern, E.; Klemic, J. F.; Routenberg, D. A.; Wyrembak, P. N.; Turner-Evans, D. B.; Hamilton, A. D.; LaVan, D. A.; Fahmy, T. M.; Reed, M. A. *Nature* **2007**, *445*, 519-522.

(9) Eustis, S.; El-Sayed, M. A. *Chemical Society Reviews* **2006**, *35*, 209-217.

(10) Jain, P. K.; Lee, K. S.; El-Sayed, I. H.; El-Sayed, M. A. *Journal of Physical Chemistry B* **2006**, *110*, 7238-7248.

(11) Aslan, K.; Zhang, J.; Lakowicz, J. R.; Geddes, C. D. *Journal of Fluorescence* **2004**, *14*, 391-400.

(12) Daniel, M. C.; Astruc, D. *Chemical Reviews* **2004**, *104*, 293-346.

(13) Hayat, M. A. *Colloidal Gold: Principles, Methods, and Applications*; Academic Press: San Diego, 1989.

(14) Rechberger, W.; Hohenau, A.; Leitner, A.; Krenn, J. R.; Lamprecht, B.; Aussenegg, F. R. *Optics Communications* **2003**, *220*, 137-141.

(15) Yonzon, C. R.; Stuart, D. A.; Zhang, X. Y.; McFarland, A. D.; Haynes, C. L.; Van Duyne, R. P. *Talanta* **2005**, *67*, 438-448.

(16) Zayats, M.; Baron, R.; Popov, I.; Willner, I. *Nano Letters* **2005**, *5*, 21-25.

(17) Huang, C. C.; Chang, H. T. *Chemical Communications* **2007**, 1215-1217.

(18) Ipe, B. I.; Yoosaf, K.; Thomas, K. G. *Journal of the American Chemical Society* **2006**, *128*, 1907-1913.

(19) Lee, J. S.; Han, M. S.; Mirkin, C. A. *Angewandte Chemie, International Edition in English* **2007**, *46*, 4093-4096.

(20) Liu, C. W.; Huang, C. C.; Chang, H. T. *Langmuir* **2008**, *24*, 8346-8350.

(21) Liu, J. W.; Lu, Y. *Journal of the American Chemical Society* **2003**, *125*, 6642-6643.

(22) Liu, J. W.; Lu, Y. *Journal of the American Chemical Society* **2004**, *126*, 12298-12305.

(23) Mirkin, C. A.; Letsinger, R. L.; Mucic, R. C.; Storhoff, J. J. *Nature* **1996**, *382*, 607-609.

(24) Slocik, J. M.; Zabinski, J. S.; Phillips, D. M.; Naik, R. R. *Small* **2008**, *4*, 548-551.

(25) Srivastava, S.; Frankamp, B. L.; Rotello, V. M. *Chemistry of Materials* **2005**, *17*, 487-490.

(26) Yoosaf, K.; Ipe, B. I.; Suresh, C. H.; Thomas, K. G. *Journal of Physical Chemistry C* **2007**, *111*, 12839-12847.

(27) Nath, N.; Chilkoti, A. *Journal of the American Chemical Society* **2001**, *123*, 8197-8202.

(28) Elghanian, R.; Storhoff, J. J.; Mucic, R. C.; Letsinger, R. L.; Mirkin, C. A. *Science* **1997**, *277*, 1078-1081.

(29) McNamara, B. K.; Lumetta, G. J.; Rapko, B. M. *Solvent Extraction and Ion Exchange* **1999**, *17*, 1403-1421.

(30) Spjuth, L.; Liljenzin, J. O.; Skalberg, M.; Hudson, M. J.; Chan, G. Y. S.; Drew, M. G. B.; Feaviour, M.; Iveson, P. B.; Madic, C. *Radiochimica Acta* **1997**, *78*, 39-46.

(31) Xu, X. K.; Zhu, W. Z.; Wang, Z. J.; Witkamp, G. J. *Science of the Total Environment* **2002**, *293*, 97-105.

(32) Seo, S.; Marks, T. J. *Organic Letters* **2008**, *10*, 317-319.

(33) Wooten, A. J.; Carroll, P. J.; Walsh, P. J. *Journal of the American Chemical Society* **2008**, *130*, 7407-7419.

(34) Jacquier, A.; Wendland, M.; Do, L.; Robert, P.; Corot, C.; Higgins, C. B.; Saeed, M. *Contrast Media and Molecular Imaging* **2008**, *3*, 112-119.

(35) Bau, M.; Dulski, P. *Earth and Planetary Science Letters* **1996**, *143*, 245-255.

(36) Bau, M.; Knappe, A.; Dulski, P. *Chemie der Erde-Geochemistry* **2006**, *66*, 143-152.

(37) Knappe, A.; Moller, P.; Dulski, P.; Pekdeger, A. *Chemie der Erde-Geochemistry* **2005**, *65*, 167-189.

(38) Nozaki, Y.; Lerche, D.; Alibo, D. S.; Snidvongs, A. *Geochimica et Cosmochimica Acta* **2000**, *64*, 3983-3994.

(39) Nozaki, Y.; Lerche, D.; Alibo, D. S.; Tsutsumi, M. *Geochimica et Cosmochimica Acta* **2000**, *64*, 3975-3982.

(40) http://www.hanford.gov/docs/twrs-atp/section2.html.

(41) McDonald, J. C.; Coursey, B. M.; Carter, M. *Physics Today* **2004**, *57*, 36-41.

(42) Antonovich, V. P.; Stoyanova, I. V.; Chivireva, N. A.; Lasovskaya, O. N.; Presnyak, I. S.; Golik, N. N.; Bezlutskaya, I. V. *Journal of Analytical Chemistry* **1999**, *54*, 627-628.

(43) Antonovich, V. P.; Stoyanova, I. V.; Chivireva, N. A.; Timukhin, E. V.; Zinchenko, V. F.; Efryushina, N. P. *Journal of Analytical Chemistry* **2007**, *62*, 238-244.

(44) Chen, S. L.; Zhao, H. C.; Wang, X. L.; Li, X.; Jin, L. P. *Analytica Chimica Acta* **2004**, *506*, 25-29.

(45) Collins, G. E.; Lu, Q. *Analytica Chimica Acta* **2001**, *436*, 181-189.

(46) Gmar, M.; Capdevila, J. M. *Nuclear Instruments & Methods in Physics Research, Section A: Accelerators, Spectrometers, Detectors, and Associated Equipment* **1999**, *422*, 841-845.

(47) Maizels, M.; Seliskar, C. J.; Heineman, W. R.; Bryan, S. A. *Electroanalysis* **2002**, *14*, 1345-1352.

(48) Santoyo, E.; Garcia, R.; Galicia-Alanis, K. A.; Verma, S. P.; Aparicio, A.; Santoyo-Castelazo, A. *Journal of Chromatography A* **2007**, *1149*, 12-19.

(49) Santoyo, E.; Guevara, M.; Verma, S. P. *Journal of Chromatography A* **2006**, *1118*, 73-81.

(50) Shackleford, S. G. D.; Boxall, C.; Port, S. N.; Taylor, R. J. *Journal of Electroanalytical Chemistry* **2002**, *538*, 109-119.

(51) Haraguchi, H.; Itoh, A.; Kimata, C.; Miwa, H. *Analyst* **1998**, *123*, 773-778.

(52) Hennebruder, K.; Wennrich, R.; Mattusch, J.; Stark, H. J.; Engewald, W. *Talanta* **2004**, *63*, 309-316.

(53) Kautenburger, R.; Beck, H. P. *Journal of Chromatography A* **2007**, *1159*, 75-80.

(54) Distler, H. *Angewandte Chemie Inernational Edition* **1967**, *6*, 544-553.

(55) Shon, Y. S.; Cutler, E. *Langmuir* **2004**, *20*, 6626-6630.

(56) Shon, Y. S.; Gross, S. M.; Dawson, B.; Porter, M.; Murray, R. W. *Langmuir* **2000**, *16*, 6555-6561.

(57) Spjuth, L.; Liljenzin, J. O.; Hudson, M. J.; Drew, M. G. B.; Iveson, P. B.; Madic, C. *Solvent Extraction and Ion Exchange* **2000**, *18*, 1-23.

(58) Lumetta, G. J.; Rapko, B. M.; Garza, P. A.; Hay, B. P.; Gilbertson, R. D.; Weakley, T. J. R.; Hutchison, J. E. *Journal of the American Chemical Society* **2002**, *124*, 5644-5645.

(59) Parks, B. W.; Gilbertson, R. D.; Hutchison, J. E.; Healey, E. R.; Weakley, T. J. R.; Rapko, B. M.; Hay, B. P.; Sinkov, S. I.; Broker, G. A.; Rogers, R. D. *Inorganic Chemistry* **2006**, *45*, 1498-1507.

(60) Sweeney, S. F.; Woehrle, G. H.; Hutchison, J. E. *Journal of the American Chemical Society* **2006**, *128*, 3190-3197.

(61) Lumetta, G. J.; McNamara, B. K.; Rapko, B. M.; Hutchison, J. E. *Inorganica Chimica Acta* **1999**, *293*, 195-205.

(62) Aspinall, H. C. *Chemistry of the F-Block Elements*; Taylor & Francis, 2001.

(63) Sinkov, S. I.; Rapko, B. M.; Lumetta, G. J.; Hay, B. P.; Hutchison, J. E.; Parks, B. W. *Inorganic Chemistry* **2004**, *43*, 8404-8413.

(64) Parks, B. W.; Gilbertson, R. D.; Domaille, D. W.; Hutchison, J. E. *Journal of Organic Chemistry* **2006**, *71*, 9622-9627.

(65) Pirondini, L.; Dalcanale, E. *Chemical Society Reviews* **2007**, *36*, 695-706.

(66) Schneider, H. J.; Yatsimirsky, A. K. *Chemical Society Reviews* **2008**, *37*, 263-277.

Chapter IV

(1) Feynman, R. P. In *A lecture in engineering science*; California Institute of Technology: 1960.

(2) Lim, S.; Zhong, C. *Accounts of Chemical Research* **2008**, *42*, 798-808.

(3) Weiss, P. *Accounts of Chemical Research* **2008**, *41*, 1772-1781.

(4) Jackson, A. M.; Myerson, J. W.; Stellacci, F. *Nature Materials* **2004**, *3*, 330-337.

(5) Xu, X. Y.; Rosi, N. L.; Wang, Y. H.; Huo, F. W.; Mirkin, C. A. *Journal of the American Chemical Society* **2006**, *128*, 9286-9287.

(6) Hu, Y.; Uzun, O.; Dubois, C.; Stellacci, F. *Journal of Physical Chemistry C* **2008**, *112*, 6279-6284.

(7) Kim, J. H.; Kim, J. W. *Langmuir* **2008**, *24*, 5667-5671.

(8) Nishiyabu, R.; Hashimoto, N.; Cho, T.; Watanabe, K.; Yasunaga, T.; Endo, A.; Kaneko, K.; Niidome, T.; Murata, M.; Adachi, C.; Katayama, Y.; Hashizume, M.; Kimizuka, N. *Journal of the American Chemical Society* **2009**, *131*, 2151-2158.

(9) Nam, K. T.; Kim, D. W.; Yoo, P. J.; Chiang, C. Y.; Meethong, N.; Hammond, P. T.; Chiang, Y. M.; Belcher, A. M. *Science* **2006**, *312*, 885-888.

(10) Wang, Y.; Tang, Z. Y.; Tan, S. S.; Kotov, N. A. *Nano Letters* **2005**, *5*, 243-248.

(11) Kim, Y. J.; Johnson, R. C.; Hupp, J. T. *Nano Letters* **2001**, *1*, 165-167.

(12) Eustis, S.; El-Sayed, M. A. *Chemical Society Reviews* **2006**, *35*, 209-217.

(13) Choi, Y.; Ho, N. H.; Tung, C. H. *Angewandte Chemie International Edition* **2007**, *46*, 707-709.

(14) Elghanian, R.; Storhoff, J. J.; Mucic, R. C.; Letsinger, R. L.; Mirkin, C. A. *Science* **1997**, *277*, 1078-1081.

(15) Gates, A. T.; Fakayode, S. O.; Lowry, M.; Ganea, G. M.; Murugeshu, A.; Robinson, J. W.; Strongin, R. M.; Warner, I. M. *Langmuir* **2008**, *24*, 4107-4113.

(16) Mirkin, C. A.; Letsinger, R. L.; Mucic, R. C.; Storhoff, J. J. *Nature* **1996**, *382*, 607-609.

(17) Lisowski, C. E.; Hutchison, J. E. *Analytical Chemistry* **2009**, *81*.

(18) Li, Q. F.; He, J. B.; Glogowski, E.; Li, X. F.; Wang, J.; Emrick, T.; Russell, T. P. *Advanced Materials* **2008**, *20*, 1462-1466.

(19) Zhang, Z. L.; Glotzer, S. C. *Nano Letters* **2004**, *4*, 1407-1413.

(20) Jackson, A. M.; Hu, Y.; Silva, P. J.; Stellacci, F. *Journal of the American Chemical Society* **2006**, *128*, 11135-11149.

(21) Vilain, C.; Goettmann, F.; Moores, A.; Le Floch, P.; Sanchez, C. *Journal of Materials Chemistry* **2007**, *17*, 3509-3514.

(22) Farokhzad, O. C.; Khademhosseini, A.; Yon, S. Y.; Hermann, A.; Cheng, J. J.; Chin, C.; Kiselyuk, A.; Teply, B.; Eng, G.; Langer, R. *Analytical Chemistry* **2005**, *77*, 5453-5459.

(23) He, S. T.; Liu, Y. L.; Maeda, H. *Journal of Nanoparticle Research* **2008**, *10*, 209-215.

(24) Prasad, N.; Perumal, J.; Choi, C. H.; Lee, C. S.; Kim, D. P. *Advanced Functional Materials* **2009**, *19*, 1656-1662.

(25) Song, Y. J.; Hormes, J.; Kumar, C. S. S. R. *Small* **2008**, *4*, 698-711.

(26) Wang, K.; Wang, Y. J.; Chen, G. G.; Luo, G. S.; Wang, J. D. *Industrial & Engineering Chemistry Research* **2007**, *46*, 6092-6098.

(27) McKenzie, L. C.; Zakharov, L. N.; Hutanu, D.; Remcho, V. T.; Hutchison, J. E. *to be submitted to Nature Nanotechnology* **2010**.

(28) Lohse, S. E.; Dahl, J. A.; Hutchison, J. E. *Langmuir accepted* **2010**.

(29) Sweeney, S. F.; Woehrle, G. H.; Hutchison, J. E. *Journal of the American Chemical Society* **2006**, *128*, 3190-3197.

(30) Woehrle, G. H.; Hutchison, J. E.; Ozkar, S.; Finke, R. G. *Turkish Journal of Chemistry* **2006**, *30*, 1-13.

(31) Daniel, M. C.; Astruc, D. *Chemical Reviews* **2004**, *104*, 293-346.

(32) Shon, Y. S.; Cutler, E. *Langmuir* **2004**, *20*, 6626-6630.

(33) Woehrle, G. H.; Warner, M. G.; Hutchison, J. E. *Journal of Physical Chemistry B* **2002**, *106*, 9979-9981.

(34) Ji, X.; Song, X.; Li, J.; Bai, Y.; Yang, W.; Peng, X. *Journal of the American Chemical Society* **2007**, *129*, 13939-13948.

(35) Peng, X. A.; Peng, X. *Journal of the American Chemical Society* **2001**, *123*, 1389-1395.

(36) Yu, W. W.; Peng, X. *Angewandte Chemie International Edition* **2002**, *41*, 2368-2371.

(37) Yu, W. W.; Wang, Y. A.; Peng, X. *Chemistry of Materials* **2003**, *15*, 4300-4308.

(38) Hostetler, M. J.; Wingate, J. E.; Zhong, C. J.; Harris, J. E.; Vachet, R. W.; Clark, M. R.; Londono, J. D.; Green, S. J.; Stokes, J. J.; Wignall, G. D.; Glish, G. L.; Porter, M. D.; Evans, N. D.; Murray, R. W. *Langmuir* **1998**, *14*, 17-30.

Chapter V

(1) Choi, Y.; Ho, N. H.; Tung, C. H. *Angewandte Chemie International Edition* **2007**, *46*, 707-709.

(2) Slocik, J. M.; Zabinski, J. S.; Phillips, D. M.; Naik, R. R. *Small* **2008**, *4*, 548-551.

(3) Lee, J. S.; Han, M. S.; Mirkin, C. A. *Angewandte Chemie International Edition* **2007**, *46*, 4093-4096.

(4) Cha, J. N.; Bartl, M. H.; Wong, M. S.; Popitsch, A.; Deming, T. J.; Stucky, G. D. *Nano Letters* **2003**, *3*, 907-911.

(5) Jeong, S.; Achermann, M.; Nanda, J.; Ivanov, S.; Klimov, V. I.; Hollingsworth, J. A. *Journal of the American Chemical Society* **2005**, *127*, 10126-10127.

(6) Kim, T.; Noh, M.; Lee, H.; Joo, S.-W.; Lee, S. Y.; Lee, K. *The Journal of Physical Chemistry B* **2009**, *113*, 14487-14490.

(7) Paul, S.; Pearson, C.; Molloy, A.; Cousins, M. A.; Green, M.; Kolliopoulou, S.; Dimitrakis, P.; Normand, P.; Tsoukalas, D.; Petty, M. C. *Nano Letters* **2003**, *3*, 533-536.

(8) Zheng, J.; Constantinou, P. E.; Micheel, C.; Alivisatos, A. P.; Kiehl, R. A.; Seeman, N. C. *Nano Letters* **2006**, *6*, 1502-1504.

(9) Chen, C.-F.; Tzeng, S.-D.; Chen, H.-Y.; Lin, K.-J.; Gwo, S. *Journal of the American Chemical Society* **2007**, *130*, 824-826.

(10) Ishifuji, M.; Mitsuishi, M.; Miyashita, T. *Journal of the American Chemical Society* **2009**, *131*, 4418-4424.

(11) Kang, Y.; Erickson, K. J.; Taton, T. A. *Journal of the American Chemical Society* **2005**, *127*, 13800-13801.

(12) Daniel, M. C.; Astruc, D. *Chemical Reviews* **2004**, *104*, 293-346.

(13) Eustis, S.; El-Sayed, M. A. *Chemical Society Reviews* **2006**, *35*, 209-217.

(14) Hayat, M. A. *Colloidal Gold: Principles, Methods, and Applications*; Academic Press: San Diego, 1989.

(15) Rotello, V. M. *Nanoparticles: Building Blocks for Nanotechnology*; Kluwer Academic/Plenum Publishers: New York, 2004.

(16) Woehrle, G. H.; Brown, L. O.; Hutchison, J. E. *Journal of the American Chemical Society* **2005**, *127*, 2172-2183.

(17) Hess, A.; Brosch, O.; Weyhermuller, T.; Metzler-Nolte, N. *Journal of Organometallic Chemistry* **1999**, *589*, 75-84.

(18) Sardar, R.; Heap, T. B.; Shumaker-Parry, J. S. *Journal of the American Chemical Society* **2007**, *129*, 5356-5357.

(19) Hillebrenner, H.; Buyukserin, F.; Kang, M.; Mota, M. O.; Stewart, J. D.; Martin, C. R. *Journal of the American Chemical Society* **2006**, *128*, 4236-4237.

(20) Kannan, B.; Kulkarni, R. P.; Majumdar, A. *Nano Letters* **2004**, *4*, 1521-1524.

(21) Lisowski, C. E.; Hutchison, J. E. *Analytical Chemistry* **2009**, *81*.

(22) Niikura, K.; Nagakawa, K.; Ohtake, N.; Suzuki, T.; Matsuo, Y.; Sawa, H.; Ijiro, K. *Bioconjugate Chemistry* **2009**, *20*, 1848-1852.

(23) Sun, L.; Liu, D.; Wang, Z. *Langmuir* **2008**, *24*, 10293-10297.

(24) Verma, A.; Nakade, H.; Simard, J. M.; Rotello, V. M. *Journal of the American Chemical Society* **2004**, *126*, 10806-10807.

(25) Duchesne, L.; Gentili, D.; Comes-Franchini, M.; Fernig, D. G. *Langmuir* **2008**, *24*, 13572-13580.

(26) Kulkarni, A. P.; Munechika, K.; Noone, K. M.; Smith, J. M.; Ginger, D. S. *Langmuir* **2009**, *25*, 7932-7939.

(27) Mei, B. C.; Oh, E.; Susumu, K.; Farrell, D.; Mountziaris, T. J.; Mattoussi, H. *Langmuir* **2009**, *25*, 10604-10611.

(28) Wang, Y.; Neyman, A.; Arkhangelsky, E.; Gitis, V.; Meshi, L.; Weinstock, I. A. *Journal of the American Chemical Society* **2009**, *131*, 17412-17422.

(29) Dahl, J. A.; Maddux, B. L. S.; Hutchison, J. E. *Chemical Reviews* **2007**, *107*, 2228-2269.

(30) Rouhana, L. L.; Jaber, J. A.; Schlenoff, J. B. *Langmuir* **2007**, *23*, 12799-12801.

(31) Hostetler, M. J.; Wingate, J. E.; Zhong, C. J.; Harris, J. E.; Vachet, R. W.; Clark, M. R.; Londono, J. D.; Green, S. J.; Stokes, J. J.; Wignall, G. D.; Glish, G. L.; Porter, M. D.; Evans, N. D.; Murray, R. W. *Langmuir* **1998**, *14*, 17-30.

(32) Templeton, A. C.; Wuelfing, W. P.; Murray, R. W. *Accounts of Chemical Research* **2000**, *33*, 27-36.

(33) Lukkari, J.; Meretoja, M.; Kartio, I.; Laajalehto, K.; Rajamaki, M.; Lindstrom, M.; Kankare, J. *Langmuir* **1999**, *15*, 3529-3537.

(34) Lusk, A. T.; Jennings, G. K. *Langmuir* **2001**, *17*, 7830-7836.

(35) Shon, Y. S.; Gross, S. M.; Dawson, B.; Porter, M.; Murray, R. W. *Langmuir* **2000**, *16*, 6555-6561.

(36) Shon, Y. S.; Mazzitelli, C.; Murray, R. W. *Langmuir* **2001**, *17*, 7735-7741.

(37) Ciszek, J. W.; Stewart, M. P.; Tour, J. M. *Journal of the American Chemical Society* **2004**, *126*, 13172-13173.

(38) Ciszek, J. W.; Tour, J. M. *Chemistry of Materials* **2005**, *17*, 5684-5690.

(39) Lohse, S. E.; Dahl, J. A.; Hutchison, J. E. *Langmuir accepted* **2010**.

(40) Caragheorgheopol, A.; Chechik, V. *Physical Chemistry Chemical Physics* **2008**, *10*, 5029-5041.

(41) Sardar, R.; Funston, A. M.; Mulvaney, P.; Murray, R. W. *Langmuir* **2009**, *25*, 13840-13851.

(42) Shen, C.; Buck, M.; Wilton-Ely, J. D. E. T.; Weidner, T.; Zharnikov, M. *Langmuir* **2008**, *24*, 6609-6615.

(43) Sweeney, S. F.; Woehrle, G. H.; Hutchison, J. E. *Journal of the American Chemical Society* **2006**, *128*, 3190-3197.

(44) Woehrle, G. H.; Hutchison, J. E.; Ozkar, S.; Finke, R. G. *Turkish Journal of Chemistry* **2006**, *30*, 1-13.

(45) Ji, X.; Song, X.; Li, J.; Bai, Y.; Yang, W.; Peng, X. *Journal of the American Chemical Society* **2007**, *129*, 13939-13948.

(46) Song, Y. J.; Hormes, J.; Kumar, C. S. S. R. *Small* **2008**, *4*, 698-711.

(47) Stoeva, S.; Klabunde, K. J.; Sorensen, C. M.; Dragieva, I. *Journal of the American Chemical Society* **2002**, *124*, 2305-2311.

(48) Ju-Nam, Y.; Bricklebank, N.; Allen, D. W.; Gardiner, P. H. E.; Light, M. E.; Hursthouse, M. B. *Organic & Biomolecular Chemistry* **2006**, *4*, 4345-4351.

Chapter VI

(1) Pirondini, L.; Dalcanale, E. *Chemical Society Reviews* **2007**, *36*, 695-706.

(2) Luo, J.; Zhou, X.-H.; Jen, A. *Journal of Materials Chemistry* **2009**, *19*, 7410-7424.

(3) Wakita, J.; Sekino, H.; Sakai, K.; Urano, Y.; Ando, S. *Journal of Physical Chemistry B* **2009**, *113*, 15212-15224.

(4) Li, G.; Jiang, K.-J.; Bao, P.; Li, Y.-F.; Li, S.-L.; Yang, L.-M. *New Journal of Chemistry* **2009**, *33*, 868-876.

(5) Zhang, X.; Zhang, J.-J.; xia, Y.-Y. *Journal of Photochemistry and Photobiology, A* **2008**, *194*, 167-172.

(6) Mondal, R.; Ko, S.; Norton, J. E.; Miyaki, N.; Bercerril, H. A.; Verploegen, E.; Toney, M.; Bredas, J.-L.; McHehee, M. D.; Bao, Z. *Journal of Materials Chemistry* **2009**, *19*, 7195-7197.

(7) Battacharya, S.; Biswas, J. *Langmuir* **ASAP**.

(8) Gorden, A. E.; Xu, J.; Raymond, K. N.; Durbin, P. *Chemical Reviews* **2003**, *103*, 4207-4282.

(9) Hay, B. P.; Firman, T. K.; Lumetta, G. J.; Rapko, B. M.; Garza, P. A.; Sinkov, S. I.; Hutchison, J. E.; Parks, B. W.; Gilbertson, R. D.; Weakley, T. J. R. *Journal of Alloys and Compounds* **2004**, *374*, 416-419.

(10) Wassana, Y.; Fryxell, G. E.; Addleman, R. S.; Wiacek, R. J.; Koonsiripaiboon, V.; Pattamakomsan, K.; Sukwarotwat, V.; Xu, J.; Raymond, K. N. *Journal of Hazardous Materials* **2009**, *168*, 1233-1238.

(11) McNamara, B. K.; Lumetta, G. J.; Rapko, B. M. *Solvent Extraction and Ion Exchange* **1999**, *17*, 1403-1421.

(12) Spjuth, L.; Liljenzin, J. O.; Skalberg, M.; Hudson, M. J.; Chan, G. Y. S.; Drew, M. G. B.; Feaviour, M.; Iveson, P. B.; Madic, C. *Radiochimica Acta* **1997**, *78*, 39-46.

(13) Trens, P.; Russell, M. L.; Spjuth, L.; Hudson, M. J.; Liljenzin, J. O. *Industrial & Engineering Chemistry Research* **2002**, *41*, 5220-5225.

(14) Xu, X. K.; Zhu, W. Z.; Wang, Z. J.; Witkamp, G. J. *Science of the Total Environment* **2002**, *293*, 97-105.

(15) Wooten, A. J.; Carroll, P. J.; Walsh, P. J. *Journal of the American Chemical Society* **2008**, *130*, 7407-7419.

(16) Seo, S.; Marks, T. J. *Organic Letters* **2008**, *10*, 317-319.

(17) Jacquier, A.; Wendland, M.; Do, L.; Robert, P.; Corot, C.; Higgins, C. B.; Saeed, M. *Contrast Media and Molecular Imaging* **2008**, *3*, 112-119.

(18) Bau, M.; Dulski, P. *Earth and Planetary Science Letters* **1996**, *143*, 245-255.

(19) Bau, M.; Knappe, A.; Dulski, P. *Chemie der Erde-Geochemistry* **2006**, *66*, 143-152.

(20) Hennebruder, K.; Wennrich, R.; Mattusch, J.; Stark, H. J.; Engewald, W. *Talanta* **2004**, *63*, 309-316.

(21) Lisowski, C. E.; Hutchison, J. E. *Analytical Chemistry* **2009**, *81*, 10246-10253.

(22) Parks, B. W.; Gilbertson, R. D.; Domaille, D. W.; Hutchison, J. E. *Journal of Organic Chemistry* **2006**, *71*, 9622-9627.

(23) Lumetta, G. J.; Rapko, B. M.; Garza, P. A.; Hay, B. P.; Gilbertson, R. D.; Weakley, T. J. R.; Hutchison, J. E. *Journal of the American Chemical Society* **2002**, *124*, 5644-5645.

(24) Parks, B. W.; Gilbertson, R. D.; Hutchison, J. E.; Healey, E. R.; Weakley, T. J. R.; Rapko, B. M.; Hay, B. P.; Sinkov, S. I.; Broker, G. A.; Rogers, R. D. *Inorganic Chemistry* **2006**, *45*, 1498-1507.

(25) Sinkov, S. I.; Rapko, B. M.; Lumetta, G. J.; Hay, B. P.; Hutchison, J. E.; Parks, B. W. *Inorganic Chemistry* **2004**, *43*, 8404-8413.

(26) Liu, J.; Castro, R.; Abboud, K. A.; Kaifer, A. E. *Journal of Organic Chemistry* **2000**, *65*, 6973-6977.

(27) Schreiber, S. L.; Claus, R. E.; Reagan, J. *Tetrahedron Letters* **1982**, *23*, 3867-3870.

(28) Cao, X.; Wang, W.; Wang, G.; Chen, L. *Huaxue Tongbao* **2009**, *72*, 776-782.

(29) Yamaguchi, M.; Shiraishi, T.; Hirama, M. *Journal of Organic Chemistry* **1996**, *61*, 3520-30.

(30) Yamaguchi, M.; Yokota, N.; Minami, T. *Journal of the Chemical Society-Chemical Communications* **1991**, 1088-1089.

(31) Krishtal, G. V.; Kul'ganek, V. V.; Kucherov, V. F.; Yanovskaya, L. A. *Synthesis* **1979**, 107-9.

(32) Hayat, M. A. *Colloidal Gold : Principles, Methods, and Applications*; Academic Press: San Diego, 1989.